

---

## National Laser Users' Facility and External Users' Programs

Under the facility governance plan implemented in FY08 to formalize the scheduling of the Omega Laser Facility as a National Nuclear Security Administration (NNSA) User Facility, Omega Facility shots are allocated by campaign. The majority (69.2%) of the FY18 target shots were allocated to the Inertial Confinement Fusion (ICF) Campaign conducted by integrated teams from Lawrence Livermore National Laboratory (LLNL), Los Alamos National Laboratory (LANL), Naval Research Laboratory (NRL), Sandia National Laboratories (SNL), and LLE; and to the High-Energy-Density (HED) Campaigns conducted by teams led by scientists from the national laboratories, some with support from LLE.

The Fundamental Science Campaigns accounted for 27.4% of the Omega Laser Facility target shots taken in FY18. Nearly 60% of these shots were dedicated experiments led by U.S. academia and businesses under the National Laser Users' Facility (NLUF) Program, and the remaining shots were allotted to the Laboratory Basic Science (LBS) Program, comprising peer-reviewed fundamental science experiments conducted by the national laboratories and LLE.

The Omega Laser Facility was also used for several campaigns led by teams from the Commissariat à l'énergie atomique et aux énergies (CEA) of France, the University of Bordeaux of France, and the joint Rutherford Appleton Laboratory (RAL) and the University of York of the United Kingdom. These externally funded experiments are conducted at the facility on the basis of special agreements put in place by UR/LLE and participating institutions with the endorsement by the Department of Energy (DOE)/NNSA.

The facility users during this year included 13 collaborative teams participating in the NLUF Program; 15 teams led by LLNL, LANL, and LLE scientists participating in the LBS Program; many collaborative teams from the national laboratories and LLE conducting ICF experiments; investigators from LLNL, LANL, and LLE conducting experiments for high-energy-density-physics programs; and scientists and engineers from CEA, the University of Bordeaux, and RAL/York.

In this section, we briefly review all the external user activity at the Omega Laser Facility during FY18.

### **FY18 NLUF Program**

FY18 was the second of a two-year period of performance for the 13 NLUF projects (Table 156.VII) approved for FY17–FY18 funding and Omega Laser Facility shot allocation. In total, 293 target shots were taken for NLUF projects during FY18. The NLUF experiments conducted at the facility during FY18 are summarized in this section.

A critical part of the NLUF Program is the education and training of graduate students in high energy density and plasma physics. During the year, 34 graduate students from ten universities participated in experiments conducted under the NLUF Program at the Omega Laser Facility (Table 156.VIII). Ten graduate students trained under the Omega Fundamental Science Program (NLUF and LBS) successfully defended their Ph.D. theses in 2017/2018 (Table 156.IX).

### ***Transport of Relativistic Electrons in Cylindrically Imploded Magnetized Plasmas***

Principal Investigator: F. N. Beg [University of California, San Diego (UCSD)]

Co-investigators: C. McGuffey, M. Dozières, M. Bailly-Grandvaux, P. Forestier-Colleoni, and K. Bhutwala (UCSD); M. S. Wei [General Atomics (GA)]; P. Gourdain, J. R. Davies, and E. M. Campbell (LLE); K. Matsuo and S. Fujioka (University of Osaka); and J. J. Santos and D. Batani (University of Bordeaux)

In the electron fast-ignition (FI) scheme of inertial confinement fusion (ICF), two drivers separately compress the fuel to high density and then heat it via intense electron-beam generation. A high-energy (over 10 kJ), high-intensity (over  $10^{20}$  W/cm<sup>2</sup>), short-pulse (~10-ps) laser is used to create the intense, appropriately energetic (~3- to 10-MeV) electrons to heat the compressed fuel plasma to initiate ignition. Magnetic fields may aid in guiding the electrons to the core. Therefore, transport of these electrons inside a compressed, hot, magnetized plasma must be investigated; in particular, to determine (1) the

volume or position of the plasma heated by the relativistic electrons; and (2) the energy and number of relativistic electrons that can reach the core and effectively heat the core plasma. These unresolved issues warranted a new approach/platform to observe the spatial energy deposition of relativistic electrons in a characterized, compressed volume. The objective of the UCSD NLUF project in collaboration with General Atomics, LLE, the University of Bordeaux, and the University of Osaka is to systematically investigate the relativistic electrons' propagation and energy deposition in a pre-assembled cylindrical plasma under controlled conditions of density and temperature with and without an external magnetic field. Understanding the role of an external magnetic field in relativistic electrons' transport and energy distribution is important for several applications including fast-ignition inertial confinement fusion.

This year we performed the first joint experiment of the project after characterizing the cylindrical target compressed

by OMEGA in 2017 with and without an external magnetic field applied by the MIFEDS (magneto-inertial fusion electrical discharge system) driver. For all shots, 36 beams (0.3-TW/beam, 1.5-ns square pulse) of the OMEGA laser were used to compress a CH cylinder filled with Cl-doped CH foam to reach a density close to  $8 \text{ g/cm}^3$ . A schematic of the joint experiments is shown in Fig. 156.58. The cylinder, with a  $600\text{-}\mu\text{m}$  outer diameter and a  $540\text{-}\mu\text{m}$  inner diameter, was filled by  $0.1 \text{ g/cm}^3$  of CH foam doped with 1% of Cl. In addition, one Cu foil and one Zn foil were attached to the cylinder sides in order to decrease the magnetic mirror and allow  $K_\alpha$  emission during the joint shots.

The implosion was characterized through static and framed x-ray imagers and Cl x-ray spectroscopy focused on K-shell emission lines with a spectral range from 2600 eV to 3600 eV. An example pinhole image is shown in the inset of Fig. 156.58, which exhibits a column of self-emission near the cylinder axis, indicating compression. The time-resolved spectroscopy data

Table 156.VII: NLUF projects approved for the FY17–FY18 funding and Omega Laser Facility shot allocation.

Principal Investigator	Institution	Title
F. N. Beg	University of California, San Diego	Transport of Relativistic Electrons in Cylindrically Imploded Magnetized Plasmas
A. Bhattacharjee	Princeton University	Dynamics of Magnetic Reconnection in High-Energy-Density Plasmas
R. P. Drake	University of Michigan	Experimental Astrophysics on the OMEGA Laser
T. S. Duffy	Princeton University	Phase Transitions and Crystal Structure of Tin Dioxide at Multi-Megabar Pressures
R. Jeanloz	University of California, Berkeley	High-Energy-Density Chemical Physics and Planetary Evolution
H. Ji	Princeton University	Particle Acceleration Resulting from Magnetically Driven Reconnection Using Laser-Powered Capacitor Coils
K. Krushelnick	University of Michigan	X-Ray Measurements of Laser-Driven Relativistic Reconnection Using OMEGA EP
D. Q. Lamb	University of Chicago	Properties of Magnetohydrodynamic Turbulence in Laser-Produced Plasmas
R. Mancini	University of Nevada, Reno	Development of a Photoionized Plasma Experiment on OMEGA EP
R. D. Petrasso	Massachusetts Institute of Technology	Explorations of Inertial Confinement Fusion, High-Energy-Density Physics, and Laboratory Astrophysics
A. Spitkovsky	Princeton University	Study of Magnetized Collisionless Shocks in Laser-Produced Plasmas
D. Stutman	John Hopkins University	Demonstration of a Talbot–Lau X-Ray Deflectometry Electron Density Diagnostic in Laser–Target Interactions
M. S. Wei/ C. Krauland	General Atomics	Hot-Electron Generation with $10^6\text{-W/cm}^2$ Lasers in Shock-Ignition–Relevant Conditions

gave us insight into the evolution of the cylinder compression including differences in the compression with the presence of the magnetic field. With the field, we observed the continuum emission of the target becoming more intense, while the density and temperature increased until reaching a maximum intensity before the full compression of the cylinder. In the second phase, the emission spectra intensity decreased with the expansion of

the plasma, which occurred after full compression. In addition, we could observe the emission lines from  $Li_{\alpha}$  to  $Ly_{\alpha}$  as well as a broadening of  $He_{\beta}$  with density and opacity effects. To analyze these data, we used an atomic physics code to reproduce the emission lines to estimate the temperature and density of the cylinder during the compression. The radiation-hydrodynamic code *FLASH* was used to provide expectations for the compres-

Table 156.VIII: Graduate students participating in NLUF experiments in 2018.

Name	University	Principal Investigator
Krish Bhutwala	University of California, San Diego	Beg
Rui Hua	University of California, San Diego	Beg
Shu Zhang	University of California, San Diego	Beg/Wei
Jack Matteucci	Princeton University	Bhattacharjee/Fox/Schaeffer
Adrianna Angulo	University of Michigan	Drake
Patrick X. Belancourt	University of Michigan	Drake
Shane Coffing	University of Michigan	Drake
Laura Elgin	University of Michigan	Drake
Heath LeFevre	University of Michigan	Drake
Alex Rasmus	University of Michigan	Drake
Robert Vandervort	University of Michigan	Drake
Joseph Levesque	University of Michigan	Drake/Hartigan
Sirius Han	Princeton University	Duffy
Donghoon Kim	Princeton University	Duffy
Tylor Perez	John Hopkins University	Duffy/Wicks
Melissa Sims	Stonybrook University	Duffy/Wicks
Abraham Chien	Princeton University	Ji
Paul Campbell	University of Michigan	Krushelnick
Amina Hussein	University of Michigan	Krushelnick
Peter Kordell	University of Michigan	Krushelnick
Archie Bott	Oxford University/University of Chicago	Lamb/Tzeferacos/Gregori
Alexandra Rigby (Ph.D. 2018)	Oxford University/University of Chicago	Lamb/Tzeferacos/Gregori
Daniel Mayer	University of Nevada, Reno	Mancini
Kyle Swanson	University of Nevada, Reno	Mancini
Patrick Adrian	MIT	Petrasso
Timothy Mark Johnson	MIT	Petrasso
Neel Kabadi	MIT	Petrasso
Brandon Lahmann	MIT	Petrasso
Jacob Percy	MIT	Petrasso
Raspberry Simpson	MIT	Petrasso
Hon Sio (Ph.D. 2018)	MIT	Petrasso
Graeme Sutcliffe	MIT	Petrasso
Shuhui Cao	University of Rochester	Ren/Wei
Cole Holcomb	Princeton University	Spitkovsky

sion dynamics through 2-D cylindrical simulations with the magnetohydrodynamic (MHD) module. Figure 156.59 shows maps of density and temperature at various times during the simulated compression.

In FY18's joint shots, the OMEGA EP short-pulse laser (850 J, 10 ps) irradiated an aluminum disk coating on the Zn end cap of the same nominal target with normal incidence at three different delays into the implosion with the same nominal

Table 156.IX: Recent Ph.D.'s trained under the Omega Fundamental Science (NLUF and LBS) Program.

Name	Institution/Supervisor	Graduation Year	Current Position
Hong Sio	MIT/Petrasso	2018	Postdoc at MIT, applying for fellowship with national labs
Alison Saunders	University of California, Berkeley/ Falcone	2018	Postdoc at LLNL
Alexandra Rigby	Oxford University/ University of Chicago/Gregori	2018	Industry
Matthew Newman	Caltech/Ravichandran	2018	Private sector
Jonathan Peebles	University of California, San Diego/ Beg	2017	Postdoc at LLE
Rachel Young	University of Michigan/Drake	2017	Postdoc at University of Michigan
Jeffrey Fein	University of Michigan/Drake	2017	Postdoc at SNL
Willow Wan	University of Michigan/Drake	2017	Postdoc at LANL
Andrew Liao	Rice University/Hartigan	2017	Postdoc at LANL
Luke Ceurvorst	Oxford University/Norreys	2017	Postdoc at CELIA, University of Bordeaux

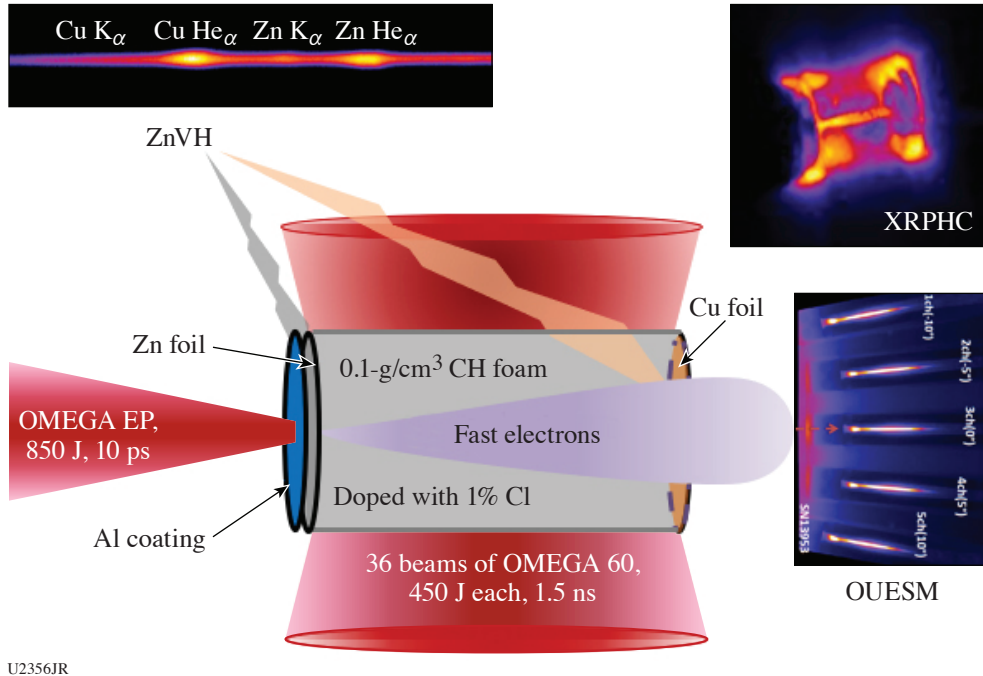


Figure 156.58 Schematic of the electron transport target with primary diagnostics, the ZnVH K-shell x-ray spectrometer, and the five-channel magnetic-particle Osaka University electron spectrometer (OUESM). XRPHC: x-ray pinhole camera.

drive conditions and magnetic field. Relativistic electrons with energy up to 30 MeV, accelerated from the interaction at  $10^{19}$ -W/cm<sup>2</sup> intensity, were measured primarily with five magnetic spectrometers spanning  $\pm 10^\circ$  from the axis of the cylinder. At zero delay, electron transport through the as-yet uncompressed foam was steered at least  $10^\circ$  off-axis, while at a 1.2-ns delay the transmitted electron beam was forward directed. At the latest delay tested, the escaping electrons were reduced across the whole spectrum. Additional clues about the electrons' transport inside the target were obtained from the

$K_\alpha$  they induced in the Zn and Cu foils, which were recorded with a von Hamos configuration x-ray spectrometer (ZnVH). The emission of the Cu and Zn foils included hot ionic lines that hint at the temperature of the foils as well as  $K_\alpha$ , which indicates the number of electrons.

These measured behaviors are consistent with two-step modeling using *FLASH* to model the hydrodynamics of the implosion and 3-D hybrid particle-in-cell (PIC) simulations, which elucidate the transport. Plotted in Fig. 156.60 are

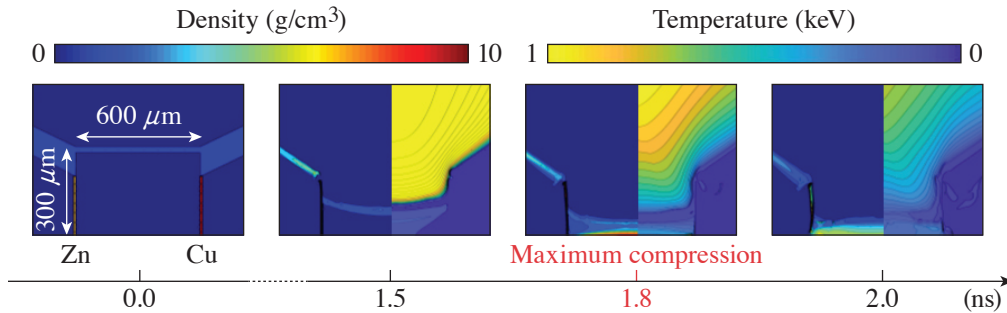
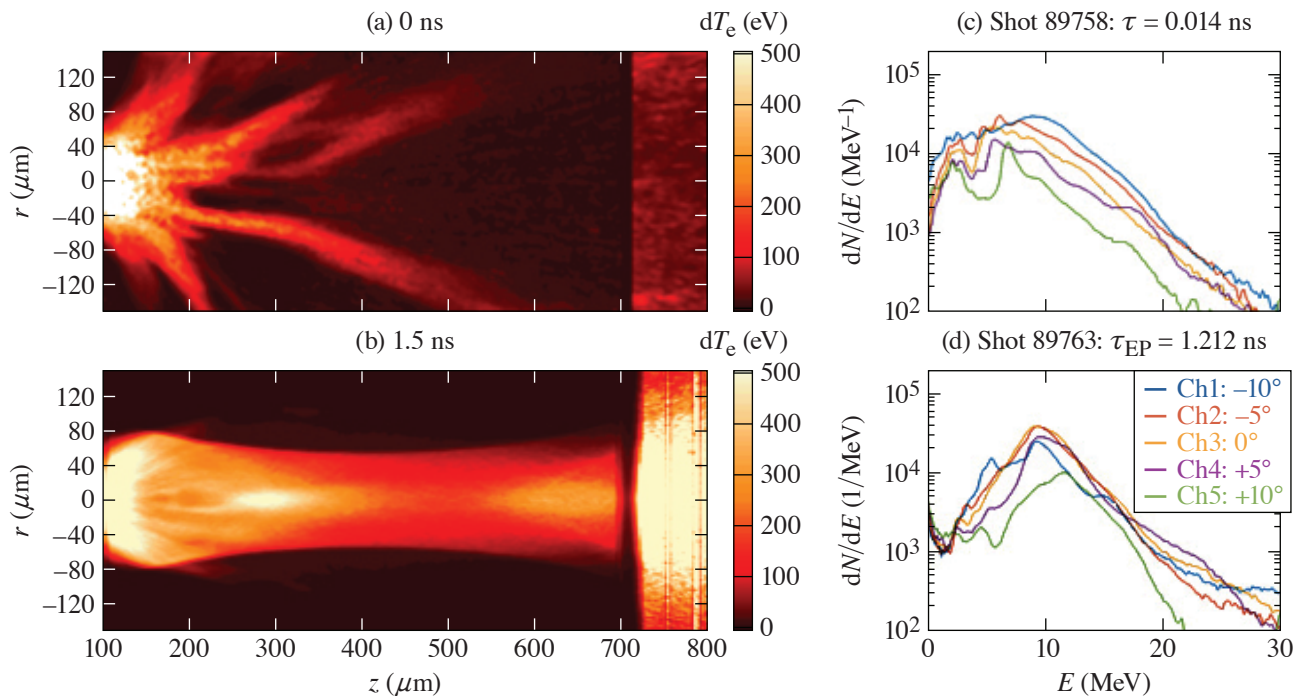


Figure 156.59  
*FLASH* simulations of the OMEGA-driven cylindrical target implosion at four times. For each map, the left half shows density and the right half shows temperature.

U2357JR



U2358JR

Figure 156.60

Electron transport behavior at different delay times in simulations and experimental data. [(a),(b)] PIC simulation of the electron transport through the target is visualized through the maps of temperature increase. (a) At 0 ns, electrons are highly affected by filamentation in the uncompressed foam, heating it in an uncontrollable fashion, while (b) at 1.5 ns, the electrons are guided in a channel, heating a column of plasma all the way to the rear. [(c),(d)] The OUESM spectrometer data show that (c) for a shot with no delay, an electron beam was present but steered at least  $10^\circ$  off axis. (d) For a shot with a 1.2-ns delay, the electron beam was forward directed, and the spectra indicate additional stopping of electrons below 5 MeV and high throughput of electrons above 8 MeV.

simulation outputs from the PIC simulations showing maps of increased temperature when electrons are injected into the *FLASH*-predicted imploding target for cases at two different delays. The *FLASH* density, temperature, and magnetic-field maps at the delays indicated were used as initial conditions. At zero delay, resistive filamentation of the electron beam resulted in wide-angle beamlets in multiple directions. After 1 ns into the implosion, a self-generated B field developed into a channel that effectively guided the electrons through to the target rear. Lastly, at a simulated delay of 1.75 ns, when the applied magnetic field was constricted to 500 T, transport of the electrons was severely terminated because of magnet mirroring.

In summary, we have successfully implemented a platform to study relativistic electron transport in cylindrically compressed plasmas with and without magnetic fields. Simulations show that the magnetic field facilitates efficient transport and energy deposition of fast electrons, which this first set of experimental data tends to confirm.

### ***Dynamics of Magnetic Reconnection in High-Energy-Density Plasmas***

Principal Investigators: A. Bhattacharjee, W. Fox, D. Schaeffer, and J. Matteucci (PPPL); G. Fiksel (University of Michigan); and D. Haberberger and R. K. Follett (LLE)

We have developed and conducted experiments at the Omega Laser Facility to study the related phenomena of magnetic reconnection and collisionless shocks. Magnetic reconnection occurs when regions of opposite directed magnetic fields in a plasma can interact and relax to a lower-energy state; it is an essential plasma physics process that governs the storage and explosive release of magnetic energy in systems such as the earth's magnetosphere, the solar corona, and magnetic-fusion devices. The energy thereby liberated can produce heat flows and can enable the acceleration of a large number of particles to high energies. Magnetic reconnection in laser plasmas can occur between externally imposed magnetic fields (generated by MIFEDS on OMEGA) or magnetic fields self-generated in the plasma by the Biermann battery effect. Recent reconnection experiments (from the 2017 NLUF allocation) with colliding Biermann-generated fields observed the onset of magnetic-reconnection-triggered plasmoid instabilities occurring in the reconnection layer. This effect has been predicted to be important to drive fast rates of magnetic reconnection in many space and astrophysical plasmas. These results have been submitted to *Nature*.<sup>1</sup>

During previous NLUF reconnection experiments on OMEGA EP using MIFEDS, we also unexpectedly observed the

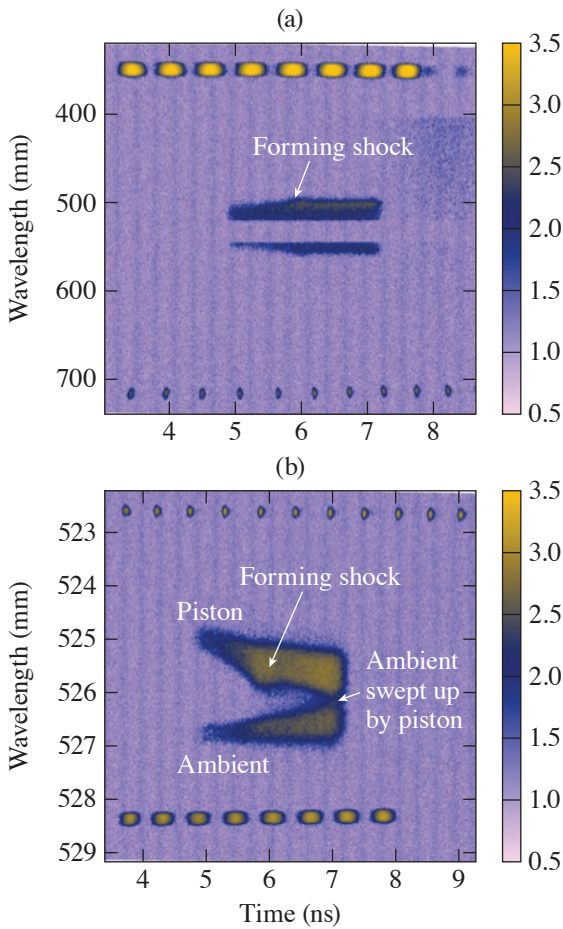
formation of magnetized collisionless shocks. Like reconnection, collisionless shocks are common in space and astrophysical systems. Magnetized shocks form from the nonlinear steepening of a magnetosonic wave and convert highly kinetic supersonic inflows to high-pressure subsonic outflows. In the process, they can also accelerate particles to extremely high energies. Those experiments were recently published in Refs. 2 and 3.

We successfully carried out two NLUF experimental shot days on OMEGA EP and one shot day on OMEGA 60. One shot day on OMEGA EP employed a double MIFEDS-driven coil platform to study particle acceleration from magnetic reconnection in counter-streaming plasmas. The second shot day utilized a flat-foil platform for studying particle energization from Biermann-mediated reconnection. Both platforms were developed for previous NLUF campaigns. The experiments on OMEGA utilized a platform first demonstrated on OMEGA EP in our previous NLUF experiment and deployed both single and double MIFEDS-driven coils to study the formation of collisionless shocks and magnetic reconnection.

The first shot day (November 2017) on OMEGA utilized the Thomson-scattering and proton-radiography diagnostics to measure the temperature, density, flow speed, and magnetic field of both a single plasma plume and counter-streaming plumes interacting with a background magnetic field and ambient plasma (see Fig. 156.61). These measurements continued experiments on OMEGA started in the previous NLUF campaign and complemented previous efforts on OMEGA EP that used proton radiography and angular filter refractometry (AFR) to diagnose large-scale magnetic topology and density profiles. They also provided information on conditions necessary for magnetized collisionless shock formation. We successfully obtained data at a range of times, distances from the target, ambient plasma conditions, and magnetic-field conditions. The results provided direct measurements of magnetized shock formation and are being prepared for submission to *Physical Review Letters*.<sup>4</sup>

The second shot day (February 2018) on OMEGA EP used the recently developed single-channel electron spectrometer (SC-ESM) to study the interaction between expanding plasma plumes and the resulting electron acceleration. We obtained electron spectra, but we were unable to directly measure energized electrons because of the strong MIFEDS-driven magnetic field, which confined the particles to the region near the coils.

The third shot day (May 2018) on OMEGA EP continued the previous experiments on magnetic reconnection between Biermann-battery-generated fields in the expanding plasmas.



U2364JR

Figure 156.61 Streaked Thomson-scattering measurements of the interaction of a piston plasma with a magnetized ambient plasma: (a) electron plasma wave feature and (b) ion-acoustic wave feature. The scattered spectra show the beginnings of shock formation. Afterward, the ambient ions are swept up by the piston and form a hot, high-density downstream region.

We used AFR and the SC-ESM to study the interaction of the colliding plumes and particle energization. We obtained excellent AFR images and electron spectra. SC-ESM observed a population of energized electrons that is consistent with reconnection-accelerated particles but could also be caused by laser-plasma interaction (LPI) effects. Separating these acceleration mechanisms is a topic of present analysis. The AFR will help benchmark simulations.

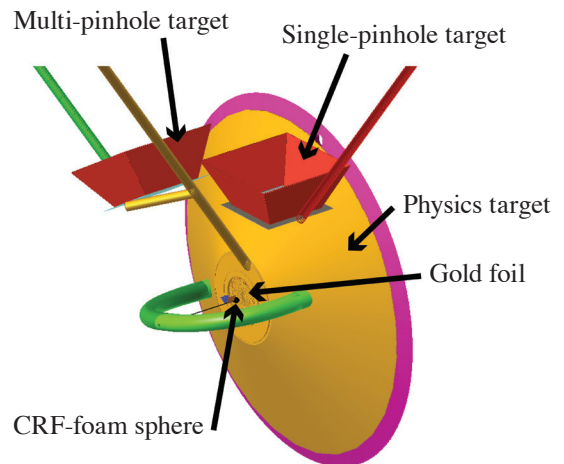
**Experimental Astrophysics on the OMEGA Laser**

Principal Investigator: R. P. Drake (University of Michigan)

We are developing an experimental platform to study processes that occur during the interaction of stellar radiation with molecular gas clouds. Large O- and B-type stars ionize the local

stellar medium, which is then known as an HII region, by emitting huge fluxes of ultraviolet photons. If the ionizing photons encounter a cloud with higher density than the local interstellar medium, then two limiting cases are possible: The first limit occurs when the cloud's optical depth is large to the incident photons. In this limit, photons are absorbed at the cloud's edge facing the star, which acts to asymmetrically compress the cloud. Cloud compression can stimulate the formation of new stars. The second limit occurs when the optical depth of the cloud is small to the incident photons. In this limit, the photons penetrate deep into the cloud where some of the photons are absorbed, which causes heating throughout the cloud. This distributed heating causes the cloud to expand and dissipate.

We are exploring these phenomena in the laboratory by creating a platform that can achieve an appropriate range of optical depths. We use a sphere of carbonized-resorcinol-formaldehyde (CRF) foam to represent the gas cloud and soft x-ray emission from a thin gold foil to represent the stellar radiation source. Our x-ray source produces radiation for several nanoseconds, having a spectrum and intensity that are approximately those of a blackbody at 80 to 100 eV. The platform, shown in Fig. 156.62, enables multiple x-ray backlighters to produce radiographic images of the foam sphere, which is held in a chosen position relative to the gold foil and to shielding required by the diagnostics. Laser-irradiated titanium foils on the backlighter targets create sources of 4.75-keV x rays, which are directed through pinholes toward the sphere and then



U2359JR

Figure 156.62 VisRad model of our experiment. The experiment uses three targets: the physics target, a single-pinhole backlighter target, and a multi-pinhole backlighter target. The physics target contains the gold foil, shielding, the CRF-foam sphere, and fiducial grids.

a detector. We used two orthogonal radiographic lines of sight to obtain up to three radiographs per experiment.

We can scale the optical depth of a sphere across the range of astrophysical interest by varying its density. Our experiments have focused on the large optical-depth limit with an optical depth around 11 by using a 500- $\mu\text{m}$ -diam, 120-mg/cm<sup>3</sup>-density sphere. Figure 156.63 shows a radiograph from such an experiment in which the gold foil was laser driven for 1 ns. In this regime, a shock is expected to form on the side of the sphere closest to the gold foil source. As one can see, the radiograph shows a density increase in the side closest to the gold foil source. We are analyzing these data to infer the areal density of the sphere and compare the observations to the results of simulations. We plan to lower the foam density to achieve optical depths of  $\sim 1$  in future experiments.

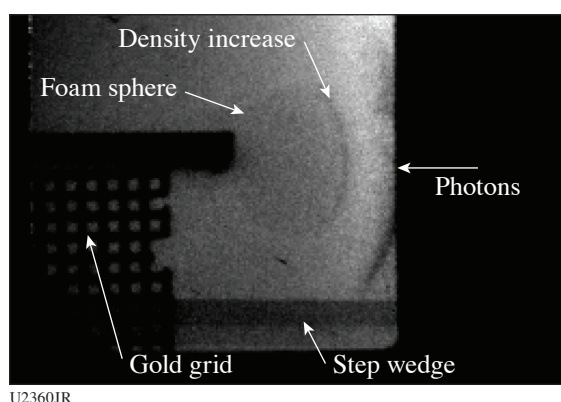


Figure 156.63  
Radiograph of the asymmetric collapse of the sphere generated using a titanium backlighter from a single backlit-pinhole x-ray source. At this experimental time, the sphere's profile is not circular, and a higher-density region is seen in the side of the sphere closest to the gold foil.

### **Structure of Silicon Carbide Ramp Compressed to Multimegabar Pressures**

Principal Investigator: T. S. Duffy (Princeton University)  
Co-investigators: R. F. Smith, F. Coppari (LLNL); J. K. Wicks (Johns Hopkins University); and T. R. Boehly (LLE)  
Graduate Students: D. Kim and S. Han (Princeton)

Carbon planets are a type of exoplanet that are proposed to form around host stars whose composition contains a high ratio of carbon to oxygen. The condensation pathways in protoplanetary disks around such stars are hypothesized to result in the carbide-rich planets in which silicon carbide, SiC, rather than silicates, play a major role in the mantle. The super-Earth planet 55 Cancri e (mass  $8 M_{\oplus}$ , radius  $2 R_{\oplus}$ ) can be described

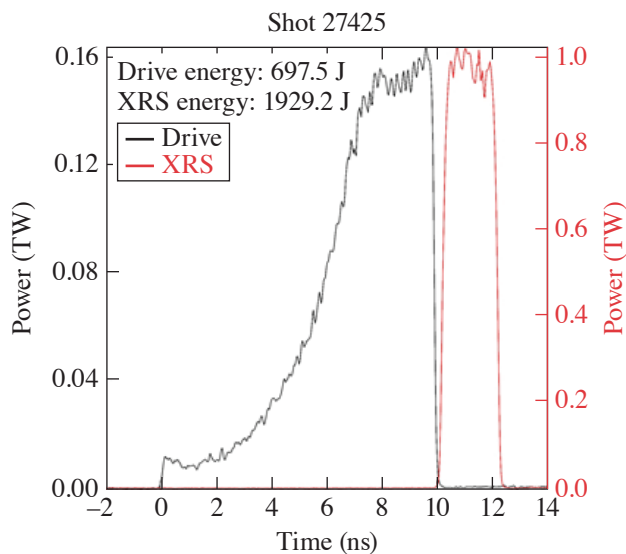
by a carbon-rich interior including SiC. Attempts to model the interior structure of SiC-rich planets are limited, however, by a lack of equation-of-state data for the high-pressure phase of SiC that is formed above 1 Mbar.

Gas-gun shock-wave experiments have provided evidence for a phase transition in SiC beginning around 100 GPa. This transformation is accompanied by a large volume collapse ( $\sim 20\%$ ) and is consistent with the transition from the low-pressure zincblende (B3) phase to the high-pressure rock salt (B1) phase that is also observed in static compression using the diamond-anvil cell; however, the shock-wave data extend only up to  $\sim 150$  GPa with significant scatter above 100 GPa. More recently, the thermal equation of state of SiC was measured using the laser-heated diamond-anvil cell up to 200 GPa. There are no constraints, however, on the behavior of the B1 phase at higher pressures.

Using OMEGA and OMEGA EP, we have carried out x-ray diffraction measurements of SiC using the powder x-ray diffraction image-plate (PXRDIIP) and active shock breakout (ASBO) diagnostics. Commercially purchased SiC powder (1  $\mu\text{m}$ , 99.8% purity, cubic 3C polytype) was prepared as a starting material for the laser-driven ramp compression. The identity of the sample material was confirmed using Raman spectroscopy. Sample pellets  $\sim 10 \mu\text{m}$  thick were produced by compressing the 3C-SiC using a diamond-anvil cell with 0.5- to 1.2-mm culets to 5 GPa to reduce the porosity and increase uniformity. The target assembly consisted of a 10- $\mu\text{m}$ -thick SiC layer sandwiched between a (110) diamond ablator and either a (100) LiF window for low-pressure experiments ( $< 400$  GPa) or a (110) diamond window for higher pressures. For lower-pressure experiments on OMEGA EP, we used a Cu x-ray source paired with either a Ta or W pinhole. A quasi-monochromatic He $_{\alpha}$  x-ray source was generated by driving the Cu foil with a 2-ns square laser pulse (Fig. 156.64). The ASBO was focused at the sample/LiF interface, and the resulting wave profile was used to determine pressure history by fitting with hydrocode simulations. For higher-pressure experiments on OMEGA, a Ge foil was driven with an 8.5-kJ, 1-ns square laser pulse to generate the He $_{\alpha}$  x-ray source. A Pt pinhole was used for these experiments. The VISAR (velocity interferometer for any reflector) was directed at the free surface of the rear diamond. The sample pressure was determined from the measured wave profile by back-integrating using the method of characteristics.

We carried out six successful shots between 100 and 386 GPa and three more shots covering the range from 909 to 1255 GPa. Our lowest-pressure datum ( $\sim 100$  GPa) is consistent

with the low-pressure B3 phase, but all other experiments yield diffraction lines consistent with the (111), (200), and in some



U2362JR

Figure 1156.64

Drive pulse (black curve) for a ramp-compression experiment on silicon carbide producing a peak pressure of 322(14) GPa. The red curve shows the laser pulse used to create a quasi-monochromatic source of He $\alpha$  x rays for x-ray diffraction measurements. The x-ray source (XRS) pulse is delayed relative to the loading pulse in order to probe the sample at the predicted time of peak compression.

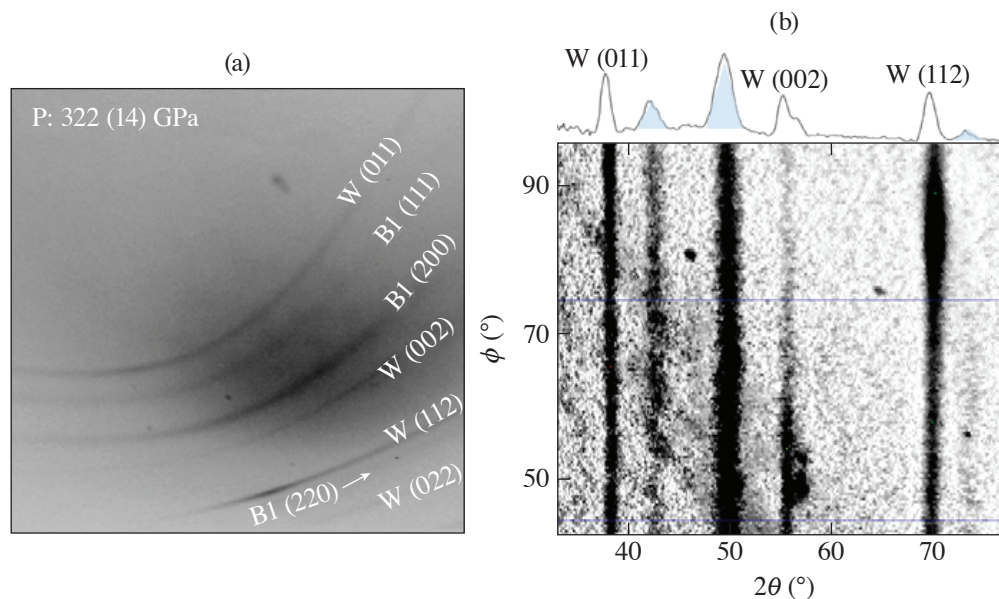
cases the (220) peaks of the rock-salt-type B1 high-pressure phase of silicon carbide (Fig. 156.65). Therefore, we confirm the transformation to the B1 phase under ramp loading as previously identified in shock compression and static experiments. For some shots, however, we observe some additional diffraction peaks whose origin is not yet understood. These will be the subject of further study. We also plan to obtain ramp compression data in the range between 400 GPa and 800 GPa in order to better constrain the high-pressure equation of state of the B1 phase. This will allow us to resolve discrepancies in the extrapolated equation of state from lower-pressure static data, to test theoretical predictions, and to develop models for the interior of 55 Cancri e and other candidate carbon planets.

### High-Energy-Density Chemical Physics and Planetary Evolution

Principal Investigator: R. Jeanloz (University of California, Berkeley)

Co-investigators: M. Millot, D. E. Fratanduono, P. M. Celliers, and J. H. Eggert (LLNL); S. Brygoo and P. Loubeyre (CEA); and T. R. Boehly, G. W. Collins, and J. R. Rygg (LLE)

Our NLUF collaboration aims at documenting the metallization transition of several key constituents of gas giant planets and exoplanets, namely hydrogen, helium, and hydrogen-helium mixtures. During FY18, we conducted five campaigns



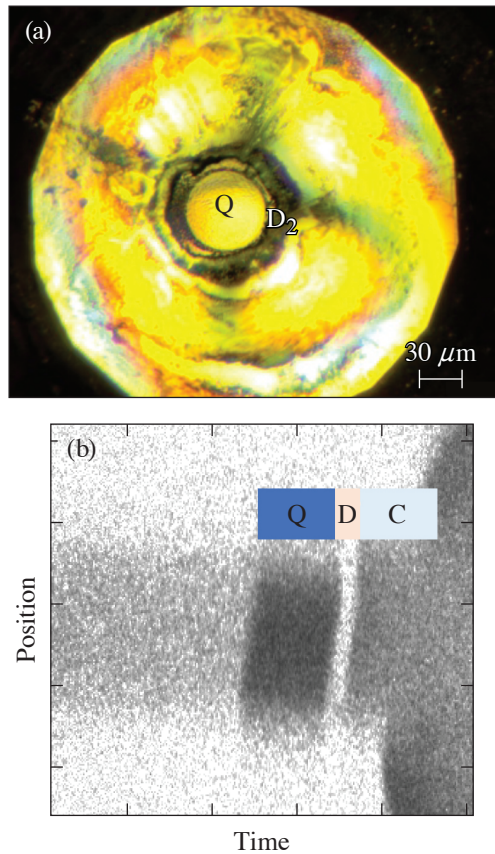
U2363JR

Figure 156.65

Diffraction data for SiC at 322(14) GPa. (a) One of the image plates for OMEGA EP shot 27425. Lines from the tantalum pinhole (used for collimation and calibration) are labeled. Diffraction lines from the sample are indicated with  $hkl$  values. (b) Image-plate data transformed to  $\phi$ - $2\theta$  coordinates, where  $\phi$  is the azimuthal angle around the incident x-ray beam and  $2\theta$  is the diffraction angle. A lineout from the region between the blue horizontal lines is shown at the top. Peaks from the high-pressure B1 phase of SiC are shaded in blue.

with diamond-anvil-cell targets on the OMEGA laser, for a total of 35 shots in a direct-drive geometry.

We used up to 12 beams delivering up to 6 kJ in 1-ns square pulses to the 1-mm aperture in the tungsten carbide seats holding the diamond anvils. VISAR velocimetry and streaked optical pyrometry were used to monitor the shock propagation in the pressurized sample chamber to diagnose the pressure–density equation of state and the optical properties (reflectivity, absorption coefficient) using quartz reference.<sup>5</sup> We focused our efforts on the study of the metallization of hydrogen isotopes using a combination of high precompression and double-shock compression to access high-density states in the vicinity of the predicted first-order transition from the insulating molecular fluid to a metallic atomic fluid. In particular, we successfully fielded targets with solid deuterium precompressed to a record 16 GPa [Fig. 156.66(a)].



U2361JR

Figure 156.66

(a) Image of polygonal-shaped diamond-anvil tip compressing a thin layer of deuterium ( $D_2$ ) above and around a quartz disk (Q) within the pressure chamber. (b) Corresponding streaked optical pyrometry record illustrates the strong difference in radiance between the hot quartz (Q) and diamond (C) layers, and the colder deuterium fluid (D), which stems from the highly elevated initial density state.

Our international team successfully fielded 13 shots with diamond-anvil-cell targets on the OMEGA EP laser during a one-day campaign to investigate the optical properties of dense fluid helium near its metallization. Preliminary analysis of the velocimetry and pyrometry data reveals that accurate measurements of the absorption coefficient can be extracted from the data [Fig. 156.66(b)], which will be useful in benchmarking future improved equation-of-state and planetary models.

Part of this work was conducted at LLNL under Contract DE-AC52-07NA27344.

### Particle Acceleration Caused by Magnetically Driven Reconnection Using Laser-Powered Capacitor Coils

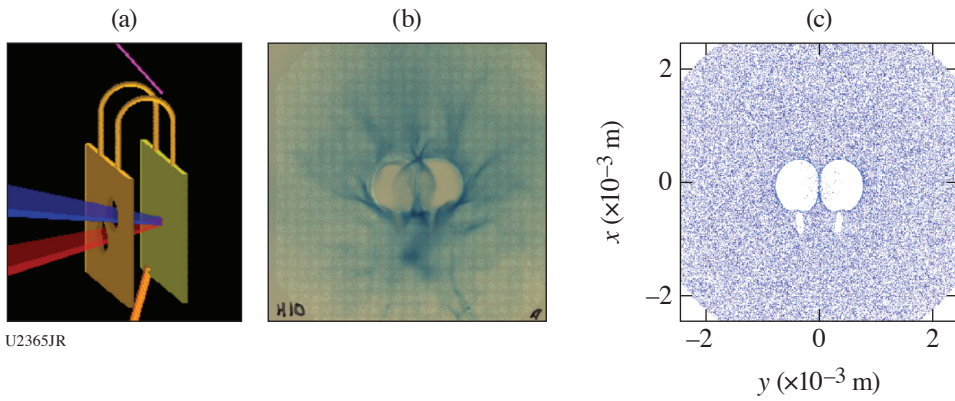
Principal Investigator: H. Ji (Princeton University)

Co-investigators: L. Gao, A. Chien, K. Hill (PPPL); G. Fiksel (University of Michigan); and Q. Lu (University of Science and Technology of China)

Magnetic reconnection is a ubiquitous astrophysical phenomenon in which magnetic energy is rapidly converted into plasma kinetic energy in the form of flow energy and thermal energy, as well as nonthermal energetic particles. The latter is often regarded as an observational signature of the magnetic reconnection, which can be a more efficient generation mechanism than other competing processes such as collisionless shocks. The goal of this NLUF project is to build an effective new platform to achieve and measure conspicuous particle acceleration by magnetically driven axisymmetric reconnection using laser-powered capacitor coils. A long effective path length in this new platform will be provided for particles to be accelerated to high energies and captured by our particle detectors. The experimental results will be quantitatively compared with PIC simulations and interpreted in the context of astrophysical observations.

In FY18, we successfully carried out two experiments on the OMEGA EP Laser System that led to three major achievements of this proposed work:

1. Improved target design for creating reconnection (based on the results from FY17): We improved our target design in FY18, which led to a factor of 2 to 3 stronger current and magnetic-field generation by the coils. Figure 156.67(a) is a schematic showing these new coil targets. Magnetic fields generated by the currents in the two parallel coils of these new targets were measured by ultrafast proton radiography. An example high-profile proton image is shown in Fig. 156.67(b). In the center of the image, there are two proton voids around the coil region resulting from incident protons deflected away by the magnetic fields around the coils. Figure 156.67(c) shows



U2365JR

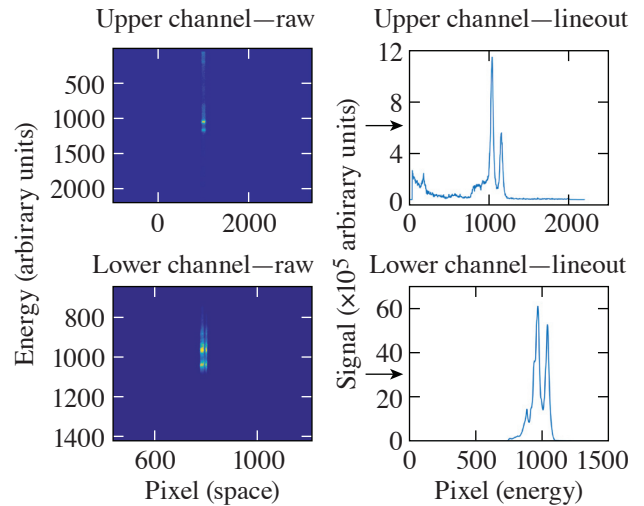
Figure 156.67

(a) The new target design used in our FY18 campaign. (b) Example proton image of the capacitor-coil target. (c) Synthetic proton image calculated by ray tracing.

synthetic proton images with particle ray tracing. By comparing the synthetic proton images with the measured proton data, we were able to determine the current and therefore magnetic-field strength, which is a factor of 2 to 3 larger than those measured in our previous campaigns. By proton probing these targets at various times, the reconnection platform was well calibrated and established. More analysis is underway to focus on understanding other features observed in the proton data. For example, the balloon-like feature in between the two voids is shown to be caused by an in-plane electrical field or out-of-plane current, both of which are direct confirmation of magnetic reconnection.

2. High-resolution x-ray spectroscopy: The newly built OMEGA EP high-resolution x-ray spectrometer was fielded in our experiments to measure Cu  $K_{\alpha}$  emission when the lasers transport through the two holes in the front Cu plate and irradiate the back Cu plate. Figure 156.68 shows example x-ray spectra collected from the upper and lower channels of the spectrometer, where the upper channel uses a charge-coupled device (CCD) and the lower channel uses an image plate as detectors. The energy range covered by the lower channel is higher than that covered by the upper channel. By combining the two channels, we aim to seek hot-electron generation from the intense laser–solid interaction and, therefore, the voltage built by these hot electrons.

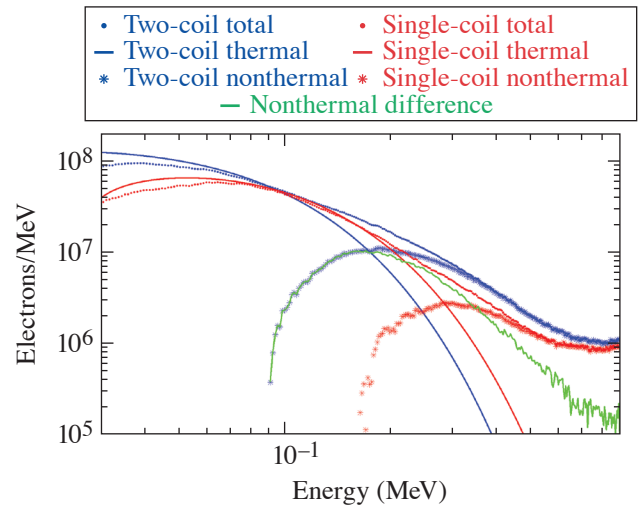
3. Particle acceleration: Energetic electrons generated by magnetic reconnection were successfully measured by the Osaka University electron spectrometer. To definitely confirm that these particles are indeed caused by reconnection, comparison shots were carried out. Figure 156.69 shows the electron spectra from a two-coil reconnection target and a one-coil “no-reconnection” target. Significantly more electrons are observed for the two-coil case, indicating magnetic reconnection has occurred. Each spectrum was fitted to a Maxwell–Boltzmann distribution to represent the thermal



U2366JR

Figure 156.68

High-resolution Cu  $K_{\alpha}$  emission measured from our experiments when the main lasers irradiate a Cu plate in the capacitor coil target.



U2367JR

Figure 156.69

Electron spectra measured from two-coil and single-coil targets.

part, and the nonthermal component is the difference of the measured spectrum to the Maxwell–Boltzmann distribution. The nonthermal difference between the two-coil and one-coil targets, represented by the green curve in Fig. 156.69, is directly caused by magnetic reconnection. PIC simulations of the experiments have been carried out and will be compared to these experimental observations.

### **Proton Radiography of a Highly Asymmetric Magnetic-Reconnection Geometry on OMEGA EP**

Principal Investigators: K. Krushelnick, P. T. Campbell, L. Willingale, and G. Fiksel (University of Michigan); and P. M. Nilson and C. Mileham (LLE)

The laser-driven magnetic-reconnection geometry has been a robust experimental platform for exploring the complex physics underlying this ubiquitous astrophysical phenomenon. Over the past decade, numerous experiments and simulations have studied this geometry in the context of moderate-intensity, nanosecond-class lasers. In previous experimental campaigns, our group extended this platform into the relativistic regime by replacing the long-pulse lasers with short-pulse, high-intensity lasers.<sup>6</sup> For the present work, we adapt the laser-driven reconnection geometry to study a highly asymmetric system. Rather than firing two identical laser pulses side by side, we conducted experiments on the OMEGA EP laser to study a reconnection geometry established by focusing a short-pulse, high-intensity laser alongside a long-pulse UV beam on solid targets.

The high-intensity laser interaction accelerates a population of electrons to relativistic energies. The rapid expansion of

the relativistic electrons generates strong azimuthal magnetic fields (~10 to 100 MG) centered around the laser focal spot that spreads radially across the target with a velocity near the speed of light ( $v_B \approx c$ ). In contrast, the long-pulse, moderate-intensity interaction generates magnetic fields via the Biermann battery mechanism (~1 MG), which expand relatively slowly ( $v_B \approx c_s$ ). This dramatic difference in scales yields a highly asymmetric field geometry, with the rapidly expanding short-pulse-generated field driving into a quasi-static Biermann battery field. In the experiment, a UV beam with a 1-ns pulse duration and 1250 J was focused to an intensity of  $2 \times 10^{14}$  W/cm<sup>2</sup> onto foil targets. After the long-pulse-produced plasma developed, a 10-ps IR pulse with 500 J was focused to relativistic intensity ( $I > 10^{18}$  W/cm<sup>2</sup>) nearby. Proton radiography was used to diagnose the magnetic-field dynamics associated with the asymmetric interaction. A second high-intensity laser pulse with 300 J in 1-ps accelerated protons via the target normal sheath acceleration (TNSA) mechanism. A stack of radiochromic film (RCF) detected the deflection of the proton beam by the electromagnetic fields.

Figure 156.70 shows a schematic representation of the asymmetric reconnection geometry as well as a single-shot proton radiography time series. At  $t_0$ , the Biermann field has evolved for 750 ps when the high-intensity pulse arrives on the 25- $\mu$ m-thick plastic target. In the subsequent time steps, the proton radiography captures the high-intensity magnetic-field generation and the dynamic interaction between the two plasmas. As the magnetic field from the high-intensity pulse drives into the long-pulse-produced plasma, there is evidence of a compression of the initially round magnetic field into a pointed

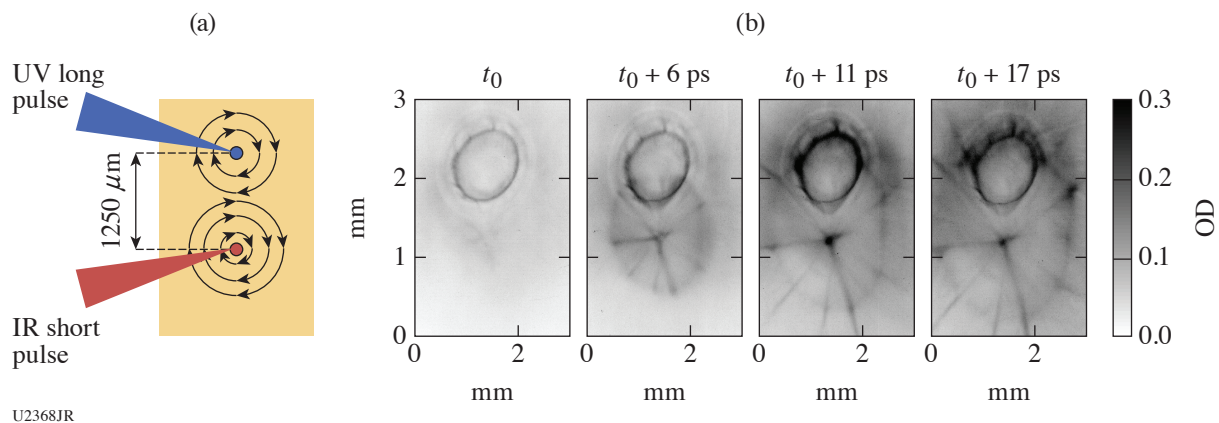


Figure 156.70

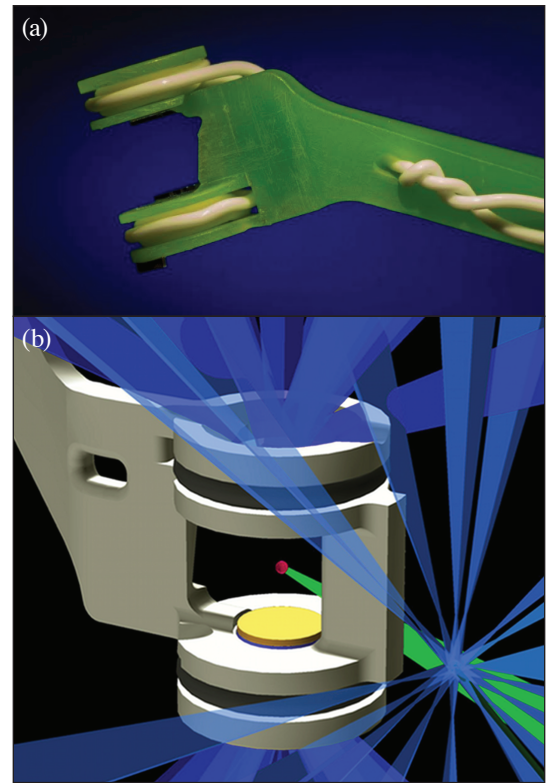
(a) Schematic representation of the experiment demonstrating the asymmetric magnetic-field configuration produced during the experiment. (b) Proton radiography captures the interaction of the rapidly expanding, high-intensity laser-generated magnetic field with the quasi-static Biermann battery field. Regions of higher optical density (OD) correspond to a greater proton flux.

structure at the interface of the two plasmas. In addition, there is an enhancement of proton signal surrounding the Biermann field structures in the region opposite the interface (near the top of the images). These features, as well as the spoke-like structures evident in the high-intensity magnetic field, are the focus of present analysis efforts.

### ***Properties of Magnetohydrodynamic Turbulence in Laser-Produced Plasmas***

Principal Investigator: D. Q. Lamb (University of Chicago)

The second shot day of the TDYNO NLUF Experimental Campaign was carried out on 2 May 2018 using the OMEGA laser. The experiments studied the turbulent dynamo amplification of magnetic fields, a ubiquitous process in astrophysical systems, in the presence of large-scale mean magnetic fields. We deployed a platform [Figs. 156.71(a) and 156.71(b)] similar to the one we fielded on OMEGA for our previous successful TDYNO campaigns (FY15–FY17), during which we (1) demonstrated nonlinear amplification by the turbulent dynamo for the first time in a laboratory environment; (2) quantified the diffusion of energetic charged particles through magnetized turbulence; and (3) characterized the growth rates in the kinematic and nonlinear phases of the turbulent dynamo mechanism. The main augmentation in the TDYNO platform for this shot day was the inclusion of MIFEDS coils [Fig. 156.71(a)] that induced large-scale mean magnetic fields. The magnetic energy of the latter was comparable to the turbulent magnetic energy achieved in previous shot days. The primary goals were to determine the energy cascade of MHD turbulence by measuring the spectrum of both the magnetic field and velocity/density fluctuations, and to characterize and map out the time history and saturation of turbulent dynamo in the presence of a strong background field [Fig. 156.72(b)]. We designed the experimental platform using numerical simulations on one of the nation's leadership supercomputers [Figs. 156.72(a) and 156.72(b)]. The platform is uniquely suited to generating turbulent plasmas in the large magnetic Reynolds numbers ( $R_m$ ) regime, where the dynamo can operate. The configuration consists of two diametrically opposed foil targets and a pair of grids supported by cylindrical shields where the MIFEDS coils rest. The coils are driven well in advance, embedding the target in a background field of  $\sim 100$  kG. The foil targets are then backlit with temporally stacked beams, delivering 5 kJ of energy on each side in a 10-ns span [Fig. 156.71(b)]. The beams drive a pair of counter-propagating, high- $R_m$  plasma flows that carry both the seed magnetic fields generated by the Biermann battery and imposed background field. The flows propagate through a pair of grids that destabilize the flow and



U2369JR

Figure 156.71 TDYNO NLUF Campaign. (a) Experimental platform for the NLUF Campaign to study turbulent dynamo amplification in the presence of a strong background field. The field is applied using MIFEDS coils (white wires). The stalk holding the assembly is crafted via additive manufacturing (green). (b) VisRad schematic of the experimental platform. The target assembly consists of two polystyrene foils and a pair of spatially offset meshes, held together by a pair of cylindrical shields and the MIFEDS stalk. The foils and meshes were carefully designed to optimize the conditions in the interaction region for turbulent field amplification. The shields and flaps protect the interaction region, the imploding  $D^3He$  capsule, and the diagnostics from direct view of the laser spots.

define the driving scale of the turbulence. The flows then meet at the center of the chamber to form a hot, turbulent interaction region [Fig. 156.72(a)], where the magnetic fields are amplified to saturation values [Fig. 156.72(b)].

The shots yielded a wealth of experimental data that made it possible to assess how the MIFEDS background field affects the magnetized turbulence. The predictive power of the *FLASH* simulations and the sheer number of shots we were able to execute (14 in total) allowed us to perform a number of A- to B-type comparisons of the magnetized turbulent state, with and without the MIFEDS background field [Figs. 156.73(a) and 156.73(b)] and at different phases of the temporal evolution of the field amplification [Fig. 156.72(b), red arrows].

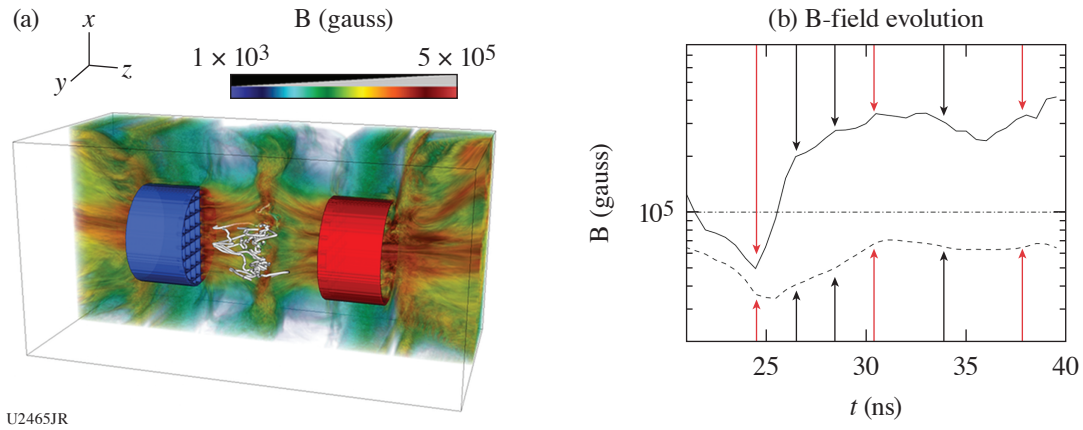


Figure 156.72

(a) Three-dimensional radiation magnetohydrodynamic simulation of the experimental platform, performed with the multiphysics code *FLASH*. A large simulation campaign on Argonne National Lab's *Mira* BG/Q supercomputer guided us in the design of a platform capable of probing the turbulent dynamo regime. The figure displays a 3-D rendering of the magnetic-field magnitude (in gauss), after the jets collide, with sample magnetic-field lines in white. The red cylindrical shield holds the grid that has a hole in its center, whereas the blue shield holds the grid that has a wire in its center. (b) Simulated time history of the magnetic-field strength (in gauss) in the interaction region, showing the kinematic (exponential), nonlinear, and saturation phases of the dynamo for rms and peak values of the magnetic field. The arrows denote the different times at which we fired the proton radiography diagnostic. The red arrows show the times when we performed A-B comparisons with and without the MIFEDS fields. The cadence allowed us to collect enough experimental data to temporally resolve the rise of the magnetic field.

Further, the diagnostics enabled us to fully characterize the turbulent interaction region and quantify its plasma properties in time. More specifically, we used x-ray imaging (Fig. 156.74) to visualize the formation and evolution of the magnetized turbulence and to reconstruct the density power spectrum from the x-ray intensity fluctuations. Moreover, the Thomson-scattering diagnostic yielded information on the plasma state (ion and electron temperatures, bulk flow velocity, turbulent velocity, and electron density) at different times. Finally, we

employed proton radiography on all shots to reconstruct the path-integrated magnetic fields and to recover the time history of the magnetic-field amplification, with and without the MIFEDS fields [Figs. 156.73(a) and 156.73(b)]. The proton radiography data were taken at a 2-ns cadence during the

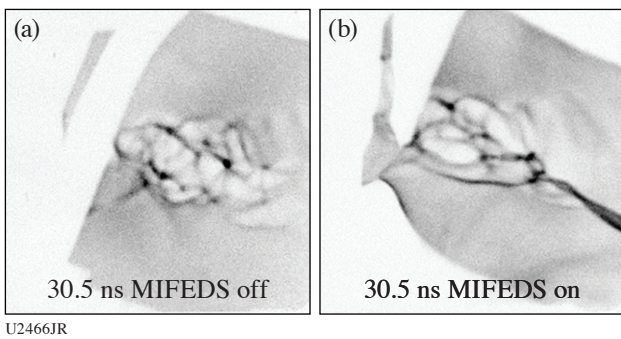


Figure 156.73

(a) Proton radiographs (14.7 MeV) at  $t = 30.5$  ns, corresponding to the time when the field amplification begins to saturate, with the MIFEDS device off. Analysis of the radiographs will reveal the topology and magnetic-field strength that the protons traversed on their way to the CR39 film pack. (b) Same as (a) but with the MIFEDS device on. The filamentary structure differs significantly when the background field is present.

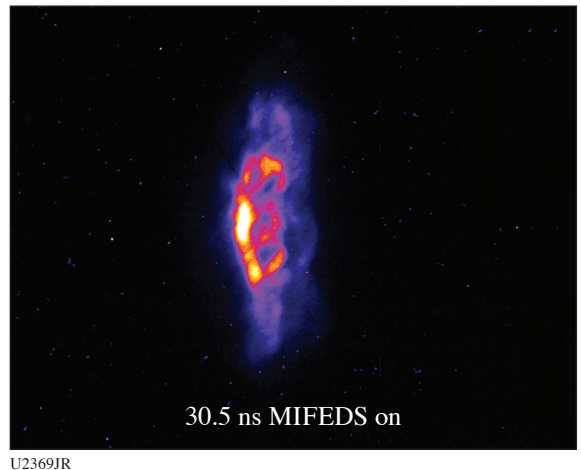


Figure 156.74

(a) X-ray image of the turbulent interaction region for the same shot as in Fig. 156.73(b). The x-ray intensity fluctuations will reveal the power spectrum of the density fluctuations. The wealth of experimental diagnostics has enabled us to characterize the magnetized plasma, study the turbulent dynamo mechanism, and map its temporal evolution in the presence of a strong background field.

kinematic/nonlinear phases of the dynamo, which allowed us to reconstruct the strength and topology of the magnetic field during *all* phases of dynamo amplification [Fig. 156.72(b)] and to recover the growth rate of the turbulent magnetic field. We were also able to dedicate one shot for calibrating the MIFEDS background field, as well as three single-flow shots to assess the magnetic-field advection by the plasma. The experimental data are currently being analyzed and promise to further our understanding of magnetized astrophysical turbulence in the presence of strong background fields.

#### **Development of a Photoionized Plasma Experiment on OMEGA EP**

Principal Investigator: R. C. Mancini (University of Nevada, Reno)  
Co-investigators: R. Heeter and D. Martinez (LLNL) and S. P. Regan (LLE)

The majority of the experiments performed to date on high-energy-density laboratory plasmas pertain to collisional plasmas, i.e., those plasmas where electron collisional processes play a dominant role in the plasma ionization and atomic kinetics. The focus of this project is to study the fundamental atomic and radiation physics of plasmas driven by a broadband intense flux of x rays, i.e., photoionized plasmas. Photoionized plasmas are wide spread in space and found in many astrophysical systems including warm absorbers in active galactic nuclei, x-ray binaries, and the accretion disks surrounding black holes. In these plasmas, the ionization is driven by photoexcitation and photoionization caused by an x-ray flux characterized by a broadband distribution of photons. Yet, in spite of their astrophysical relevance, the increasing number of observations from orbiting telescopes and the complexity of the astrophysical environment, only a small number of laboratory experiments have been done under controlled conditions to test modeling codes and establish what physics models are needed to describe these plasmas. The dearth of laboratory photoionized plasma data is due in part to inadequate x-ray source radiation energy. Recently, this issue has been overcome by using large-scale pulsed-power laser facilities.

We are developing a silicon photoionized plasma experiment for OMEGA EP. This new experimental platform uses a plastic-tamped silicon microdot driven by the 30-ns-duration, broadband x-ray flux produced by the “Gatling-gun” radiation source. This source is comprised of three copper hohlraums that are sequentially driven by three OMEGA EP beams, each one delivering 4 kJ of UV energy in a 10-ns square pulse shape. Each copper hohlraum has a length of 2.8 mm and an inner diameter of 1.4 mm and is filled with TPX foam. The laser

beams sequentially illuminate one hohlraum at a time, thereby producing an x-ray drive characteristic of 90-eV radiation temperature for 30 ns. The silicon microdot has a 1-mm diameter and is placed 7 mm from the source. It has an initial thickness of 0.2  $\mu\text{m}$  and is coated with two 1- $\mu\text{m}$ -thick, 1.5-mm-diam layers of plastic. Figure 156.75 shows the Gatling-gun x-ray source and the silicon microdot sample. Heated by the x-ray flux, the silicon sample expands and ionizes into the L-shell range of silicon ions, i.e., neon- to lithium-like ions, thereby producing a photoionized plasma with an atom number density of a few times  $10^{18}$  atoms/cm<sup>3</sup> and a relatively uniform spatial distribution.

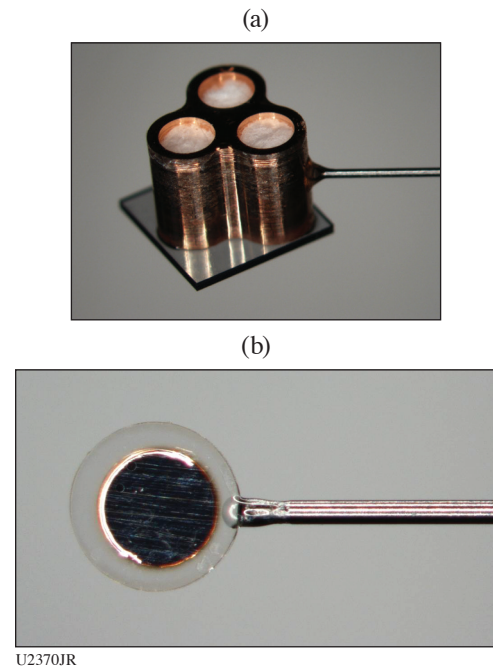
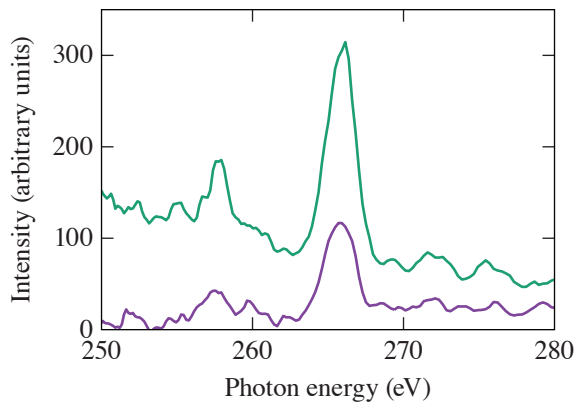


Figure 156.75

(a) Three Cu hohlraum Gatling-gun x-ray sources. (b) The plastic-tamped silicon microdot sample with a 1-mm diameter.

The spatial extension of the blowoff copper plasma from the hohlraums is monitored with the  $4\omega$  probe laser to ensure that it does not reach the silicon sample. The silicon photoionized plasma is probed with emission and absorption spectroscopy. The latter is afforded by a 1-ns-duration, separate titanium backlight source driven by the fourth laser beam of OMEGA EP. This laser beam delivers 1 kJ of UV energy onto a titanium slab target in a 1-ns square pulse shape. Figure 156.76 displays emission from line transitions in B- and Be-like silicon ions recorded at  $t = 6$  ns and  $t = 9$  ns with the gated variable line-spaced grating (VSG) spectrometer in OMEGA EP shot 26079. No measurable line emission in these



U2371JR

Figure 156.76

Photoionized silicon plasma self-emission recorded in OMEGA EP shot 26079 at  $t = 6$  ns (purple curve) and  $t = 9$  ns (green curve). The spectral features at photon energies of 257 eV and 266 eV are caused by L-shell line transitions in B-like and Be-like silicon ions.

ions is noted before  $t = 6$  ns. The x-ray flux starts at  $t = -15$  ns and lasts until  $t = +15$  ns. Therefore, these observations are taken during the second half of the x-ray drive duration. This is reasonably consistent with the pre-shot expectation based on radiation-hydrodynamic modeling of the experiment. The spectra demonstrate the formation of a highly ionized silicon plasma driven by the Gatling-gun broadband x-ray flux. The next step in the development of the experiment is to perform transmission spectroscopy. The absorption spectrum will permit the extraction of the silicon charged-state distribution, an independent check on the temperature determined from the analysis of the L-shell emission spectra, and a test of the photoionization equilibrium condition of the silicon plasma.

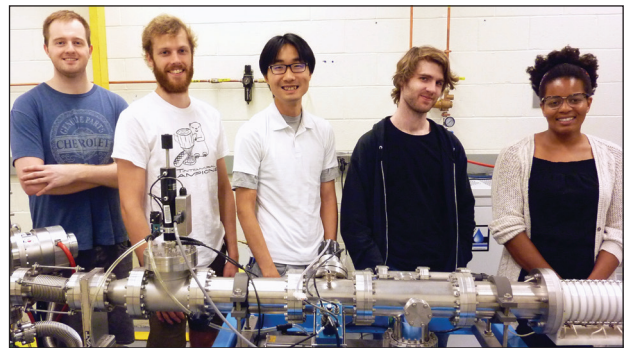
### ***High-Energy-Density–Physics Explorations of Kinetic Physics, Plasma Stopping Power, Hohlraum Fields, and Nuclear Astrophysics***

Principal Investigators: R. D. Petrasso, C. K. Li, and J. A. Frenje [Massachusetts Institute of Technology (MIT)]  
 Co-investigators: F. H. Séguin and M. Gatu Johnson (MIT)  
 Postdocs: C. Parker and A. Bose (MIT)  
 Graduate students: P. Adrian, T. Johnson, N. Kabadi, B. Lahmann, J. Percy, A. Sandberg, R. Simpson, H. Sio, and G. Sutcliffe (MIT)

MIT NLUF work in FY18 has included a wide range of experiments applying charged-particle spectrometry, time-history study of ICF nuclear and x-ray production, and mono-energetic charged-particle radiography methods developed by MIT and collaborators to the study of laboratory astrophysics, high-energy-density physics (HEDP), and ICF plasmas.

Specific major topics where research has produced important results include kinetic and multi-ion-fluid effects on ICF implosion dynamics; ion–electron equilibration in ICF; ion stopping around the Bragg peak in more fully characterized, weakly coupled  $D^3He$  plasmas; ion stopping in warm dense matter; and nuclear reactions and products relevant to stellar and big-bang nucleosynthesis. Twenty-four papers about NLUF-related research were generated in FY18 (Refs. 7–30). There were also many invited talks and contributed talks given at conferences. All of this NLUF work was instrumental in the MIT group being designated a *Center of Excellence* by NNSA as of 2019.

Much of the work was done by award-winning MIT graduate students in the group (see Fig. 156.77), and during the last year the group has welcomed four new participating graduate students and one new postdoc as part of MIT’s long-term program of recruiting and training outstanding Ph.D. students in HEDP and ICF science. Graduate student Hong Sio completed his Ph.D. thesis on “Using Time-Resolved Nuclear Diagnostics to Probe Kinetic/Multi-Ion Physics and Shock Dynamics on OMEGA and the NIF,” based heavily on NLUF work and his development with LLE collaborators of the particle x-ray temporal diagnostic (PXTD), which measures the time history of multiple nuclear burn products and multiple energy bands of x-ray emissions in ICF implosions.<sup>7</sup> Dr. Sio is being nominated for the 2019 *Rosenbluth Outstanding Doctoral Thesis Award* for this work.



U2372JR

Figure 156.77

Five of the six MIT Ph.D. students who won awards for their research during the last year, shown behind the beamline of MIT’s accelerator. From left to right, with their specialties: Patrick Adrian (stopping power and ion–electron equilibration in ICF); Graeme Sutcliffe (tri-particle backlighter program); Hong Sio (PXTD and multi-ion and kinetic effects in ICF); Brandon Lahmann (experimental and theoretical studies of ICF implosion convergence); and Raspberry Simpson (fuel areal-density asymmetries in cryogenic implosions). Missing in this photo is Neel Kabadi (multi-ion and kinetic effects in ICF).

Two important new diagnostic methods have evolved from students' NLUF science experiments this year and will be very important for many future experiments at Omega: The first is "cryoPXTD," which is the PXTD modified with improved optics for cryogenic ICF experiments; it will have 10-ps relative timing accuracy of nuclear-burn and x-ray-emission measurements and will provide measurements of electron temperature as a function of time. The second method is an extension of the monoenergetic charged-particle radiography technique for imaging and analyzing plasmas and their self-generated electromagnetic fields, originally developed by MIT scientists C. K. Li, R. D. Petrasso, and F. H. Séguin (who received the *John Dawson Award for Excellence in Plasma Physics Research* for this work at the October 2017 APS DPP conference). This radiography technique previously utilized a backlighter that supplied 3- and 14.7-MeV protons. Student Graeme Sutcliffe is developing a new tri-particle backlighter that supplies monoenergetic 9.5-MeV deuterons in addition to the 3- and 14.7-MeV protons. This new backlighter will make it possible to simultaneously record three radiographs (one for each particle type), thereby providing new options for separating the effects of self-generated electric and magnetic fields in plasmas.

Individuals from MIT's HEDP Division of the Plasma Science and Fusion Center have carried on other important new physics studies. For example, Dr. Li did innovative and breakthrough studies on astrophysically relevant, electromagnetic collisionless shocks in the laboratory. These studies led to the first-ever demonstration that the structure and dynamics of astrophysical collisionless shocks can be modeled in the laboratory; they also provided new insight into the role of the Weibel instability in electron heating and shock mediation. Dr. Frenje reported on the first accurate validation of ion-stopping formalisms around the Bragg peak in well-characterized high-energy-density plasmas; this has important implications for our understanding of alpha heating in an ICF ignition experiment. Dr. Gatu Johnson used the Omega Laser Facility ICF platform to uniquely study the  $T(t,2n)\alpha$  reaction as a function of center-of-mass (c-m) energy, discovering a hitherto unexpected c-m energy dependence in the shape of the  $T + T$  neutron spectrum.

#### **Study of Magnetized Shock-Formation Experiments**

Principal Investigators: A. Spitkovsky and C. Huntington (Princeton University)

Collisionless shocks are of great importance in astrophysical and space plasmas and occur when the mean free path for

Coulomb collisions between particles is large compared to the size of the shock transition. The shock is then mediated by collective plasma effects caused by interaction between plasma particles and electromagnetic fields. The MagShock Campaign is designed to study the physics of collisionless shocks by sending a stream of high-speed ablated plasma into magnetized, low-velocity plasma that supports an externally applied magnetic field generated by MIFEDS. The setup is shown in Fig. 156.78(a). The experiments used the OMEGA EP laser in which a 3-D-printed Helmholtz coil powered by MIFEDS was inserted. Two targets were mounted on MIFEDS. A 400-J to 800-J, 1-ns pulse was used to ablate plasma that propagated along the coil magnetic field (this component is called "background" plasma). A 1.3-kJ, 1-ns pulse was used to drive fast flow orthogonal to the magnetic field [this component is called "piston" plasma, see Fig. 156.78(b)]. The interaction between the flows was expected to drive a compression in the background plasma and the magnetic field. At a strong-enough drive, this compression becomes a collisionless shock. We diagnosed this compression using proton radiography with TNSA from a short, 1-ps laser pulse. The protons were recorded on CR-39 film, which was our primary diagnostic. On some shots, a  $4\omega$  optical probe was also utilized.

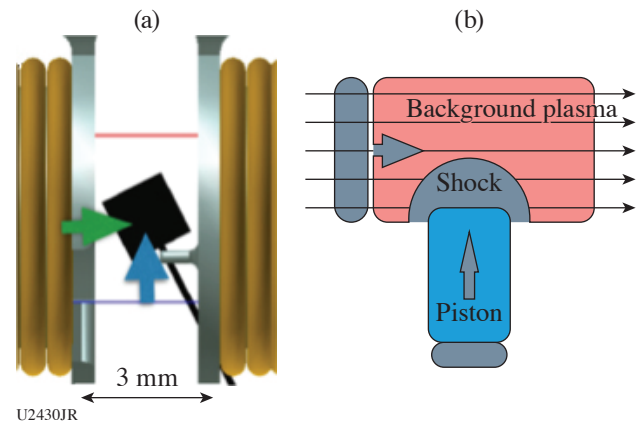


Figure 156.78

(a) Experimental setup for MagShock-EP-18A. (b) Schematic of the fast piston plasma interacting with a magnetized background plasma.

The OMEGA EP shot day on 5 May 2018 was used to collect data with the  $4\omega$  and proton-radiography diagnostics to complement data collected on previous shot days. We used proton radiography on seven shots to image the magnetic shock propagation across the system. The  $4\omega$  optical diagnostic was used to characterize the laser-driven plasmas, providing clear signatures of the expanding plasma plumes. The experiment was accompanied by a significant modeling and simulation

campaign, which allowed us to interpret the data as a detection of a magnetized collisionless shock propagating through the plasma. The main feature of the magnetic compression in the data was the appearance of a proton-deficit band in the proton image, indicating additional deflection of the protons. The band was followed by a sharp caustic of enhanced proton concentration [Figs. 156.79(a)–156.79(c); shots separated by 1 ns]. Simulations allowed us to model the distortions in proton images because of realistic MIFEDS fields [seen as distortion in the squares of Fig. 156.79(d)], and to measure the speed of the shock and its Mach number. Further 3-D simulations helped us to understand the asymmetries in the interaction between the two plumes [Fig. 156.79(e)]. These findings will be presented at the APS DPP meeting in November 2018 as two oral contributions.

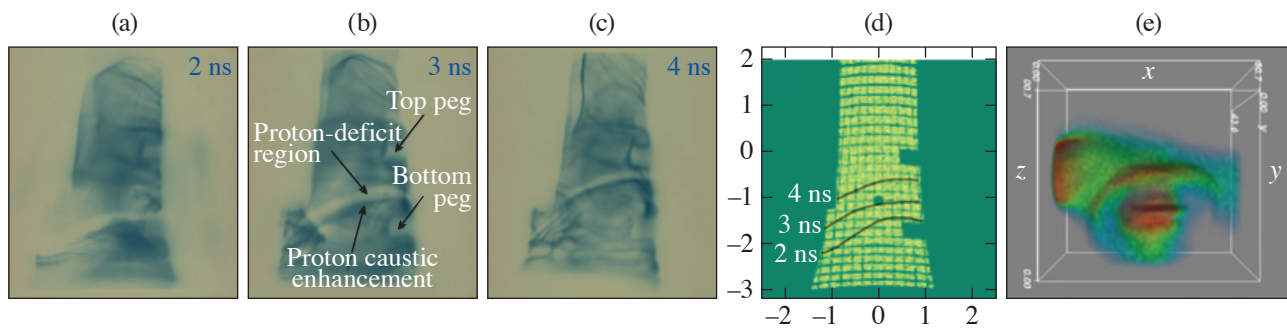
We thank OMEGA EP personnel for their assistance in planning and executing this campaign.

**Demonstration of a Talbot–Lau X-Ray Deflectometry Electron Density Diagnostic in Laser–Target Interactions**  
Principal Investigator: D. Stutman (John Hopkins University)

Simulations and theory have failed to accurately predict electron density profiles and dynamics of ablating plasmas. Talbot–Lau x-ray deflectometry (TXD) will provide electron density information in ranges not available today ( $<n_c$ ) and will therefore advance the field of HED science. The main goal of demonstrating TXD electron density retrieval in HEDP experiments is compatible with the goal of advancing the understanding of plasma ablation of irradiated foils. The

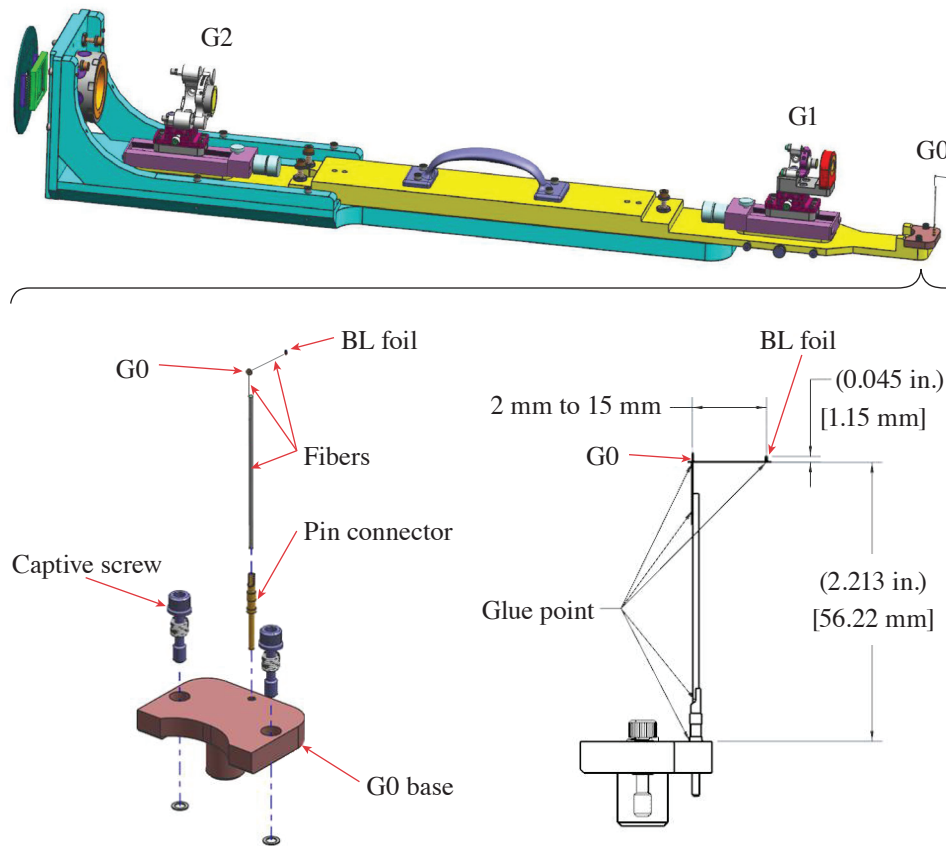
OMEGA EP experiments have been defined in collaboration with P. A. Keiter and R. P. Drake from the University of Michigan. Previous experiments have confirmed TXD potential as a basic and widespread diagnostic for HEDP experiments. In order to benchmark the technique, the interferometer must be tested in the presence of a plasma target. To this aim, a CH foil will be irradiated by three UV OMEGA EP beams. A fourth beam will be used to obtain an x-ray backlighter source, which will illuminate the Talbot–Lau deflectometer, providing an electron density map of the ablated foil.

The proposed two-year research includes the implementation of a Talbot–Lau x-ray deflectometer on the OMEGA EP laser. Preparatory experiments have been performed on the Multi-Terawatt (MTW) laser (FY17) to test and optimize the x-ray backlighter and Laboratoire pour l'Utilisation des Lasers Intenses (LULI) (FY18) to test grating survival and detector performance. The first year focused on diagnostic design and experiment preparation in collaboration with C. Stoeckl and S. P. Regan (LLE). The diagnostic design was completed (Final Design Review, April 2018), while the assembly of TXD is underway, coordinated by C. Sorce and C. Mileham from the LLE diagnostics group. The experimental campaign has been moved to Q1 FY19 considering rail assembly and testing delays resulting from manufacturer increased lead time for vacuum-compatible and special-order components. The ten-inch manipulator design is shown in Fig. 156.80. Similar to laboratory, MTW, and LULI setups, all gratings are mounted on a common rail. This allows one to accurately pre-align the gratings on site, pre-shot.



U2431JR

Figure 156.79 [(a)–(c)] Proton radiography of the interaction at different times. Notice the movement of the white proton-deficit band and the sharp caustic feature behind it. (d) Simulation of distortions of the equally spaced lattice at target chamber center caused by proton bending in MIFEDS fields. This simulation was used to measure the speed of the shock feature. (e) Three-dimensional simulation of the collision between background and piston plasma showing the origin of asymmetries in the interaction.



U2373JR

Figure 156.80  
Conceptual design of the TXD diagnostic for the OMEGA EP experiments. The inset shows source grating details.

### Hot-Electron Generation and Laser-Plasma Instabilities in Shock-Ignition Conditions

Principal Investigator: M. S. Wei (General Atomics, now at LLE)  
Co-investigators: C. M. Krauland (General Atomics); S. Zhang, J. Li, and F. N. Beg (UCSD); C. Ren, W. Theobald, D. Turnbull, D. Haberberger, C. Stoeckl, R. Betti, and E. M. Campbell (LLE); J. Trela and D. Batani (CELIA); R. Scott [Science and Technology Facilities Council (STFC), UK]; L. Antonelli (University of York); and F. Barbato (EMPA, Switzerland)

Shock ignition (SI) is an alternative ICF concept designed to achieve ignition by launching a strong convergent shock after low-velocity fuel compression. The experimental platform includes the use of an  $\sim 10^{16}$ -W/cm<sup>2</sup> laser pulse to directly (through collisional absorption) or indirectly (through LPI-induced hot electrons) generate this strong shock. In either scenario, the feasibility of SI depends on the hot-electron populations created during this high-intensity laser pulse. In FY18, we conducted two experiments to systematically characterize hot-electron generation in an SI-relevant regime.

Comparison data from planar targets fielded on both OMEGA and OMEGA EP show the impact of overlapped UV beams. On OMEGA EP, we used long-pulse beams with  $2$  to  $4 \times 10^{14}$ -W/cm<sup>2</sup> total irradiance to generate a  $\geq 1$ -keV CH plasma with  $L_n \sim 300$ - $\mu$ m scale length. Between 1 to 1.5 ns after the beginning of this lower-intensity pulse, a single tightly focused UV beam is injected into the plasma with  $10^{16}$ -W/cm<sup>2</sup> vacuum intensity. Figure 156.81 shows this experimental setup and the target design used on both laser systems. On OMEGA, 20 overlapped UV beams are incident on the ablator with a pulse shape that has a 2-ns foot for plasma creation followed by a 300-ps higher power spike. The spike portion of the pulse provides an overlapped beam intensity of  $1.5 \times 10^{16}$  W/cm<sup>2</sup> to be reached during that time.

Bremsstrahlung data suggest that the overlapped UV lasers produce more hot electrons than a single UV beam of comparable intensity. Laser-to-hot-electron conversion efficiency in the overlapped beam case is  $5 \pm 2\%$  with  $T_{\text{hot}} = 24 \pm 2$  keV; in

the single-beam experiment, we observed only  $2 \pm 1\%$  energy conversion with  $T_{\text{hot}} = 45 \pm 5$  keV. The lower hot-electron temperature and higher energy conversion efficiency may be more beneficial to the SI goal since it would increase the pressure of an electron-driven shock and reduce the required laser energy.

The spectrum of scattered light from both experiments suggests that hot electrons are generated mainly from stimulated Raman scattering (SRS). Figure 156.82 shows data from the single-beam experiment, where the SRS signal indicates strong pump depletion in the lower-density plasma during the

first 0.5 ns of the high-intensity interaction. This is evidenced by scattering observed only in the sub- $0.1-n_c$  region when the beam is initially injected.

A second experimental goal achieved in an OMEGA/OMEGA EP joint shot day this year was to measure the impact of pulse duration for high-intensity IR beam interactions with SI plasmas. We fielded Cu foam spherical targets coated with  $30 \mu\text{m}$  CH. All OMEGA beams irradiated the CH followed by either a single 100-ps OMEGA EP IR beam or two co-propagating OMEGA EP IR beams overlapped in space but stacked

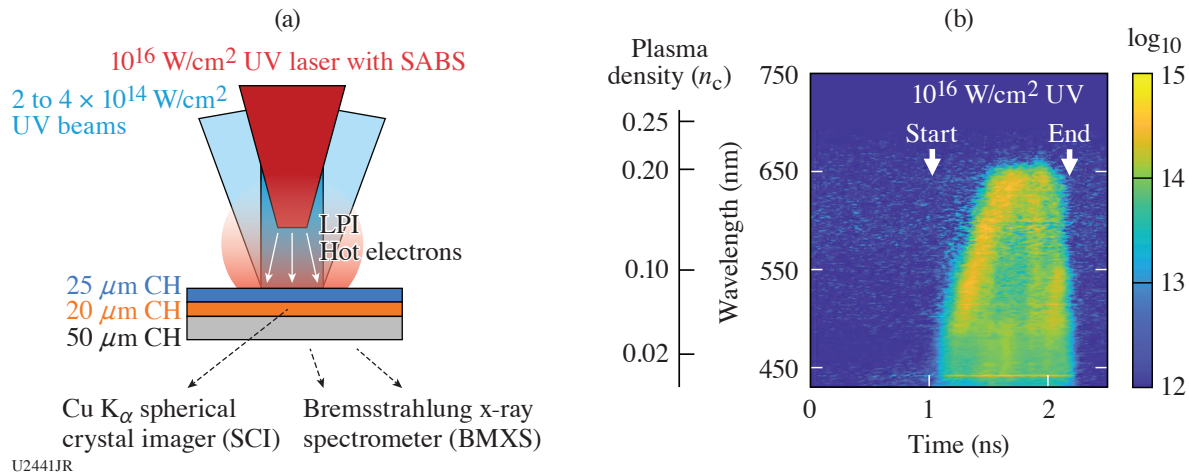


Figure 156.81

(a) Experimental platform for OMEGA EP shots. Two lower-intensity UV lasers are used to create the plasma, after which we inject one high-intensity UV beam. The sub-aperture backscattering spectrometer (SABS) observes light from the high-intensity interaction beam. (b) Spectrum of the backscattered light in the single UV beam experiment. T-0 designates the start of the plasma creation beams. The high-intensity UV pulse is injected at 1 ns.

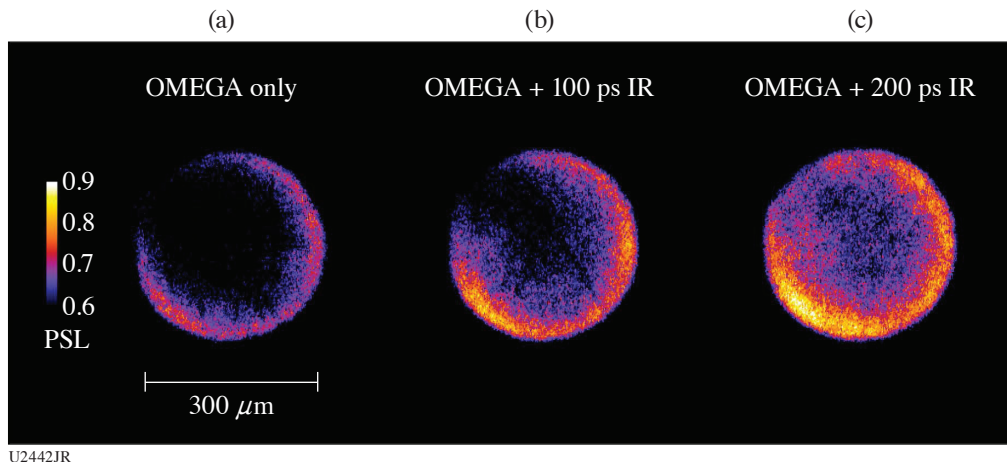


Figure 156.82

Two-dimensional images of Cu fluorescence from (a) the spherical crystal imager for the plasma-creation beams only, (b) the 100-ps OMEGA EP IR beam, and (c) the stitched co-propagating OMEGA EP IR beams for a 200-ps pulse duration.

in time to create a 200-ps pulse. Bremsstrahlung spectra show the 200-ps duration produced hot electrons with  $T_{\text{hot}} \sim 55$  keV at a conversion efficiency of 4%, while the 100-ps IR beam generated electrons with  $T_{\text{hot}} \sim 90$  keV converting only 2% of the laser energy. Near-monochromatic images from Cu  $K_{\alpha}$  fluorescence illustrate these findings in Fig. 156.82. For reasons similar to overlapped UV beams, these results suggest longer-pulse IR beams would be more beneficial for shock ignition.

**FY18 Laboratory Basic Science (LBS) Program**

Fifteen LBS projects previously approved for FY17 target shots were allocated Omega Facility shot time and conducted a total of 231 target shots at the Omega Laser Facility in FY18 (see Table 156.X). The FY18 LBS experiments are summarized in this section.

During FY18, LLE issued a solicitation for LBS proposals for beam time in FY19. A total of 39 proposals were submitted, about 1.4x more than the previous year, showing strong interest and high demand of Omega Laser Facility time for basic HED experiments from both NNSA ICF laboratories (LLNL, LANL, SNL, NRL, and LLE) and the Office of Science-funded national

laboratories such as SLAC and Princeton Plasma Physics Laboratory (PPPL). An independent committee reviewed and ranked the proposals; on the basis of these scores, 20 proposals were selected in the first round and allocated 21.5 shot days at the Omega Laser Facility in FY19. With the FY19–FY20 NLUF solicitation being delayed (no DOE solicitation in FY18), six additional LBS proposals (based on their scores) were allocated six shot days to partially replace the eight shot days in Q3FY19 that were originally reserved for new NLUF experiments. One of those six LBS proposals was also re-categorized as an ICF experiment following the LBS Review Committee’s recommendation. Table 156.XI lists the approved FY19 LBS projects with a total allocation of 26.5 shot days at the Omega Laser Facility.

***Probing Heterogeneous Dynamic Fracture and Failure Using 2-D Velocimetry***

Principal Investigator: S. J. Ali (LLNL)  
 Co-investigators: P. M. Celliers, R. F. Smith, J. H. Eggert, and D. Erskine (LLNL)

Studies on the time scale and morphology of fracture dynamics, which can occur over micron-length scales and

Table 156.X: LBS experiments conducted at the Omega Laser Facility in FY18.

Principal Investigator	Institution	Title
S. J. Ali	LLNL	Effect of Grain Size on the Dynamic Failure of Diamond
H. Chen	LLNL	Exploring the Applications of Laser-Produced Relativistic Electron–Positron Pair-Plasma Jets
T. Doeppner	LLNL	Equation-of-State Measurements of Shock-Heated Foams Using X-Ray Thomson-Scattering Fluorescence
S, Jiang	LLNL	Characterizing Pressure Ionization in Ramp-Compressed Materials with Electron-Induced Fluorescence
A. Krygier	LLNL	Shock Metamorphism and Lattice Deformation Kinetics in Meteor Impact
T. Ma	LLNL	Proton Isochoric Heating for Warm-Dense-Matter Studies
E. V. Marley	LLNL	Radiative Properties of an Open L-Shell, Non-LTE Plasma
P. M. Nilson	LLE	Applying Marshak Waves to the Iron Opacity Problem
H.-S. Park	LLNL	Study of High-Alfvénic Mach Number Plasma Dynamics and Magnetized Shocks
D. N. Polsin	LLE	Structure and Melting of High-Pressure Sodium
M. J. Rosenberg	LLE	Electron Energization During Magnetic Reconnection in High-Energy-Density Plasmas
J. R. Rygg	LLE	Atomic and Electronic Structure of Warm Dense Silicon
R. F. Smith	LLNL	Thermal Conductivity of Fe and Fe-Si at Earth Core Conditions
W. Theobald	LLE	Shock Formation and Hot-Electron Preheating in Planar Geometry at Shock-Ignition–Relevant Laser Intensities
A. B. Zylstra	LANL	Charged-Particle Stopping Power Near the Bragg Peak

time scales of a nanosecond or less, have generated a lot of interest in recent years, but experimental limitations have not permitted simultaneous measurements on these time and length scales.<sup>31–35</sup> This series of shots combines the 1-D [OMEGA active shock breakout (ASBO)] and 2-D [OMEGA high-resolution velocimeter (OHRV)] velocimetry diagnostics to study heterogeneous flow and the formation of fracture networks in diamond. The 1-D VISAR (velocity interferometer system for

any reflector) records the compression history of the sample, providing absolute velocity and pressure, while the 2-D OHRV captures picosecond snapshots of the spatially resolved velocity and reflectivity maps.

All four campaign half-days used half-hohlraum indirect drive to launch a spatially smooth shock wave into either single-crystal aluminum, single-crystal diamond, or poly-

Table 156.XI: LBS experiments approved for target shots at the Omega Laser Facility in FY19.

Principal Investigator	Institution	Title
F. Albert	LLNL	Laser-Wakefield Electron Acceleration and Betatron Radiation on OMEGA EP
H. Chen	LLNL	Exploring the Application of Laser-Produced Relativistic Electron–Positron Pair-Plasma Jets
H. Chen	LLNL	Laboratory Model of Particle Acceleration in Supernova Shocks
K. Flippo	LANL	Characterizing Magnetized Turbulent Plasmas: Toward Generating Laboratory Dynamo
C. J. Forrest	LLE	Evaluation of Neutron-Induced Breakup with Light-Z Nuclei at $E_n = 14.03$ MeV at the Omega Laser Facility
W. Fox	PPPL	Turbulent Transport in Magnetized High-Energy-Density Plasmas
D. E. Fratanduono	LLNL	Investigating Giant Impact Between Rocky Planets with High-Pressure Melting and Shock Equation-of-State Measurements on Complex Silicates
A. Gleason	SLAC	Viscosity Measurements Using Tracer Particles
S. Glenzer	SLAC	High-Yield Neutron Pulses from Deflagrating Convergence in Hohlraums
X. Gong	LLE	Structure and Melting of High-Pressure Sodium and Potassium
M. Gorman	LLNL	Phase-Transformation Kinetics—Strain Rate Tuning of the Peierls Distortion in Ramp-Compressed bct Sn
B. Henderson	LLE	Optical Spectroscopy of High-Pressure Sodium
S. X. Hu	LLE	Uncharted Territory: Testing the Predictions of Density Functional Theory in Warm and Extremely Dense Plasmas
L. C. Jarrott	LLNL	Using Line-Intensity Enhancements to Characterize NLTE Plasmas
S. Jiang	LLNL	Characterizing Pressure Ionization in Ramp-Compressed Materials with Fluorescence and Absorption Spectroscopy
G. Kagan	LANL	Probing Electron Distribution in Spherical Implosions with Hard X-Ray Spectroscopy
S. Khan	LLNL	Absolute Equation-of-State Measurements of Low-Density Foams Toward Studying the Landau–Darrieus Instability in High-Energy-Density Conditions
A. Krygier	LLNL	The Strength of Fe and Fe-Si 16 wt% at the Conditions in the Earth's Core
E. Marley	LLNL	Radiative Properties of an Open L-Shell, non-LTE Plasma
M. Millot	LLNL	A Journey to the Center of Uranus and Neptune: Using X-Ray Diffraction to Unravel the Atomic Structure of New Solid and Superionic Ices at Multi-Megabar Pressures
Z. Mohammed	LLE	Study of Gamma-Ray Products from reactions Relevant to Big-Bang Nucleosynthesis
J. Moody	LLNL	Developing an Ultrahigh-Magnetic-Field Laboratory for High-Energy-Density Science
H. G. Rinderknecht	LLE	Structure and Scaling of Strong Collisional Plasma Shocks
R. Saha	LLE	Measurements of Warm Dense Matter Based on Angularly and Spectrally Dispersed X-Ray Scattering
W. Theobald	LLE	X-Ray Phase-Contrast Imaging of Strong Shocks in Foam Targets

crystalline diamond. Over the course of the first campaign, DiamondFailure-18A, it became apparent that the dichroic mirror used to reflect the 532-nm ASBO probe and transmit the 400-nm OHRV probe was being damaged, most likely by unconverted light. This resulted in distorted images and velocity maps in the OHRV and a loss of reflected light into the ASBO. A redesign of the mirror holding with additional shielding was completed for 18B and refined slightly for 18C and 18D, resulting in a robust platform for making simultaneous OHRV and ASBO measurements with no unusable shots for 18C and 18D.

Overall, the campaign yielded excellent data showing orientation-dependent fracture in the single-crystal Al and diamond and potential intergranular fracture in the polycrystalline diamond. This suggests that over the pressure and strain rate regime observed, the fracture is primarily driven by slip planes in the single-crystal samples.

Some initial results, primarily from DiamondFailure-18C, are highlighted in Fig. 156.83. In Figs. 156.83(b) and 156.83(d) (the single-crystal samples), linear features were seen in both the image and velocity map coinciding with the predicted slip plane motion for 100-oriented aluminum and diamond. In the Fig. 156.83(d) aluminum data, it is also apparent that there is an evolution in the deformation pattern with the most linear features toward the lower left corner, closer to the center of the drive spot and higher in pressure by  $\sim 2$  GPa relative to the upper right corner. Further analysis is required to determine whether this evolution is a result of time or pressure. In the polycrystalline sample [Fig. 156.83(c)], a distribution of features of  $\sim 20$ - $\mu\text{m}$  average size was observed, with lower-velocity regions between the velocity map and discontinuity-like features in the image. Since the grain size for these samples is  $\sim 10$  to  $20$   $\mu\text{m}$ , this is commensurate with fracture occurring at the grain boundaries, where the velocity is measurably lower. Results of these campaigns are still being analyzed, with a publication planned for mid-FY19.

### Exploring Pair Plasmas and Their Applications

Principal Investigator: H. Chen (LLNL)

In FY18, an LLNL/General Atomics/University of Michigan team carried out two LBS shot days on OMEGA EP. The campaign used an OMEGA EP short-pulse beam to produce jets of electron–positron antimatter pairs, while the second short-pulse beam was used to produce protons to diagnose the laser–target interactions. The experiments focused on (1) enhancing the pair yield using nanostructured targets and

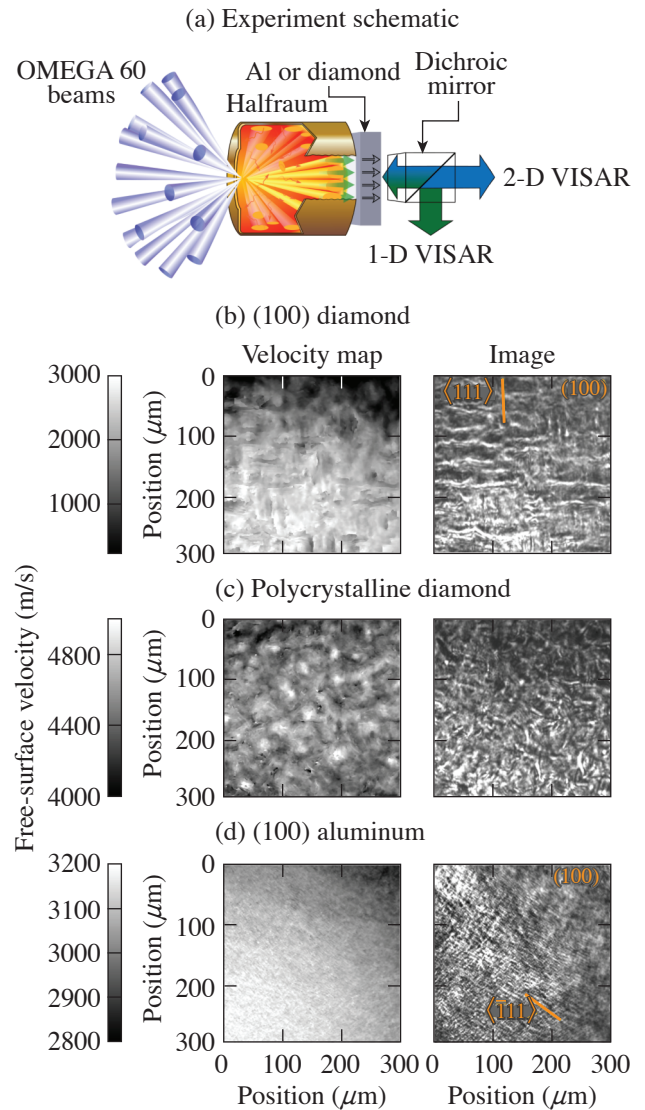


Figure 156.83

(a) Experimental configuration. OHRV velocity maps and images for (b) 120-GPa single-crystal diamond, (c) 160-GPa polycrystalline diamond, and (d) 30-GPa single-crystal aluminum.

(2) collimating and/or focusing positron jets through curved sheath potentials from shaped target surfaces. The experiments successfully demonstrated both yield enhancement and positron focusing. The data provided the basis for future experiments on laboratory astrophysics using the pair jet–plasma interaction to drive beam instabilities. A total of 14 shots were performed in the fiscal year.

The OMEGA EP short-pulse beams ( $\sim 1$  kJ in 10 ps) irradiated 1-mm-thick Au targets with and without the nanostructure on the laser interaction surface. It was found that for the

same laser energy, positron yields and acceleration were both increased dramatically by using nanostructure.<sup>36</sup> This finding is important to future experiments and applications using laser pair jets. Previous experiments used gold targets almost exclusively. It was also found that a hemispherical-shaped back surface can focus the positron jets through the sheath field—similar to that observed in proton focusing. This observation is important since it demonstrated that higher pair density can be achieved by reducing their volume, which may enable the development of instabilities predicted by theory.

Prior experiments showed that quasi-monoenergetic relativistic positron jets are formed during high-intensity irradiation of thick gold targets,<sup>37,38</sup> and that these jets can be strongly collimated<sup>39</sup> using the magneto-inertial fusion electrical discharge system (MIFEDS).<sup>40</sup> The external field produces a 40-fold increase in the peak positron and electron signal.<sup>39</sup> The positron yield was found to scale as the square of the laser energy.<sup>41,42</sup> The FY15 results revealed another dimension of scaling on the target materials. The favorable scaling would enable the laboratory study of relativistic pair plasmas that are important to understanding some of the most exotic and energetic systems in the universe.<sup>42,43</sup>

#### **Development of Platform to Benchmark Atomic Models for X-Ray Spectroscopy of Shock-Heated Materials**

Principal Investigators: T. Doepfner and M. J. MacDonald (LLNL)

Co-investigators: A. M. Saunders, C. M. Huntington, H. A. Scott, K. Ma, K. B. Fournier, D. S. Montgomery, and O. L. Landen (LLNL); S. R. Klein and R. W. Falcone (LBNL); P. X. Belancourt, H. J. Lefevre, C. C. Kuranz, and E. Johnsen (University of Michigan); and W. Theobald (LLE)

The FoamXRFTS-18A Campaign was the first shot day in a collaboration to develop a platform using simultaneous x-ray fluorescence (XRF) spectroscopy and x-ray Thomson scattering (XRTS) to measure the equation of state of shocked foams. The goal of this platform is to provide XRF spectroscopy data from shock-heated materials at known temperatures, measured independently using XRTS, to benchmark atomic models for future XRF diagnostics.

This platform uses a planar shock wave to heat a cylinder of foam doped with a mid-Z element, similar to previous results published from the Trident Laser Facility at LANL,<sup>44</sup> with the addition of an XRTS diagnostic. A laser-driven Zn He $_{\alpha}$  backlighter (1) induced K-shell fluorescence from the Co-doped

foam and (2) served as the x-ray source for XRTS. The imaging x-ray Thomson-scattering (IXTS) spectrometer recorded spatially resolved Co K $_{\beta}$  XRF, measuring the density profile of the shock wave in the foam in addition to resolving XRF spectra from the shocked and unshocked regions of the foam. The Co K $_{\beta}$  spectra from the shock-heated layer can be modeled using atomic kinetic and radiation codes to infer temperatures, electron densities, and ionization-state distributions. These results will be compared to temperatures measured using XRTS on the ZSPEC spectrometer to improve atomic models used in XRF modeling at similar conditions. This first campaign demonstrated the ability to spatially resolve XRF spectra in a single shot [Fig. 156.84(a)] and measure changes in the Co K $_{\beta}$  shift by varying the drive intensity [Fig. 156.84(b)]. Shielding issues with the XRTS measurement were resolved by the end of the shot day, and a follow-up experiment is planned for December 2018 (FoamXRFTS-19A).

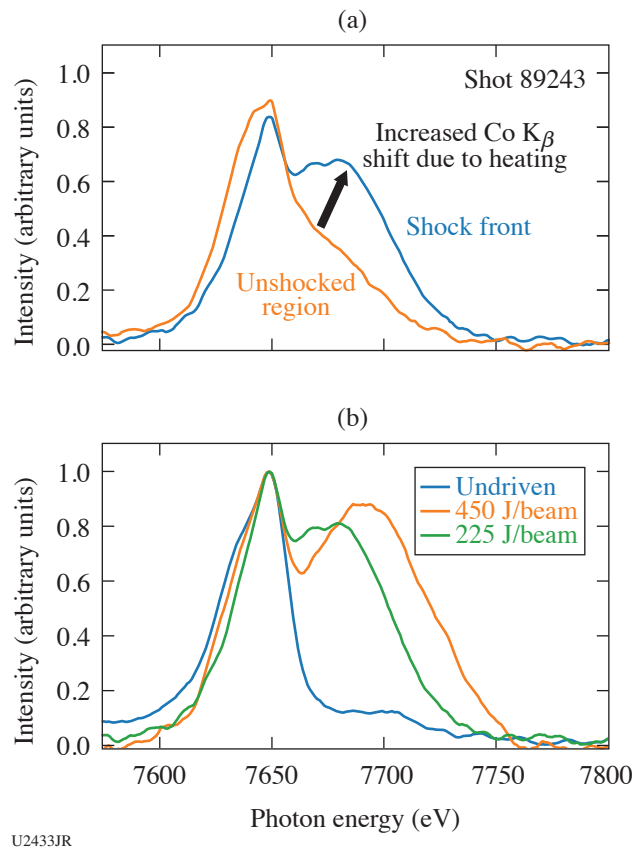


Figure 156.84

(a) Spatially resolved Co K $_{\beta}$  spectra taken ahead of the shock front (unheated) and at the shock front (heated). (b) Co K $_{\beta}$  from unshocked foam (blue curve) and at the shock front for the full drive showing the largest shift (orange curve) and half drive with a smaller shift (green curve).

**Characterizing Pressure Ionization in Ramp-Compressed Materials with Electron-Induced Fluorescence**

Principal Investigator: S. Jiang (LLNL)

Co-investigators: Y. Ping, R. Smith, A. Jenei, and J. H. Eggert (LLNL)

This pressure ionization campaign, which comprised one day on OMEGA EP during FY18, was designed to measure ionization in compressed Co as a function of density using the K-shell fluorescence spectroscopy. A schematic of the experimental setup is displayed in Fig. 156.85(a). The K-shell line emissions were induced by hot electrons generated through short-pulse laser–solid interactions. A large, thick Al target was used to avoid heating from the short pulse. The high pressure was achieved by ramp compression using the long-pulse drivers so that the temperature was kept low during the compression process. During the experiment, the pressure history was characterized with VISAR measurements. The target structure is also shown in Fig. 156.85(a). Despite the Co layer under study, the targets also included a thin Cu layer as an energy reference. The shots varied the driver intensities to reach different densities without raising the thermal ionization effect and reached up to 2.0 to 2.2× compression with maximum long-pulse energy. There is still little consensus on pressure ionization under these conditions despite extensive theoretical and experimental efforts.

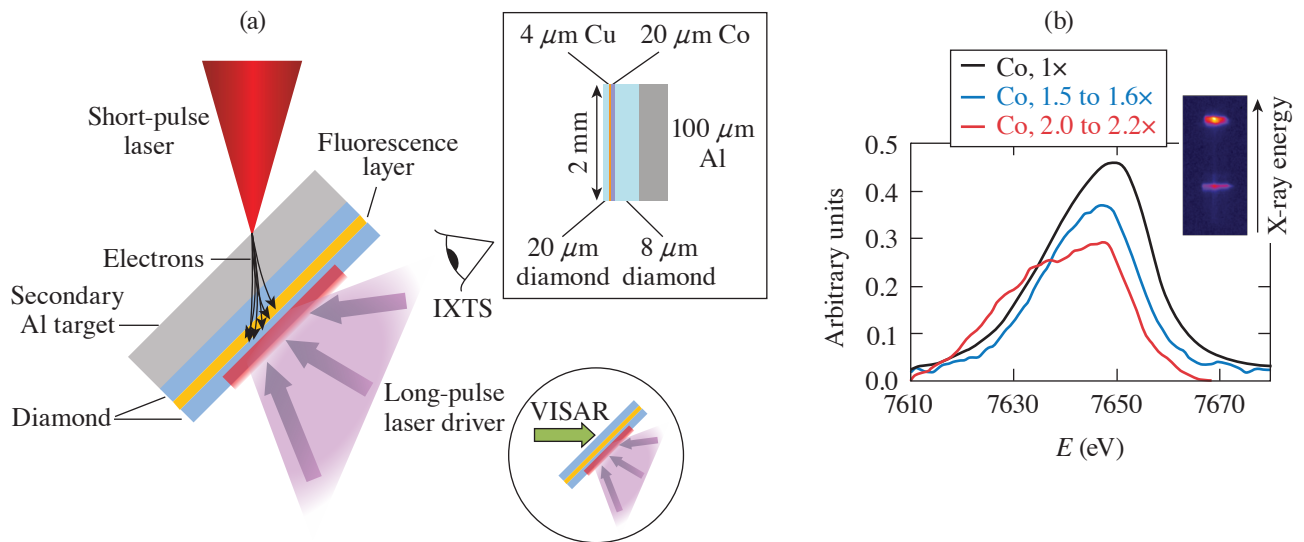
The main diagnostic used in this campaign was a high-resolution x-ray spectrometer IXTS. It successfully measured the Cu  $K_{\alpha}$  and Co  $K_{\beta}$  fluorescence lines with high signal-to-noise ratio as can be seen in Fig. 156.85(b). Under the designed experimental conditions, pressure ionization has a much more prominent effect on the outer M shell compared to inner shells (K and L shells). Therefore, the Cu  $K_{\alpha}$  line is predicted to have a negligible energy shift, while the Co  $K_{\beta}$  line is more prone to a shift. Figure 156.85(b) shows the measured Co  $K_{\beta}$  peaks under different compressions. A small red shift was observed under 2.0 to 2.2× compression, which is contrary to the prediction of the Ecker–Kroll ionization model. This campaign provided a direct and unambiguous measurement of the pressure ionization effect for benchmarking various ionization models.

**Laue Diffraction and Recovery of Shocked Single-Crystal Quartz**

Principal Investigator: A. Krygier (LLNL)

Co-investigators: C. Wehrenberg, A. Gleason, H.-S. Park, and B. Remington (LLNL)

As the second most abundant mineral in the continental crust, SiO<sub>2</sub> (quartz) plays a large role in the dynamics of meteor impacts on Earth. Quartz has become the most important material for identifying meteor sites due to the wide range of permanent shock effects including the formation of polymorph-



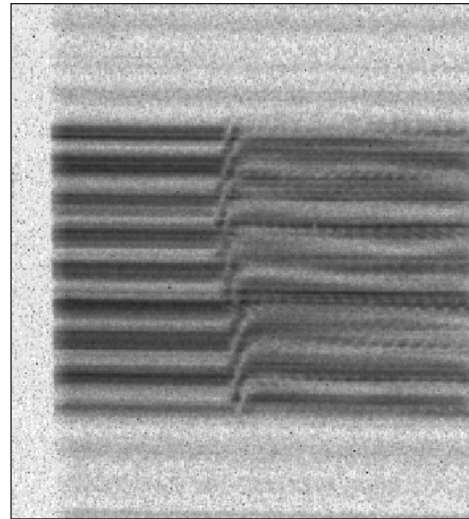
U2434JR

Figure 156.85

(a) A schematic of the experimental configuration. The inset at the top right shows the target geometry. The inset at the bottom right shows a schematic of the VISAR configuration. (b) Measured IXTS spectra of Co  $K_{\beta}$ . The lineouts are from different driver conditions. An example of the raw image is shown in the inset.

like stishovite and coesite. This campaign performed *in-situ* Laue diffraction of shocked, high-purity, single-crystal samples combined with *ex-situ* recovery analysis of a range of shocked natural samples, as illustrated in Fig. 156.86. Laue diffraction is a powerful tool for characterizing crystalline lattice dynamics in compressed samples, and recovery analysis enables a wide range of sophisticated materials science techniques.

These shots produced Laue diffraction of *z*-, *x*-, and *y*-cut quartz samples shocked to ~10 to 50 GPa and recovered natural samples shocked to over 100 GPa. Laue diffraction is a direct measure of the orientation of crystal lattice planes, and the configuration allowed direct measurement of the strain anisotropy during the shock. The x rays are produced by an imploded CH capsule that generates a smooth, broadband, 100-ps x-ray flash at stagnation. The sample conditions are determined by the ASBO diagnostic, with sample data shown in Fig. 156.87.



U2436JR

Figure 156.87  
Raw ASBO data.

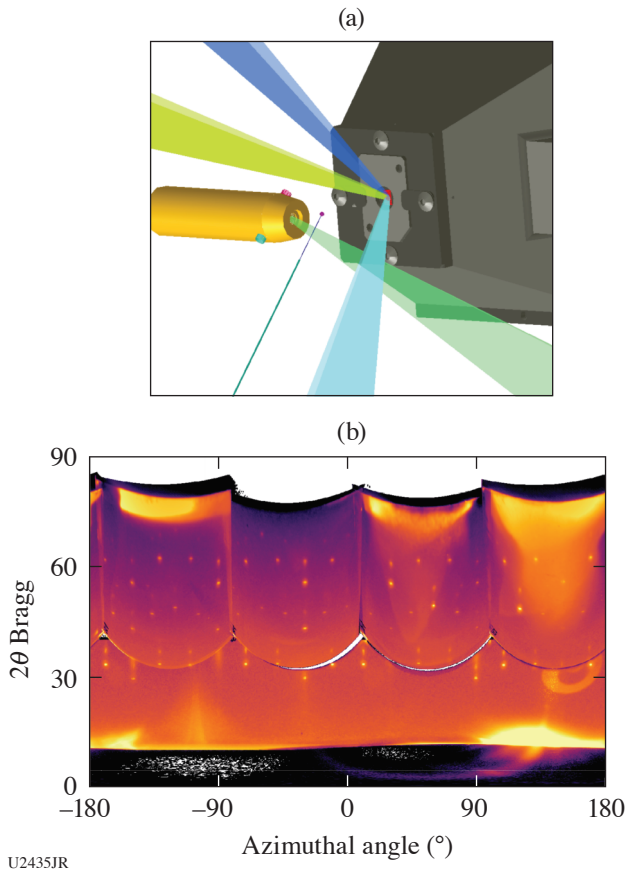
This experiment yielded 12 shots of extremely high-quality Laue diffraction and successfully recovered samples. Analysis is underway with publications to follow.

**Proton Isochoric Heating for Warm-Dense-Matter Studies**

Principal Investigators: T. Ma and D. Mariscal (LLNL)  
Co-investigators: G. J. Williams, H. Chen, and S. Wilks (LLNL) and C. McGuffey and J. Kim (UCSD)

High-intensity proton beams driven by multipicosecond, kilojoule-scale lasers are an effective means to rapidly heat solid targets into the warm-dense-matter (WDM) state.<sup>45</sup> OMEGA EP short-pulse-driven proton beams containing 20 to 50 J at proton energies >3 MeV can be rapidly (<50 ps) deposited into solid-density samples, heating them to >100-eV temperatures before significant hydrodynamic expansion can occur (i.e., solid density).

CH hemispherical targets (15- $\mu\text{m}$  thick  $\times$  375- $\mu\text{m}$  radius of curvature) were driven by OMEGA EP short-pulse beams defocused to  $R_{80} \sim 45 \mu\text{m}$  at 3-, 6-, and 10-ps pulse lengths at 800 to 1000 J in order to focus proton beams to Cu samples (15- or 50- $\mu\text{m}$  thick  $\times$  200- $\mu\text{m}$  diameter). A radiochromic film stack and a Thomson-parabola instrument were used to monitor the transmitted ion sources for each shot. Both low-resolution (zinc von Hamos) and high-resolution (HiResSpec) x-ray spectrometers measured Cu  $K_{\alpha}$  and  $K_{\beta}$  emission to infer the temperature of the heated samples. At temperatures of >50 eV, significant shifts in Cu  $K_{\alpha}$  are expected; and at ~200-eV



U2435JR

Figure 156.86  
(a) Experimental setup with a broadband x-ray Laue diffraction (BBXRD) diagnostic (gray) and shock-recovery tube (yellow) to recover intact shock-compressed samples for *ex-situ* analysis. (b) Laue diffraction data.

temperatures, Cu  $K_{\beta}$  shifts and depletions are also expected. The laser pulse length was varied to find an optimum between laser-to-proton conversion efficiency and the optimum proton beam spectral characteristics for heating. Additionally, the Cu sample position was moved closer and farther from the proton source to look for an optimal proton beam focus for heating.

A very successful day was completed with 13 shots (1 diagnostic calibration and 12 heating). A preliminary look at the data indicates that heating was optimal at longer laser pulse lengths (6 or 10 ps) and highest when the CH tamping surrounding the Cu samples was removed, as evidenced by the appearance of higher charge states, as seen in the shaded region of Fig. 156.88(c). Data analysis is ongoing, where detailed spectral analysis and particle-in-cell (PIC) modeling will enable quantitative temperature measurements.

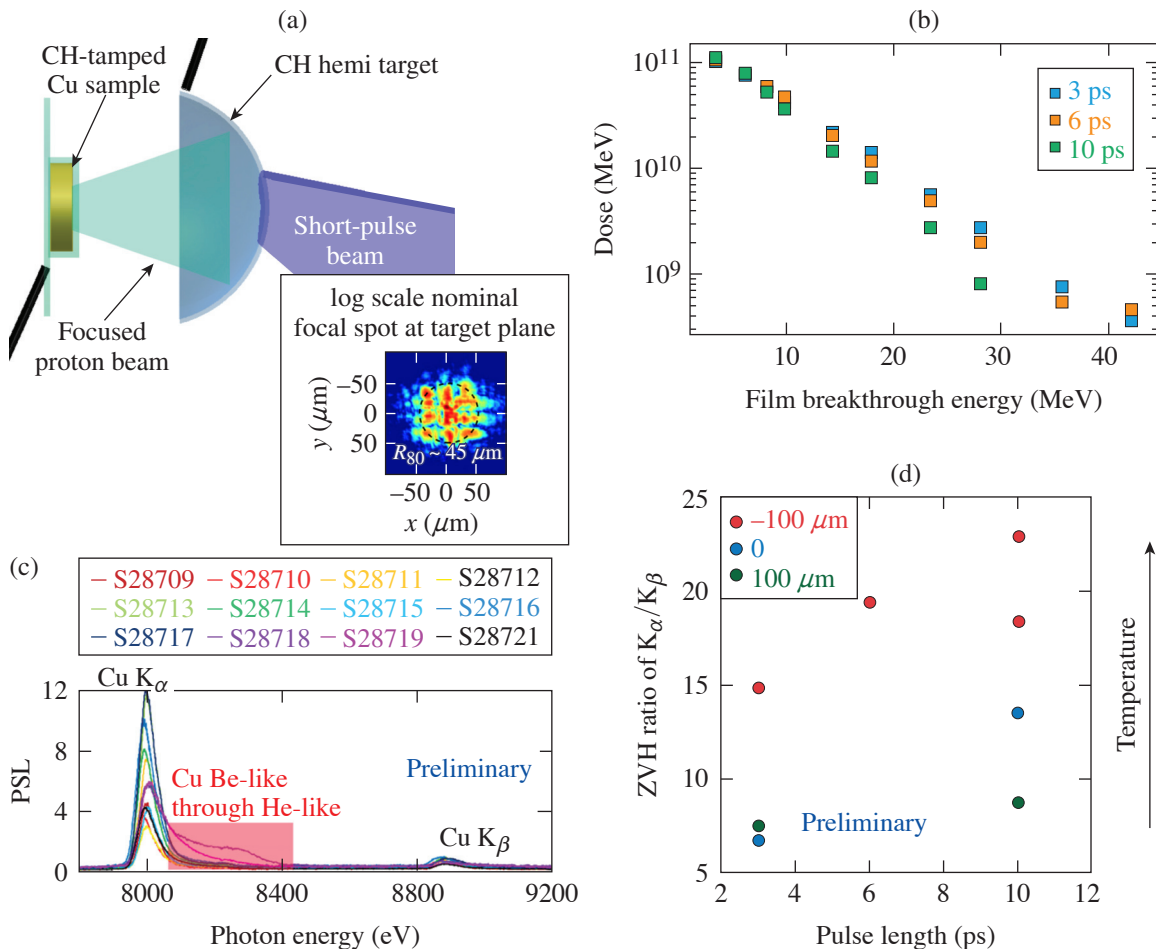
**Time-Resolved Measurement of the Radiative Properties of Open L-Shell Germanium**

Principal Investigator: E. V. Marley (LLNL)

Co-investigators: L. C. Jarrott, M. B. Schneider, G. E. Kemp, M. E. Foord, R. F. Heeter, D. A. Liedahl, K. Widmann, C. W. Mauche, G. V. Brown, and J. Emig (LLNL)

This campaign was designed to measure the emitted L-shell germanium spectra from a well characterized and uniform plasma for comparison to atomic kinetic models. Recent studies have shown a discrepancy between atomic kinetic models and high-Z M-shell spectral data. This study was done to test the accuracy of models for L-shell emission.

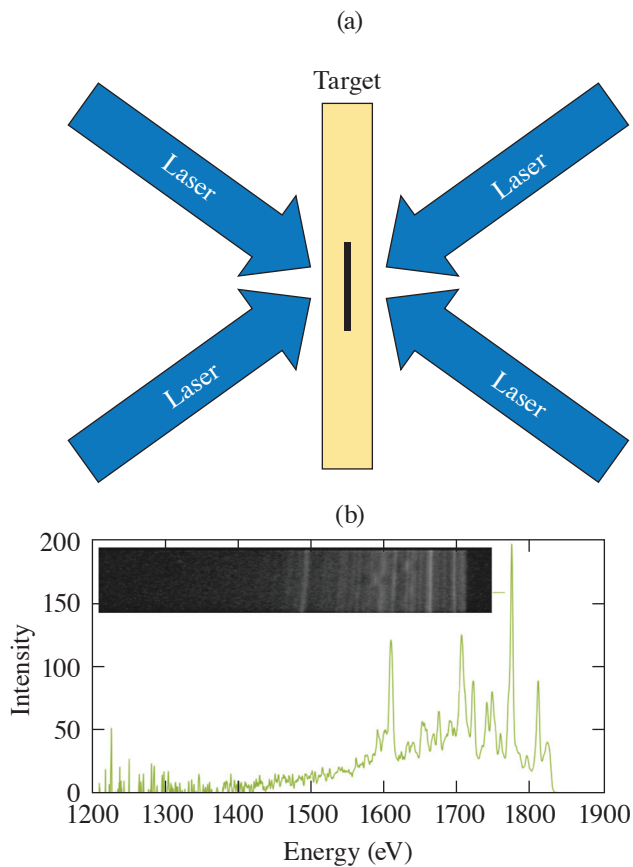
In two OMEGA shot days, planar buried-layer targets were illuminated evenly on both sides (Fig. 156.89) to heat



U2437JR

Figure 156.88

(a) Experimental configuration and defocused laser spot (inset). (b) Transmitted proton dose in radiochromic film (RCF) stacks show the differences in proton beam spectra versus pulse length. (c) Raw zinc von Hamos (ZnVH) data for all heating shots show the differences in Cu  $K_{\alpha}$  and  $K_{\beta}$  yield and shape. (d) Integrated Cu spectra ( $K_{\alpha}$ : $K_{\beta}$ ) show an increase in temperature with increasing laser pulse length and decreasing distance from hemi to Cu sample.



U2438JR

Figure 156.89

(a) Experimental configuration. (b) Time-resolved Ge L-shell spectra with data inset of shot 90543 at 2.6 ns.

the sample, composed of Sc and Ge layers. The first shot day used samples with Ge layers surrounding a single Sc layer in the center. The second shot day placed Sc layers surrounding a single Ge layer. This verified that the target was heating through, and the same conditions could be reached on both shot days. These layers were embedded between two 5- $\mu\text{m}$ -thick layers of Be tamper, which slows the sample expansion. Time-resolved 2-D images of the target's x-ray emission, viewed both face-on and side-on, were recorded using time-gated pinhole cameras. Gated Sc K-shell spectra from a crystal spectrometer were obtained to determine the electron temperature of the plasma. A second gated crystal spectrometer recorded the Ge L-shell emission at four times. During the second shot day, streaked Ge L-shell spectra also provided a continuous record of the ion population shift in time. A third gated spectrometer, which utilized a variably spaced grating and a slit, provided time- and space-resolved Ge L-shell spectra and also verified the uniformity of the plasma at different times during the experiment. All of the framing cameras used for imaging and

spectroscopy were co-timed so the plasma conditions could be determined for the measured Ge L-shell spectra.

The first shot day tested two different pulse shapes: a 3-ns square pulse and an identical pulse preceded by a 100-ps picket. The latter was used to generate a pre-plasma before the arrival of the main pulse, creating a smoother interface for the laser-plasma interaction and more-efficient coupling of energy into the target. The second shot day used a 3.5-ns square pulse with a picket to deposit the same energy into the target over a longer time. Complete data from all six co-timed diagnostics were recorded on both days at temperatures  $\sim 1.5$  keV. Detailed analysis is in progress and expected to result in future publications.

### *Changes in the Electronic Structure of Dense, High-Temperature Materials*

Principal Investigator: P. M. Nilson (LLE)

Co-investigators: S. X. Hu, G. W. Collins, and J. R. Rygg (LLE)

Graduate Student: D. A. Chin (LLE)

Changes in the electronic structure of highly compressed materials are being explored with high-resolution x-ray spectroscopy on the OMEGA Laser System. The goal is to test atomic-scale models that estimate changes in the x-ray absorption features and fluorescent line emission from dense, high-temperature materials. How atomic physics may be altered in these conditions is crucial for gauging the opacity and equation of state of materials under compression and is of fundamental importance to the study of stellar interiors, planetary cores, and inertial fusion.

The experimental setup uses direct laser ablation of a 30- $\mu\text{m}$ -thick plastic shell to compress a buried metal-doped layer. The target design is shown in Fig. 156.90 (inset). A slow, moderate-convergence (8 to 10) implosion is used. The plastic shell has three layers: a 17- $\mu\text{m}$  CH ablator, a 10- $\mu\text{m}$  CH layer doped with 2 or 4 at. % Cu, and an inner 3- $\mu\text{m}$  CH layer. At stagnation, the hot spot serves as an x-ray source for transmission measurements of the compressed shell. To increase the brightness of the core, the target contains a 20-atm  $\text{D}_2$  Ar (0.1 or 1 at. %) fill. One-dimensional radiation-hydrodynamic model predictions suggest the Cu-doped layer can be compressed by a 27-kJ, 1-ns drive to 20  $\text{g}/\text{cm}^3$ , reaching a temperature of  $\sim 200$  eV.

An example time-integrated x-ray emission spectrum from these experiments is shown in Fig. 156.90. The target had a 20-atm- $\text{D}_2$  Ar (0.1 at. %) fill and a buried, 10- $\mu\text{m}$ -thick CH layer doped with 4 at. % Cu. The data show x-ray emission

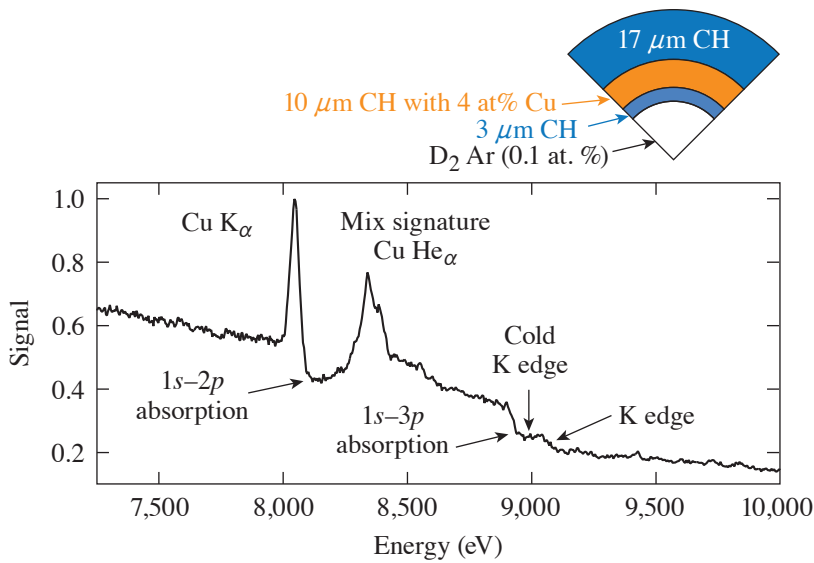


Figure 156.90  
Measured, time-integrated x-ray absorption and fluorescence features from a slow, moderate-convergence implosion containing a Cu-doped layer. The target design is shown in the inset.

U2374JR

and absorption features consistent with the creation of dense, high-temperature conditions in the compressed shell. The Cu K-edge shape and spectral shift relative to the cold K edge is observed, together with Cu K $\alpha$  emission and resonant 1s-3p and 1s-2p self-absorption features. Cu He $\alpha$  emission is measured, indicative of some fraction of the Cu dopant reaching the high-temperature core. Data from targets with a lower Cu-dopant fraction showed significantly reduced He $\alpha$  emission, indicating likely more stable buried-layer dynamics. Detailed analysis of the data and comparisons to spectroscopic modeling is underway.

Future work will extend these measurements to include thicker shells and other dopant materials and mixtures, including Fe, Ni, and Ti, as well as higher-resolution x-ray spectroscopy and imaging. This experiment has provided an important quantitative basis for target and diagnostic development in FY19.

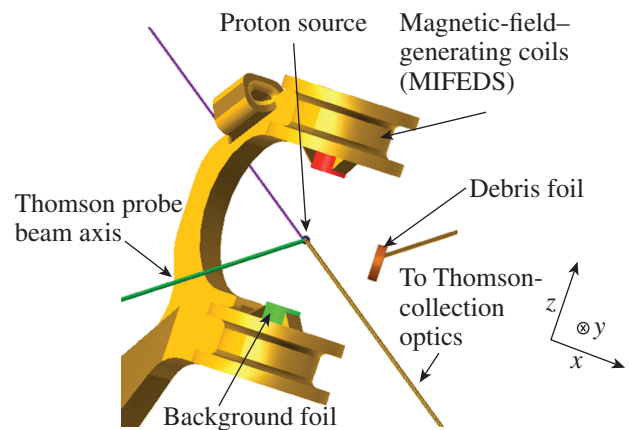
**Astrophysical Collisionless Shock Experiments with Lasers**

Principal Investigators: H.-S. Park and B. B. Pollock (LLNL)  
Co-investigators: G. Swadling and J. S. Ross (LLNL)

The goal for ACSEL-O18A is to quantify the interaction of orthogonal plasma flows with and without a background magnetic field. The field is supplied by MIFEDS, which delivers 4 to 8 T at the interaction region of the experiments (depending upon the specific geometry of the MIFEDS coils). The orthogonal plasma flows originate from two separate foil targets: one is mounted to the MIFEDS structure at one of the positions indicated by the red and green foils in Fig. 156.91;

the second foil is independently mounted outside the MIFEDS structure. The foil material compositions, spacing, and plasma arrival time to the interaction region can be varied each shot, as can be the laser drive onto each foil.

The interaction region of the two flows is simultaneously probed with 2 $\omega$  Thomson scattering and protons from the implosion of a D<sup>3</sup>He-filled capsule. To study the dynamics of these flows, the foil inside the MIFEDS is generally driven with ~500 J of laser light, while the separate foil is driven up to 8 ns later by ~2 kJ. Two types of scans attempted on these



U2289JR

Figure 156.91  
Experimental configuration viewed from the proton detector in TIM-1. One or two foils can be mounted to the MIFEDS structure, which is centered at target chamber center (TCC). The Thomson-scattering geometry is  $k$  matched to the  $z$  axis of the experiment. The proton capsule is 1 cm from TCC on the opposite side of TIM-1 and the debris foil is 2 mm from TCC.

shots include (1) varying the arrival time of the protons for given foil drive conditions to map out the temporal evolution of the interaction, and (2) holding the proton probing time fixed relative to the initial foil drive and varying the arrival time of the second plasma. Initial measurements of the electron density and temperature from Thomson scattering do not indicate a strong dependence on the strength or direction of the background magnetic field. The proton deflectometry data do show structural differences in the measured proton distribution with and without the field, but further modeling and simulations are needed in order to quantify these differences. During these experiments, the field of view of the proton-probed region is large enough to allow the entire region between the MIFEDS coils to be visible in the proton data.

### Observation of Solid Ramp-Compressed Sodium Above 300 GPa

Principal Investigator: D. N. Polsin (LLE)

Extreme pressures can induce significant changes in a material's structural and optical properties. At ambient conditions, elemental sodium can be well described by the nearly free-electron model, making it ideal for testing *ab initio* models at extreme compressions. Increasing pressure prompts a series of solid-phase transformations in Na, ultimately producing an electroneutral structure where the electrons occupy the interstitial regions or voids between the atoms.<sup>46</sup> Electrides are associated with remarkable changes in electronic behavior; Na was observed to become optically transparent at 200 GPa in diamond-anvil-cell (DAC) experiments.<sup>47</sup> In addition, the melting curve of Na decreases with increasing pressure over a wide range of pressures (over 100 GPa), dropping to below

room temperature at 118 GPa, then rising dramatically between 125 GPa and 140 GPa (Fig. 156.92).<sup>48,49</sup>

Prior to this work, no structural data existed beyond 200 GPa and no melting temperature data existed beyond 140 GPa. Nominally, our laser-driven experiments isentropically compress Na (purple curve); therefore, Na will melt in the bcc phase and, if the melting curve continues to sharply increase, a solid phase will be observed at pressures greater than 140 GPa.

To explore this high-pressure behavior, a Laboratory Basic Science (LBS) proposal was used to study ramp-compressed Na using the OMEGA EP laser. Nanosecond *in-situ* x-ray diffraction was performed to determine the crystalline structure using the powder x-ray diffraction image-plate (PXRDIP) diagnostic.<sup>50</sup> The absence of diffraction peaks was used to infer the occurrence of melting. The targets comprise Na samples (10 to 50 mm thick), sandwiched between single-crystal diamond pushers and rear windows (LiF, MgO, or diamond). Laser velocimetry was used to determine the *in-situ* pressure of the Na sample.

A solid phase of Na was repeatedly observed for pressures greater than 300 GPa (Fig. 156.93). In contrast to the highly textured diffraction pattern collected by Ma *et al.*,<sup>47</sup> a more powder-like distribution of the Na grains was observed. Indexing this structure as hP4 results in a reproducible, sixfold compressed phase of Na. For thick samples and low pressures (<200 GPa), no diffraction lines were observed, indicating that the Na melted. This and the presence of diffraction peaks above 300 GPa suggest that (1) the Na melts and then resolidifies on

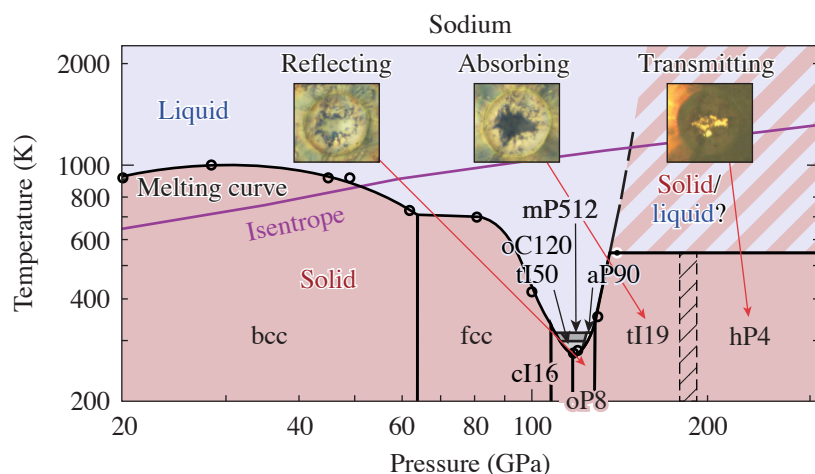
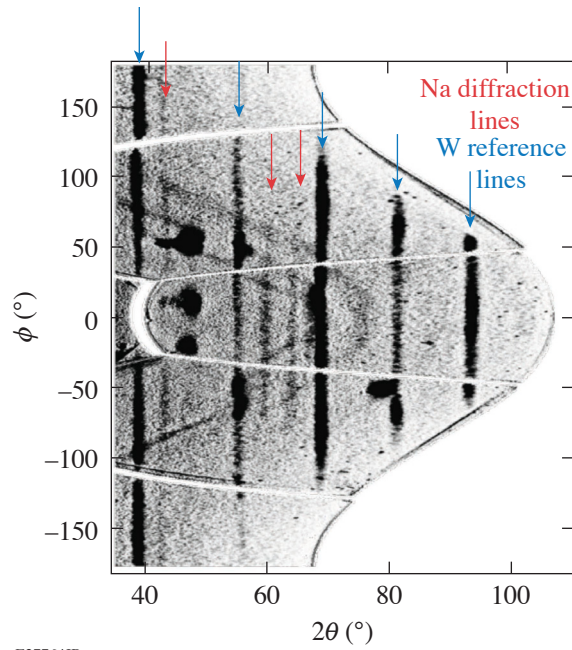


Figure 156.92  
Phase diagram of Na taken directly from Ref. 49, based on Refs. 47 and 48. The highest-pressure data for Na, before this work, are at 200 GPa from diamond-anvil-cell x-ray diffraction experiments.<sup>47</sup> The melting curve above 140 GPa is extrapolated (black dashed line), and in the striped region, the existence of solid or liquid Na is unknown.

E27765JR



E27764JR

Figure 156.93  
Background subtracted  $2\theta$ - $\phi$  projection of a Na x-ray-diffraction pattern ( $\lambda = 1.48 \text{ \AA}$ ) near 300 GPa. The red and blue arrows label Na and pinhole calibration diffraction lines, respectively.

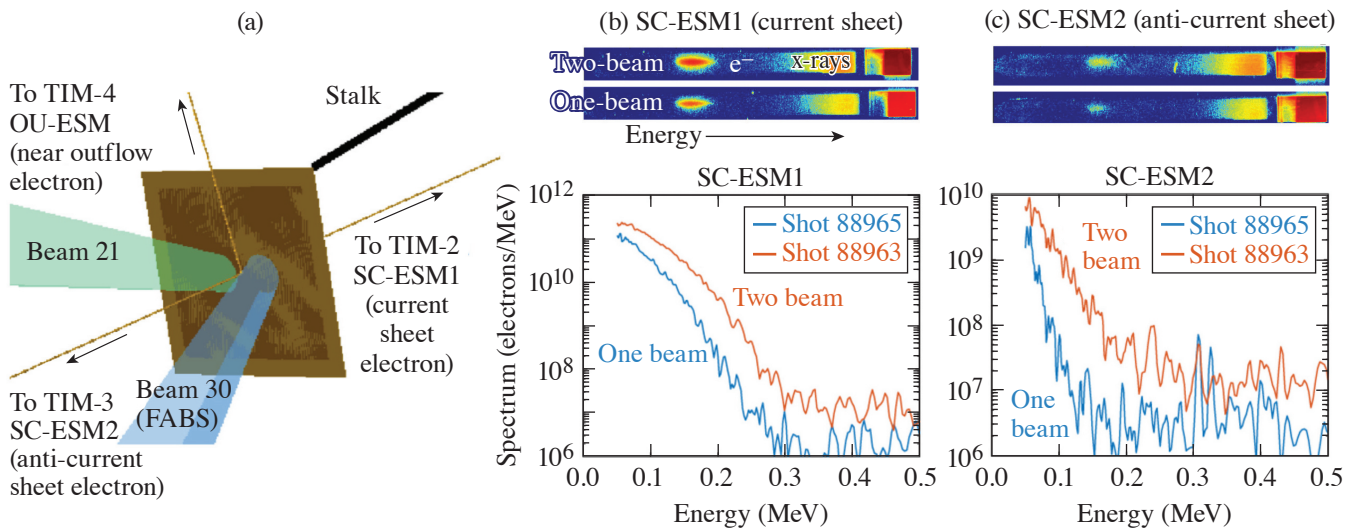
nanosecond time scales, and (2) the melting temperature greatly increases above 140 GPa. These are the highest-pressure observations of solid Na to date. In these experiments, no evidence was found that the Na became transparent at high pressure. Analysis of these results continues.

### Electron Energization During Magnetic Reconnection in High-Energy-Density Plasmas

Principal Investigator: M. J. Rosenberg (LLE)

The MagReconnection-18A shot day on OMEGA (14 March 2018) successfully demonstrated an enhancement of the supra-thermal electron population in laser-plasma experiments in which magnetic reconnection was driven. These experiments utilized a well-established platform for studying the generation, interaction, and reconnection of magnetic fields in plasmas created by the interaction of multiple laser-produced plasma plumes adjacent to each other using foil targets. The energization of particles during the annihilation of magnetic fields is a common process in astrophysical plasmas, but it is poorly understood and has rarely been investigated in the laboratory. In prior-year experiments, electron spectra were obtained at energies of  $\sim 50$  to 300 keV, but a negligible difference was observed in experiments with versus without magnetic reconnection, likely as a consequence of laser-plasma instabilities (LPI's).

These experiments used a truncated laser pulse, reduced laser energy, and/or a different target material for the planar foil (Al in addition to CH) in order to greatly reduce LPI signatures. The experimental setup and data, obtained using a  $5\text{-}\mu\text{m}$  Al foil driven by one or two 200-J, 0.5-ns laser pulses, are shown in Fig. 156.94. These drive parameters produced minimal signal in the LPI diagnostics. The two-beam experiment drove the reconnection of self-generated magnetic fields from the collision of expanding plasma plumes, while the one-beam



U2375JR

Figure 156.94  
(a) Experimental setup and [(b),(c)] data obtained on the electron spectrum using a  $5\text{-}\mu\text{m}$  Al foil driven by one or two 200-J, 0.5-ns laser pulses.

experiment did not. Energetic electrons were observed in both the forward-going direction [Fig. 156.94(b)], corresponding to acceleration by reconnection electric fields, and the direction opposite to that [Fig. 156.94(c)]. The two-beam experiment produced an enhancement of more than a factor of 2 above the one-beam experiment, suggesting that the plasma collision and magnetic-field reconnection play a role in electron energization. In addition, Thomson-scattering measurements were obtained to characterize plasma conditions in the reconnection region, and the first monoenergetic proton radiography images of magnetic fields in an Al plasma were obtained.

#### **Atomic and Electronic Structure of Warm Dense Silicon**

Principal Investigator: J. R. Rygg (LLE)

Warm dense matter, characterized by solid or higher density and temperatures of a few up to tens of electron volts, is challenging to model and experimentally difficult to produce and measure. Theoretical descriptions typically have their roots in plasma or condensed-matter limits, which start to break down at elevated densities and moderate temperature (for plasma theory) or elevated temperatures (for condensed matter theory). Experimental measurements are often limited to only a few parameters at a time and rely on computer simulations or model fitting to fill in the details.

The LBS Program's SiStructuresEP-18A Campaign had one day on OMEGA EP to initiate development of a platform

to produce a precise and uniform state of warm dense matter by shock compression and to simultaneously determine its properties using the velocity interferometer system for any reflector (VISAR) (for pressure),<sup>51</sup> angularly resolved x-ray diffraction with PXRDIP (for atomic structure and density),<sup>52</sup> and spectrally resolved inelastic x-ray scattering with XRTS (for ionization state).<sup>53,54</sup> We will leverage the complementary diagnostics in their respective analyses; for example, by directly using the ion correlation measured by PXRDIP in the analysis of the inelastic spectrum, rather than as a fit parameter.

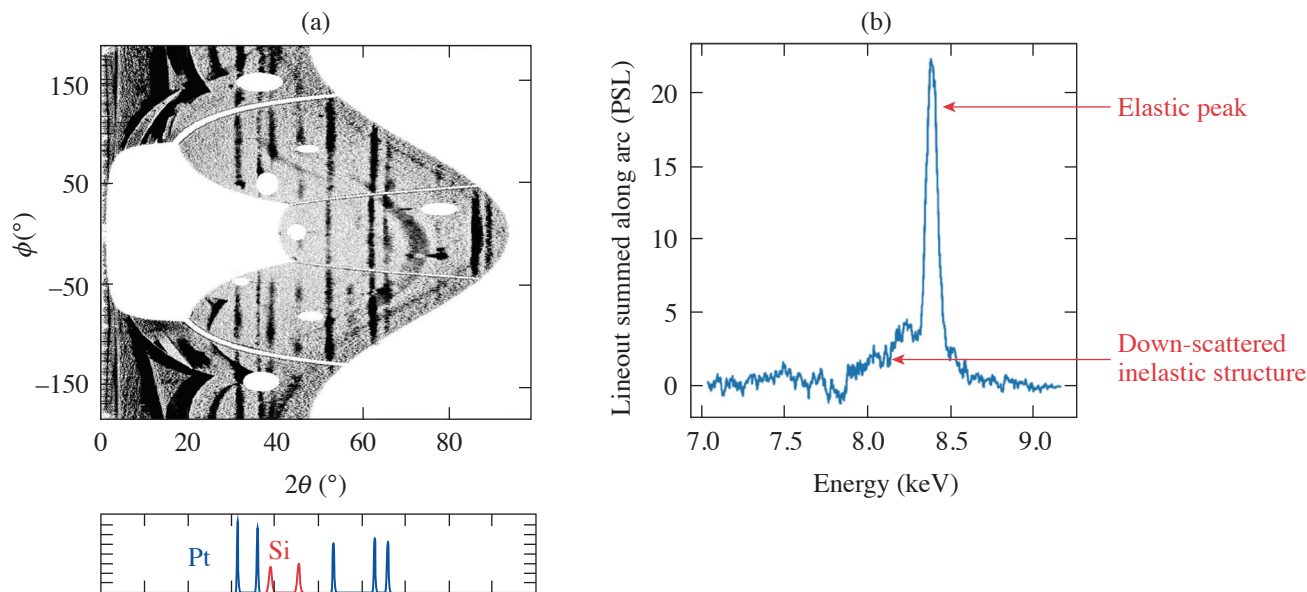
Results from this first day were used to overcome signal to background issues with the experimental setup, and measurements have been obtained on silicon samples on separate shots (see Fig. 156.95). The goals for a follow-up campaign, scheduled for FY19, include demonstration of simultaneous PXRDIP and XRTS measurements.

#### **Measurement of the High-Pressure Thermal Conductivity of Iron and Titanium**

Principal Investigator: R. F. Smith (LLNL)

Co-investigators: J. Wicks and C. Krill (Johns Hopkins University)

High-pressure thermal conductivity is one of the most important and yet most difficult to measure physical properties of materials. Within the Earth's interior, the thermal conductivity  $k$  of Fe and Fe-rich alloys at core pressure–temperature



E27654aJR

Figure 156.95

(a) Angularly resolved and (b) spectrally resolved x-ray scattering from warm dense silicon above 1 Mbar.

conditions (135 to 360 GPa, 2500 to 5000 K) is a key parameter for heat transport models and plays an important role in determining the temperature profile and energy balance of our planet. The thermal conductivity of the Earth's core remains poorly constrained because of the extreme difficulty in making thermal transport measurements under the relevant pressure and temperature conditions. Two experimental studies published in *Nature*<sup>55,56</sup> report values of  $k$  for Fe, which vary by a factor of 7 at  $\sim 130$  GPa ( $34 \rightarrow 225 \text{ W m}^{-1} \text{ K}^{-1}$ ). The goal of these experiments is to constrain the thermal conductivity at high pressures, using a ramp-compression platform previously developed on OMEGA<sup>57</sup> [Fig. 156.96(a)]. Here, 15 beams deliver 200 to 300 J over 2 ns into a hohlraum. This results in a shock wave that propagates through the Be/12% Br-CH layer. After shock breakout, the ionized CH unloads across a vacuum gap as it piles up against the stepped Fe layer. This results in a mechanical pressure wave and a thermal wave running longitudinally through the sample. The ASBO/SOP (streaked optical pyrometer) diagnostic provides velocity and thermal transport information through the stepped-samples [Figs. 156.96(b) and 156.96(c)]. Analysis is underway to translate this data into a measurement of thermal conductivity.

### *X-Ray Radiography of Shocks Perturbed by Hot Electrons*

Principal Investigators: W. Theobald (LLE) and A. Casner (CEA)

In the shock-ignition scheme for ICF, an intense spike is used to drive a strong converging shock at the end of the compression phase. This spike is intense enough to generate supra-thermal electrons through laser-plasma instabilities (stimulated Raman scattering, two-plasmon decay, etc.). Understanding the distribution of these electrons (temperature, energy, etc.) and their effect on the hydrodynamics of shock is a critical step for shock ignition. The description of hot-electron production and propagation has been recently added to radiation-hydrodynamic codes, and dedicated experiments are needed to validate it.

In ShRadEp-18A, we conduct an experiment to study the population of hot electrons produced in an interaction regime close to shock ignition and their effect on shocks. Figure 156.97 presents a schematic of the experimental setup. The interaction target is a 500- $\mu\text{m}$ -diam CH cylinder with an embedded 20- $\mu\text{m}$  Cu layer. The distance between the Cu layer and the front of the CH, facing the laser, is 175  $\mu\text{m}$ . The laser irradiating the interaction target is one OMEGA EP beam with a 1-ns square pulse (1250 J) and without distributed phase plates (DPP's) ( $\sim 150$ - $\mu\text{m}$  focal spot FWHM), resulting in a peak intensity  $\sim 10^{16} \text{ W/cm}^2$ .

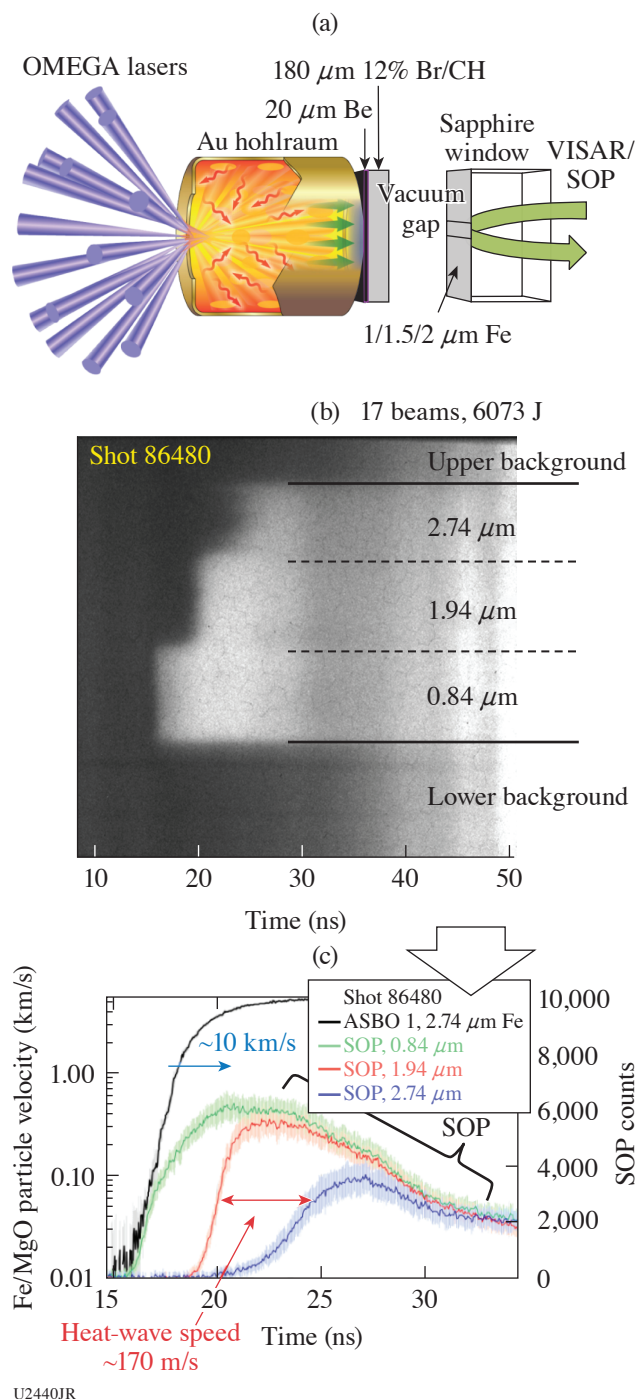
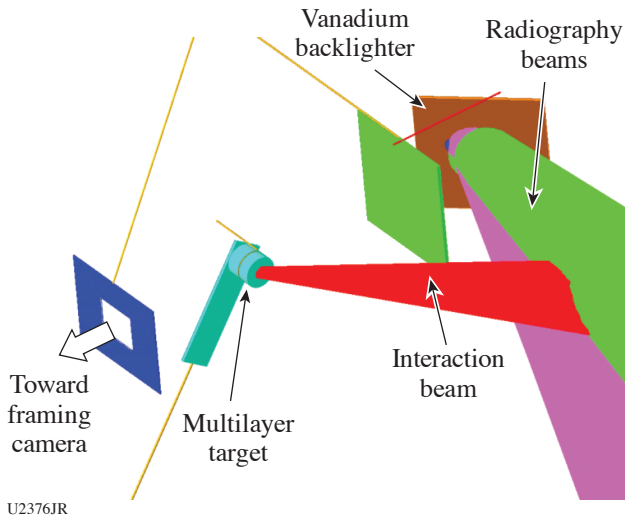


Figure 156.96 (a) Target design to measure heat flow in a ramp-compressed, stepped-Fe sample. (b) Raw SOP data show the heat flow through multiple Fe thicknesses. (c) Extracted velocity and temperature (SOP counts), both versus time, for different step thicknesses.

At this intensity, scaling laws from previous experiments and PIC simulations predict a dominance of stimulated Raman scattering (SRS) hot electrons with a temperature of 40 keV



U2376JR

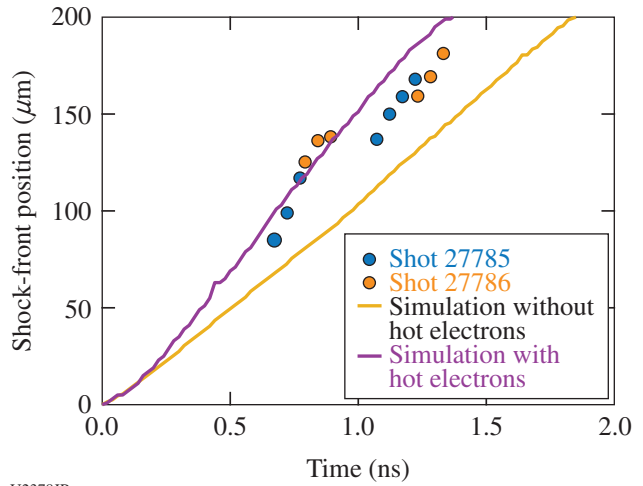
Figure 156.97

VisRad view of the experiment. One OMEGA EP interaction beam irradiates the multilayer target with a small focal spot. Three other beams irradiate the vanadium backlighter for the side radiography of the target image on a framing camera.

and a conversion efficiency of 10%. Multiple diagnostics have been set up to characterize the hot-electron population in this experiment. BMXS and HXRD measure the bremsstrahlung radiation produced by these electrons. The zinc von Hamos (ZnVH) and high-resolution spectrometers (HRS's) measure the  $K_{\alpha}$  emission from the embedded copper layer. The three other OMEGA EP beams were used to irradiate a vanadium foil to produce a high flux of x-ray radiation for the side radiography of the cylinder. These radiography beams were 3-ns square pulses (2400 J) with a 400- $\mu\text{m}$  focal spot (with DPP). The target was imaged with a pinhole array into a framing camera, resulting in 16 two-dimensional images of the shock propagation. However, because of the high sensitivity on the

target alignment compared to the imaging pinhole, only four images per shot are relevant (one per strip).

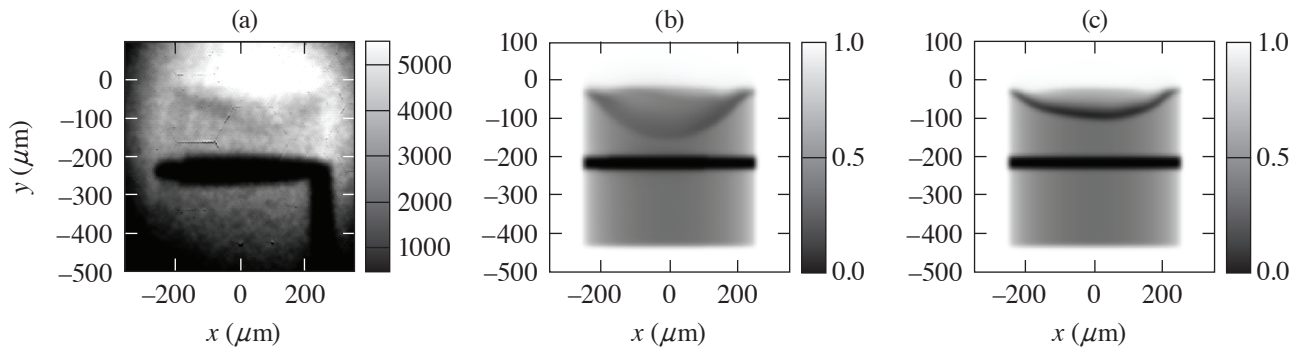
Figure 156.98 presents the qualitative comparison of the two synthetic radiographies obtained from a *CHIC* simulation with or without hot electrons with an experimental radiography from shot 27785. All images were taken 1 ns after the beginning of the laser-matter interaction. The simulation takes into account that the hot electrons are in much better agreement with the experimental image, both for the shock position and the shock-front contrast (which is characteristic of the expansion of the shock CH under the heating of hot electrons). Figure 156.99 compares the experimental shock-front position (from the radiographies of shots 27785 and 27786) with the simulated one (from the simulation with and without hot electrons). The



U2378JR

Figure 156.99

Shock-front position measured on the radiographies of shots 27785 and 27786 compared to the simulations with or without hot electrons.



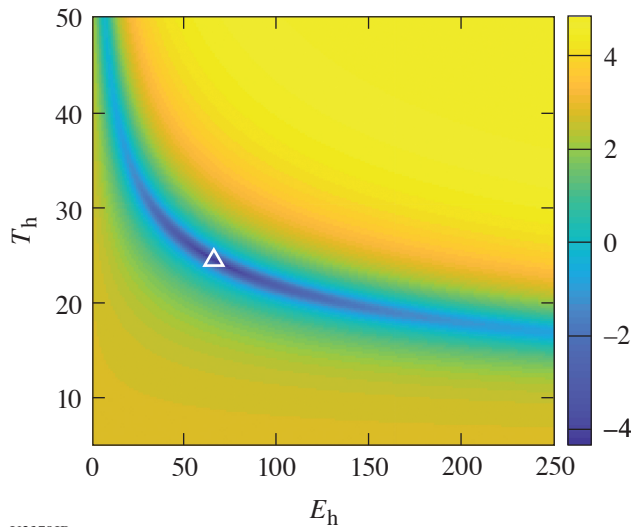
U2377JR

Figure 156.98

(a) Comparison of synthetic radiography from post-processed *CHIC* simulations at 1 ns and an experimental radiography at 1 ns from shot 27785. The synthetic radiography from the simulation taking in account (b) the hot electron is in much better agreement than (c) the one from the simulation without hot electrons.

experimental data are in better agreement with the simulation, taking into account the hot electrons, yet the shock velocity at a later time, after 1 ns, is less than expected. The reason for this could be because the hot-electron temperature or conversion efficiency is lower than expected from the scaling laws.

It is challenging to measure these parameters using the BMXS data because of the large amount of signals on image plates (IP's) 1 to 4 because of the backlighter and the absence of signals on IP's 8 to 15. Figure 156.100 presents a  $\chi^2$  analysis of a BMXS signal from IP's 5 to 7 for shot 27785. This analysis used *Geant4* simulations of the BMXS IP stack and the target bremsstrahlung emission, separately. Also, one Maxwellian temperature distribution for the hot electrons was assumed. A temperature of 25 keV and a conversion efficiency of 5% were found, which are lower than initially expected. This measurement must be confirmed with the  $K_\alpha$  diagnostics and HXR. If so, new hydrodynamic simulations must be realized with these hot-electron parameters to see if they are in better agreement with the experimental data.



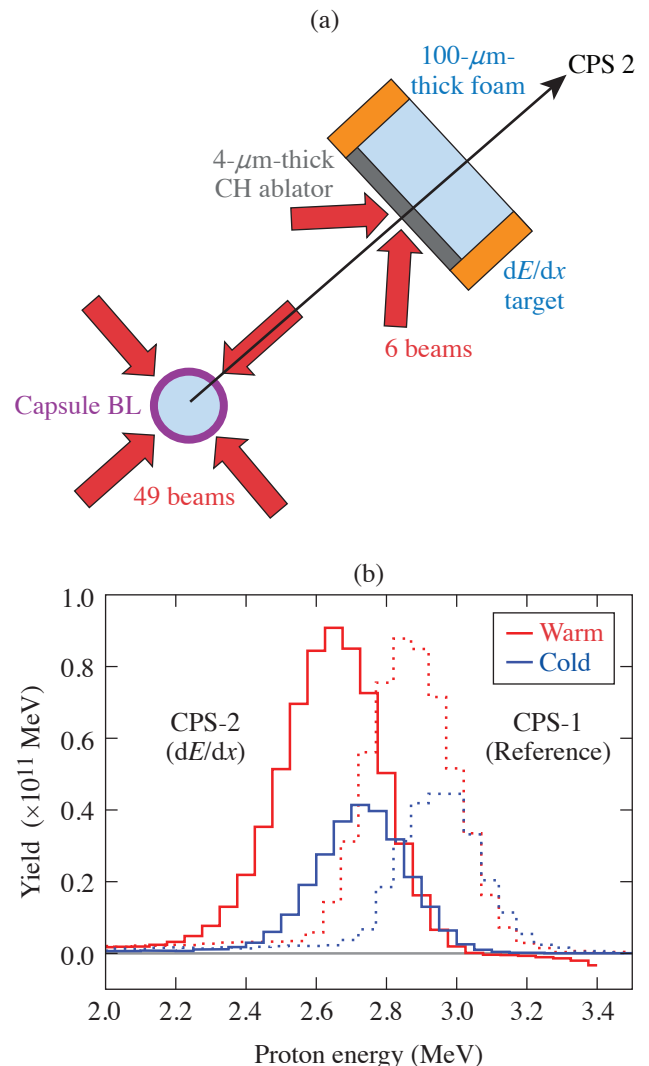
U2379JR  
Figure 156.100  
 $\chi^2$  analysis of IP's 5 to 7 of BMXS for shot 27785. The minimum gives a measured hot-electron temperature of 25 keV and total energy of 65 J (5% conversion efficiency).

**Charged-Particle Stopping Power Near the Bragg Peak**

Principal Investigator: A. B. Zylstra (LANL)

Charged-particle stopping power, or  $dE/dx$ , is a fundamental transport property, the study of which illuminates basic HEDP physics and is directly relevant to alpha self-heating in inertial fusion. Recent experiments have measured  $dE/dx$  in HED plas-

mas for the first time, but they were studying either very fast projectile particles in relatively cold plasmas<sup>58</sup> or ICF-relevant stopping power near the “Bragg” peak but with large uncertainties in the underlying plasma conditions.<sup>59</sup> The “dEdx” Campaign has been developing a platform to measure stopping power near the Bragg peak in well-characterized plasmas. The concept is shown in Fig. 156.101(a). Six OMEGA beams drive a plastic ablator, launching a planar shock into a 100- $\mu\text{m}$ -thick sample of foam. The shocked-foam plasma is probed by fusion products from a  $D^3\text{He}$  capsule backlighter and measured with the CPS-2 dipole magnetic spectrometer. This configuration is predicted to produce data that can distinguish stopping-power models in regimes relevant to ICF. In FY17 some data were



U2380JR  
Figure 156.101  
(a) Schematic of the experimental geometry for the  $dE/dx$  platform. (b) Example DD proton data from 2017. BL: backlighter.

collected using DD protons [Fig. 156.101(b)], but measurements of the  $D^3He$  alphas are required to constrain models since the proton stopping is relatively insensitive.

In FY18 two shot days were conducted. The first, dEdxEP-18A (5 December 2017), was conducted using OMEGA EP in the long-pulse configuration to develop the physics package. Several foam densities and laser-drive intensities were studied, and the plasma conditions were characterized by measuring the shock propagation and breakout using ASBO. The results of this experiment were used to choose the physics package conditions for a second shot day on OMEGA later in the year, dEdx-18A (20 September 2018). This shot day was executed successfully and data analysis is in progress.

### FY18 LLNL Experimental Programs at Omega

Principal Investigators: R. F. Heeter, S. J. Ali, L. R. Benedetti, J. V. Bernier, H. Chen, F. Coppari, A. Fernandez Panella, C. M. Huntington, S. Jiang, G. E. Kemp, S. F. Khan, A. Krygier, A. E. Lazicki, N. Lemos, M. J. MacDonald, D. Mariscal, E. V. Marley, M. C. Marshall (formerly M. C. Gregor), D. A. Martinez, J. M. McNaney, M. A. Millot, Y. Ping, B. B. Pollock, P. L. Poole, H. G. Rinderknecht (now at LLE), A. M. Saunders, R. F. Smith, G. F. Swadling, R. Tommasini, K. Widmann, G. J. Williams, O. L. Landen, W. W. Hsing, and A. S. Wan (LLNL); L. Elgin and C. Kuranz (University of Michigan); E. Gumbrell and M. Rubery [Atomic Weapons Establishment (AWE)]; and R. Hua (UCSD)

In FY18, Lawrence Livermore National Laboratory's (LLNL's) High-Energy-Density (HED) Physics and Indirect-Drive Inertial Confinement Fusion (ICF-ID) Programs conducted numerous campaigns on the OMEGA and OMEGA EP Laser Systems. This was the 20th year of National Lab collaborative experiments at Omega since the Nova Laser at LLNL shut down in 1999 (Ref. 60), building upon prior collaborations. In FY18 overall, these LLNL programs led 465 target shots, with 283 shots using only the OMEGA laser, 172 shots using only the OMEGA EP laser, and 10 joint shots using both lasers together. Approximately 28% of the total number of shots (60 OMEGA shots and 71 OMEGA EP shots) supported the ICF-ID Campaign. The remaining 72% (223 OMEGA-only shots, 101 OMEGA EP-only shots, and 10 joint shots) were dedicated to experiments for HED physics. Highlights of the various HED and ICF-ID Campaigns are summarized in the following reports.

In addition to these experiments, LLNL Principal Investigators (PI's) led a variety of Laboratory Basic Science campaigns using OMEGA and OMEGA EP, including 99 target shots using only OMEGA and 39 shots using only OMEGA EP.

Overall, LLNL PI's led a total of 603 shots at LLE in FY18. In addition, LLNL PI's supported 47 NLUF shots on OMEGA and 31 NLUF shots on OMEGA EP in collaboration with the academic community.

This work performed under the auspices of the U.S. Department of Energy by Lawrence Livermore National Laboratory under Contract DE-AC52-07NA27344.

### Indirect-Drive Inertial Confinement Fusion Experiments

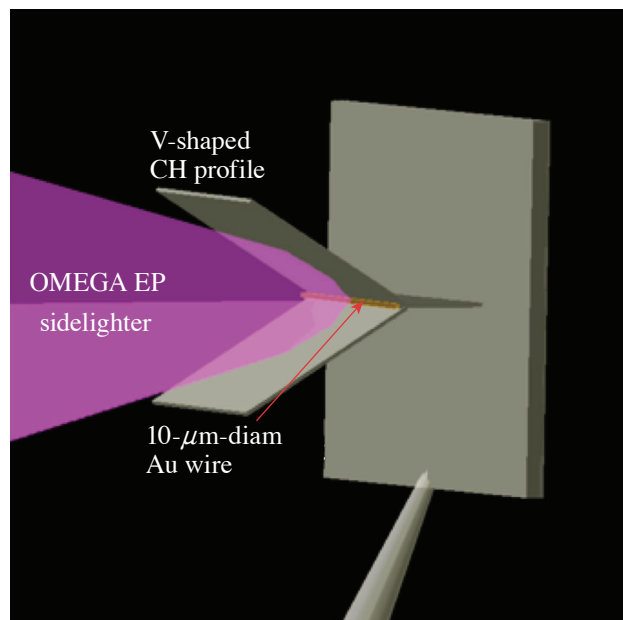
#### Short-Pulse Backlighters Using In-Situ Plasma Reflectors

Principal Investigator: R. Tommasini

Co-investigators: J. Park, L. Divol, and A. Kemp

The SmallSpotBL-EP Campaign was designed to test novel small-source x-ray backlighters. The design uses *in-situ* plasma mirrors to enhance the laser energy coupling on the backlighter target and thereby increase the conversion efficiency into x rays and, at the same time, mitigate the issue of pointing the laser spot onto backlighters small enough to act as point sources.

The targets, shown in Fig. 156.102, consisted of 10- $\mu\text{m}$ -diam gold wires placed at the vertex of a V-shaped profile formed by two CH foils. The angle between the two foils was chosen to be 40° or 60°. The OMEGA EP sidelighter beam delivered 30-ps, 1-kJ pulses into the vertex. The x-ray yield and source



U2381JR

Figure 156.102  
Experimental configuration for OMEGA EP shot 79708.

size were measured, along the line of sight parallel with the gold wire, by radiographing a tantalum step wedge and a calibrated 200- $\mu\text{m}$ -diam tungsten sphere.

Shots with and without the V-shaped profile were performed and compared. The results have fully proved the concept: x-ray conversion efficiency increased  $\sim 3\times$  using the plasma mirror configuration as compared to bare wires, with great reproducibility and also a 25% reduction in source size. The results have validated a similar experiment performed earlier on NIF-ARC (National Ignition Facility-Advanced Radiographic Capability). An improved version of these backlighters, employing parabolic-like shaped profiles, has been designed and will be tested in the upcoming experiments on OMEGA EP.

These novel schemes open the way to the next generation of backlighters to be used for hard x-ray radiography of the dense cores in ICF implosions and will allow the reduction of the backlighter size in order to record radiographs with sufficient signal to noise and higher spatial resolution.

#### **Diamond Sound-Speed Measurements Between 8 and 14 Mbar**

Principal Investigator: A. Fernandez-Panella

Co-investigators: D. E. Fratanduono and P. M. Celliers

This half day at OMEGA was designed to constrain equation-of-state (EOS) models by collecting high-quality data on

the sound speed of diamond in the multi-Mbar range. The FY18 shots completed the data set from the previous FY17 campaign where four data points were acquired up to 13 Mbar.

The campaign used planar targets and a direct-drive configuration with a CH or Be ablator, a quartz pusher and two targets side by side: quartz (standard) and diamond. The velocity profiles at the free surface were recorded using VISAR as the primary diagnostic (Fig. 156.103). The laser drive energy was varied to probe different shocked pressure states in diamond. The laser pulse was designed to produce a small pressure perturbation that propagated through both the standard and the sample. The wave propagation analysis described in Ref. 61 was then applied to extract the sound speed of both materials, quartz and diamond, from their velocity profiles (Fig. 156.104).

This campaign produced seven good data points from 700 to 1800 GPa. The data analysis is still in progress. The positions in pressure of the data acquired in the FY18 campaign are signaled by blue circles in Fig. 156.104, where solid and open circles represent data obtained by using CH and Be ablators, respectively. The results from the previous FY17 shots were useful for optimizing the target design, VISAR etalon choice, etc., and they indicate that sound-speed measurements are sensitive enough to constrain EOS models. The Livermore LEOS table 9061 shows good agreement with the data. The full analysis of the campaign data set should be able to constrain the EOS models in a wide pressure range up to 20 Mbar.

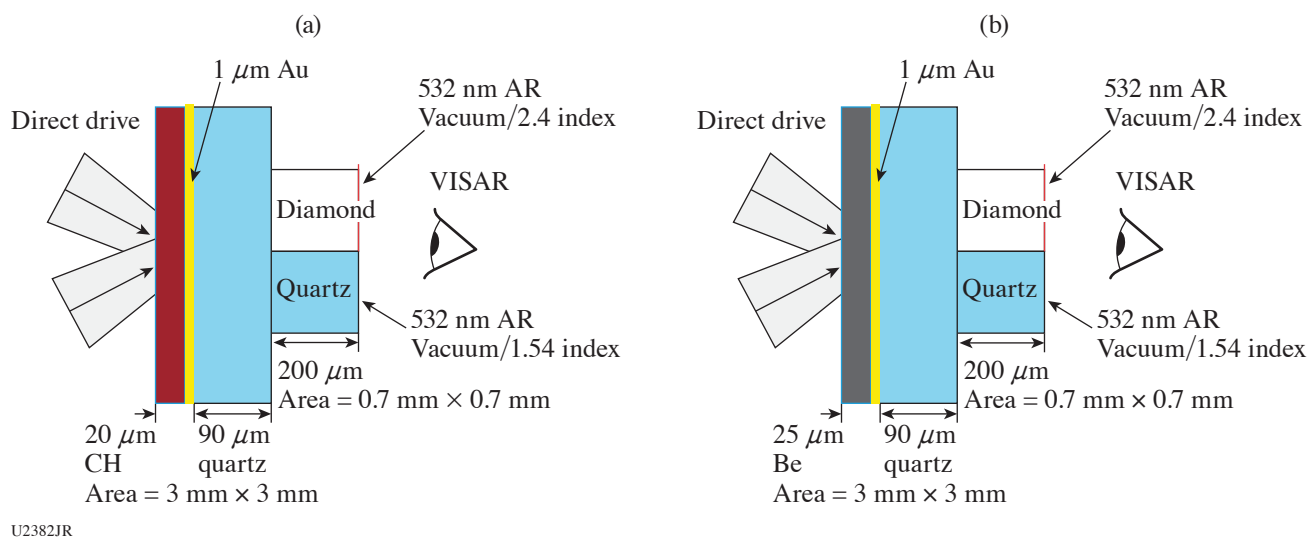
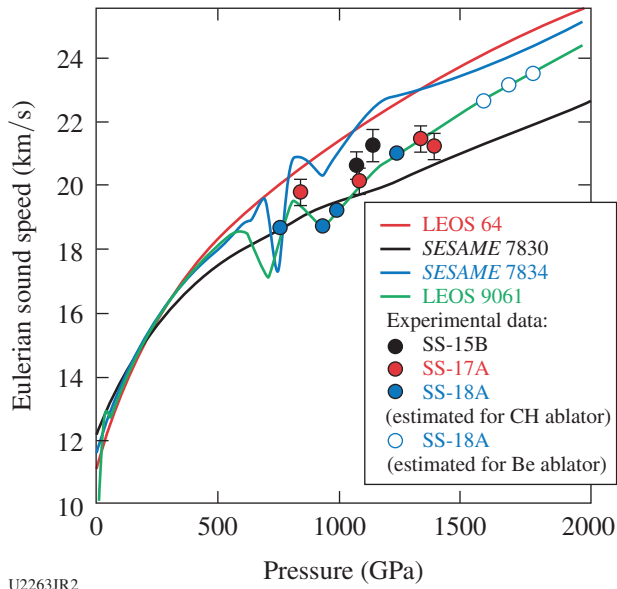


Figure 156.103  
Experimental setup and target designs: (a) CH and (b) Be ablators for the DiamondSS-18A Campaign.



U2263JR2

Figure 156.104  
Diamond sound speed versus pressure.

**Thomson-Scattering Measurements from Gold- and Beryllium-Coated Spheres**

Principal Investigator: G. F. Swadling  
Co-investigators: J. S. Ross, M. Rosen, K. Widmann and J. Moody

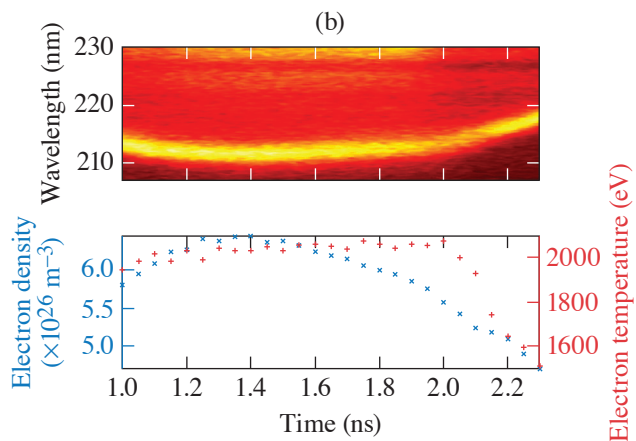
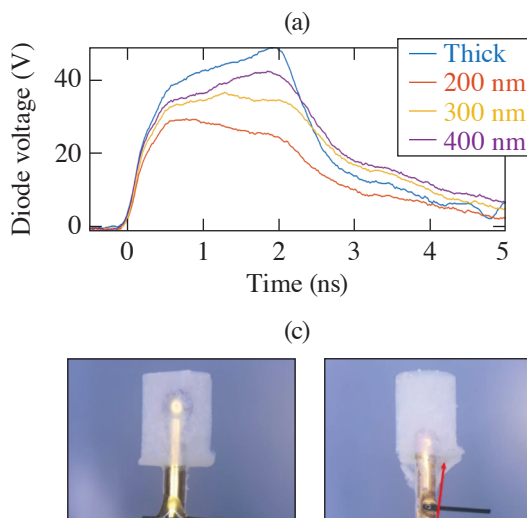
The AuSphereInFoam Campaign sought to collect data using the foam-covered sphere platform developed for the

FoamCoSphere day in FY17. Additional aims were to carry out burnthrough measurements using thin-wall (100- to 400-nm) gold sphere targets and measurements of Be-coated targets to provide benchmarking data for radiation-hydrodynamic models in a regime less dominated by complex atomic physics of gold.

On this platform, spherical targets are symmetrically heated using the 60 OMEGA beams in spherical geometry to investigate atomic physics models, radiative properties of the laser-spot plasma, and the interpenetration of multi-ion species plasmas relevant to ICF indirect-drive-ignition hohlraums. These experiments use a laser irradiation of  $10^{14}$  to  $10^{15}$  W/cm<sup>2</sup>, similar to the intensities found in ICF hohlraums fielded on the NIF.

The thin-wall target experiments used 0.86-mm-diam spheres with variable coating thicknesses. The spheres were heated using either 1- or 2-ns laser pulses. The plasma temperature and density were measured at various radial positions in the blowoff plasma using Thomson scattering (TS), while x-ray flux from the gold sphere was recorded using the Dante soft x-ray spectrometer. These shots were very successful: the data appear to be highly reproducible and the trends are consistent with pre-shot modeling [Fig. 156.105(a)]. The data captured in these experiments are currently being used to benchmark transport models.

The Be Sphere shots also produced high-quality TS data, which has been fit using theoretical curves to produce accurate



U2384JR

Figure 156.105  
(a) Dante trace showing changes in soft x-ray emission with gold thickness for a 2-ns heater pulse. (b) Thomson-scattering data fit to extract  $T_e$ ,  $n_e$  versus time for a Be-coated target. (c) Examples of two foam-covered targets, showing variation in centering, shape, and size.

measurements of blowoff plasma density and temperature [Fig. 156.105(b)]. A shot day in FY19 is planned to further benchmark nonlocal transport models.

Finally, in the foam-covered sphere experiments, the Au sphere was embedded in a low-density ( $3.8\text{-mg/cm}^3$ ) CH foam. Inconsistencies in the centration of the sphere with respect to the foam, combined with irregularities in the foam shape and suspected density clumping within the foam [Fig. 156.105(c)], led to data that were not reproducible shot-to-shot. The technical issues with foam fabrication are related to its very low density and the absence of a surrounding support structure in these open-geometry targets. Additional target-fabrication improvements are required before this type of target can be fielded for detailed scientific studies.

### ***Hydrodynamic Response from Nonuniformities in High-Density Carbon, Plastic, and Beryllium Ablators***

Principal Investigator: S. Ali

Co-investigators: P. M. Celliers, S. W. Haan, S. Baxamusa, H. Reynolds, M. Johnson, H. Xu, N. Alexander, H. Huang, V. A. Smalyuk, and H. Robey

Performance and yield from fusion capsules on the NIF are highly dependent on the uniformity of the capsule implosion, and hydrodynamic instabilities are a significant source of performance degradation during the implosion. These can arise due to, among other reasons, intrinsic heterogeneity within the capsule material. Beryllium and high-density carbon (HDC) have complex microstructures, and both are acoustically anisotropic, which can lead to variations in the shock speed in crystallites of different orientations, potentially seeding instabilities. Additional sources of heterogeneous response include behavior of the grain boundary material, which is often of a different bonding character than the crystallites, voids in the deposited material, and static internal stresses in the polycrystalline structure. The current strategy for reducing the impact of internal heterogeneities is to fully melt the ablator material on the first shock, requiring 2.6 Mbar for beryllium and  $>12$  Mbar for HDC.<sup>62–65</sup> In the case of HDC, this strong shock also raises the entropy of the fuel, making it more difficult to reach the high densities required for ignition. As part of the effort to understand both the origin and impact of the velocity nonuniformities in all three ablators, this campaign conducted 2-D velocimetry experiments on planar foils of the three ablator materials under conditions near the first shock and second shock levels in beryllium and glow-discharge polymer (GDP), and up to the first shock level in HDC.

The goal of the Capseed Campaign is to measure shock-front velocity nonuniformities in ICF ablator materials and quantify the level of nonuniformity caused by intrinsic effects. This is done using the OMEGA high-resolution velocimeter (OHRV) to obtain velocity maps of the optically reflecting shock front following release of the ablator material into either PMMA for the warm experiments or cryogenic deuterium for the cryo experiments.

Three Capseed Campaigns were conducted in FY18: CapseedHDC, Capseed2ShockCryo, and CapseedShellCryo. The goal of CapseedHDC was to obtain a pressure scan of velocity nonuniformity over the HDC melt region, 7 to 12 Mbar, helping constrain the first shock level required for a uniform shock response. The warm component of CapseedHDC also included measurements of the fill-tube perturbation from 5-, 10-, and 30- $\mu\text{m}$ -diam fill tubes, with perturbation sizes comparing qualitatively well with simulations. Capseed2ShockCryo was used to investigate velocity nonuniformity growth on transit of a second shock through GDP and Be. While relatively little nonuniformity increase was seen in the GDP, the rms for second shock Be increased by a factor of 3. CapseedShellCryo was an initial attempt to move toward more capsule-like targets, as opposed to the planar foils previously used for Capseed Campaigns, by using segments from large-diameter (4.5- to 5-mm) capsules, beginning with a successful experiment on 5-mm-diam GDP hemispheres on the first half-day. Unfortunately, due to fabrication delays, the 5-mm HDC spheres were not complete in time for the second half-day, but a secondary goal of measuring the effect of grain size on the nonuniformity was achieved. A significant improvement was seen in the velocity rms for the nanocrystalline versus microcrystalline samples, as shown in Fig. 156.106. These experiments are continuing into FY19, with two half-days of further cryogenic measurements planned.

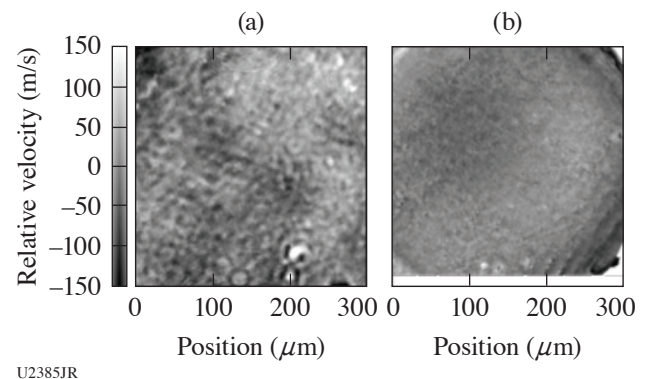


Figure 156.106 Velocity maps from (a) microcrystalline and (b) nanocrystalline HDC releasing into  $\text{D}_2$  at 12 Mbar. The rms velocity roughness was 35 m/s for (a) and 11 m/s for (b), with diagnostic detection limits of 10 m/s for (a) and 5 m/s for (b).

**Near-Critical-Density X-Ray and Particle Sources**

Principal Investigator: N. Lemos  
 Co-investigators: A. Pak, A. Kemp, G. J. Williams,  
 D. Mariscal, O. L. Landen, and T. Ma

A series of shots was designed to understand how to increase the x-ray/proton yield using near-critical-density targets at ARC<sup>66</sup>-relevant pulse durations/intensities. These shots maximized the ion and x-ray emission by optimizing the scale length of the pre-plasma in front of the solid target.

Results obtained on OMEGA EP<sup>67,68</sup> and recent results from LFEX (Laser for Fast Ignition Experiments) at Osaka University<sup>69</sup> have shown that by extending the laser pulse duration to several picoseconds, the maximum proton energy produced by the target normal sheath acceleration (TNSA) mechanism more than doubled. This enhanced energy and efficiency exceed the theoretical prediction given by the standard TNSA theory and particle-in-cell (PIC) simulations. These experiments show that a superponderomotive electron distribution generated by the picosecond-scale laser pulses drives an increase to the maximum sheath potential.

The present experiment combined the advantages of the long-pulse duration to enhance the TNSA fields and increased laser absorption with a pre-plasma in front of the target. A controlled pre-plasma was produced by focusing a 10-J, 10-ns UV laser pulse onto a parylene-coated, 13- $\mu\text{m}$  silver foil prior to the arrival of the high-intensity ARC-like beam (Fig. 156.107). The short-pulse beam was delayed 1 to 8 ns relative to the UV beam.

Figure 156.108(a) shows the maximum proton energy (22 MeV) was achieved with a 2-ns delay between the two

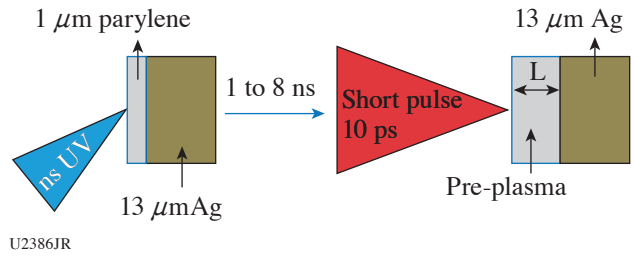


Figure 156.107  
 Experimental setup.

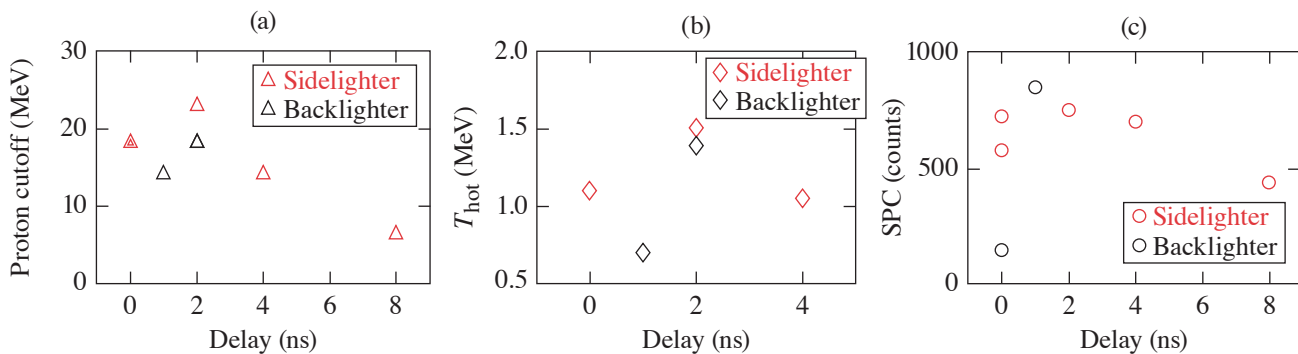
pulses; increasing the delay further degraded the performance. Figure 156.108(b) shows the escaped electron temperature is also maximized at a delay of 2 ns and corroborates the result shown in Fig. 156.108(a). Figure 156.108(c) also shows the maximum x-ray yield at a delay of 1 to 2 ns, indicating this delay is where the laser is better coupled into the solid target.

Results of this campaign are being used to optimize a similar platform that is being developed at NIF-ARC.

**Optimization Study of Thin-Foil Backlighters for Use on NIF-ARC**

Principal Investigator: G. J. Williams  
 Co-investigators: H. Chen, A. Kemp, N. Candeias Lemos,  
 T. Ma, D. Mariscal, and O. L. Landen

This series of shots was designed to benchmark backlighter conversion efficiency for NIF-ARC conditions<sup>70</sup> for various pulse durations and intensities, with 1-D x-ray source size measurements for side-on radiography applications. Electron temperatures and  $K_{\alpha}$  line emissions were measured across a laser and target parameter scan.



U2387JR

Figure 156.108  
 (a) Maximum proton energy, (b) electron temperature, and (c) x-ray yield versus delay between the long and short pulse.

Recent simulation and experimental work have shown that, for a given power or intensity, the electron temperature continues to increase with pulse duration up to a saturation limit dependent on the spot size.<sup>69,71,72</sup> Underdense plasma will one-dimensionally expand from the target front surface until the scale length exceeds the spot size. At ARC-like conditions, the large spot size is invoked to explain the observed relativistic electrons despite an intensity of  $10^{18}$  W/cm<sup>2</sup> (Ref. 73). The electron temperature is fundamental to optimizing high-energy x-ray backlighters.

Interleaved short-pulse shots were performed on OMEGA EP using 5- and 15- $\mu$ m gold foil targets with a 1- $\mu$ m CH tamper layer. In the Beam 1 (sidelighter) configuration, a gold sphere is used to project a shadow of the x-ray source perpendicular to the foil, as shown in Fig. 156.109(a), with a near-constant energy on target at pulse durations of 3, 10, and 30 ps. The Beam 2 (backlighter) shots used a fixed intensity of  $10^{18}$  W/cm<sup>2</sup> by changing both energy and pulse duration together [see Fig. 156.109(b)].

Measurements of x rays and electrons were recorded for all shots. In line with expectations, the data show an increase and then saturation of the electron temperature with pulse duration for a fixed intensity [Fig. 156.110(a)]. A correlation to existing scaling for underdense electron acceleration<sup>74</sup> was observed by scanning over a range of laser powers (intensities), where the Pukhov scaling<sup>75</sup> of  $kT \sim \sqrt{I/I_{18}}$  is shown with electron data in Fig. 156.110(b). The Au K $\alpha$  x-ray yield scaled linearly with pulse duration for a given target but did not correlate with

intensity [Fig. 156.110(c)]. X-ray source size measurements are ongoing; data suggest x rays >20 keV have a source 1.5 to 2.5 $\times$  that of the foil thickness. This measurement could be influenced by the plasma blowoff and the softer filtering used. The results of this campaign will be used to optimize the performance of future NIF-ARC x-ray backlighter platforms.

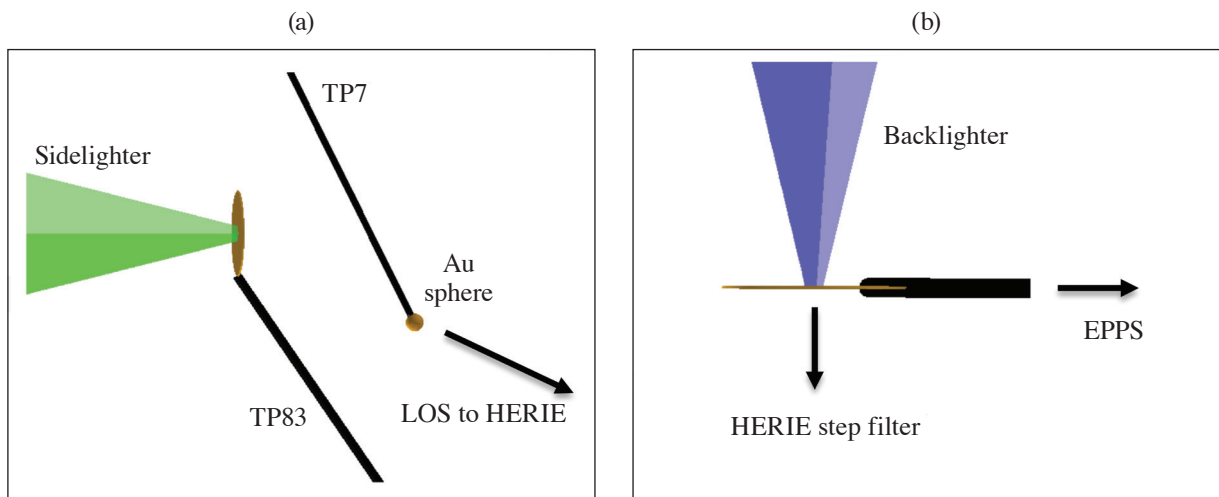
**Characterization of Laser-Driven Magnetic Fields**

Principal Investigator: B. B. Pollock

Co-investigators C. Goyon, J. Williams, D. Mariscal, G. Swadling, J. S. Ross, and J. D. Moody (LLNL) and S. Fujioka, H. Morita, and K. Law (Osaka University)

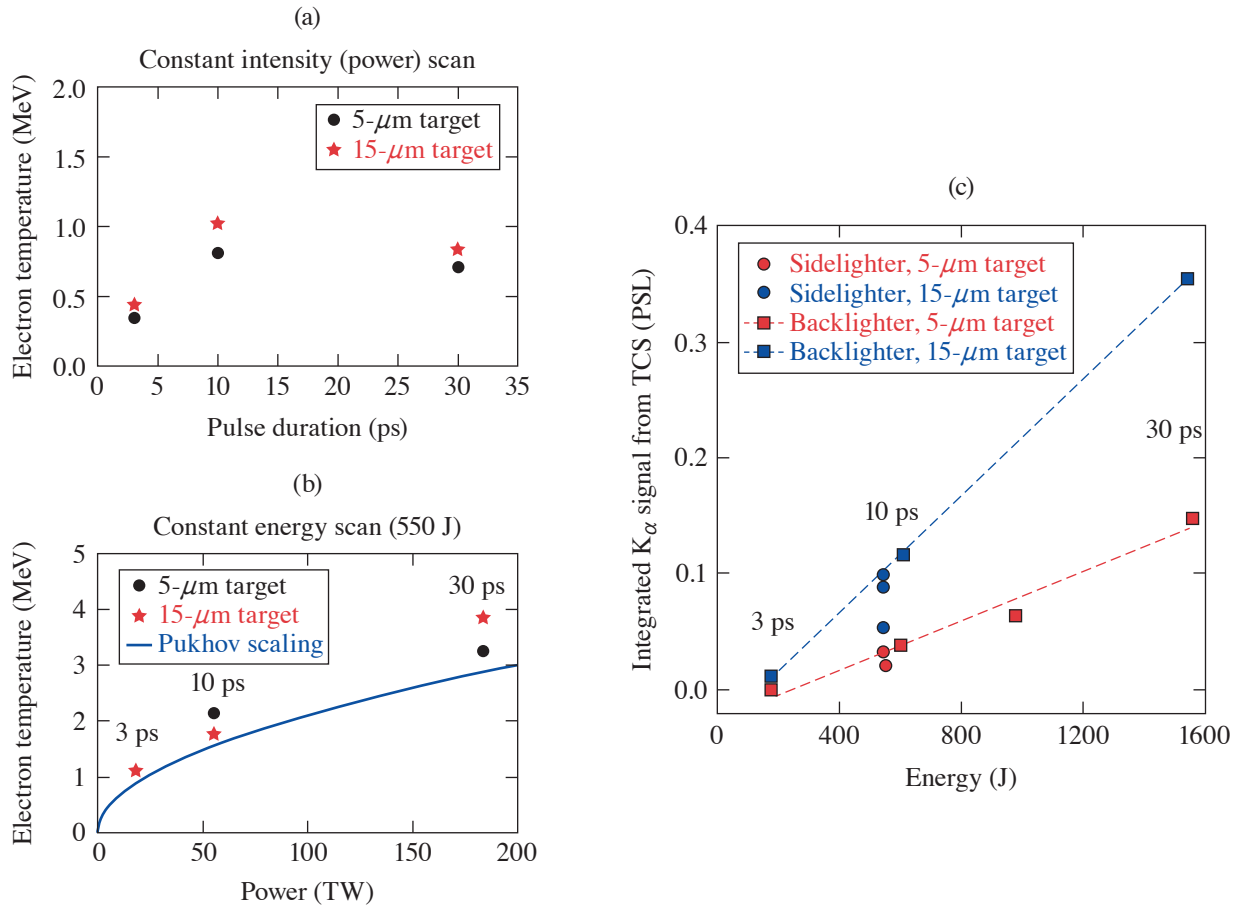
Two shot days on OMEGA EP continued the laser-driven magnetic-field experimental campaign. The goals for FY18 were to study the magnetic-field generation and decay at late times compared to previous experiments (>1 ns), while also expanding the measurement capability of the spatial profile of the magnetic field.

Figure 156.111 shows the general experimental geometry for the BFieldLoop Experimental Campaigns. The field is produced by currents flowing in the Au U-shaped foil target. Long-pulse beams are directed through the holes in the front side of the target to produce a plasma on its interior rear side. Plasma produced in this region expands toward the front side, setting up a voltage across the target, which drives current and produces a magnetic field. The field is measured by proton deflectometry in the fringing field outside the U, and in the high-field region



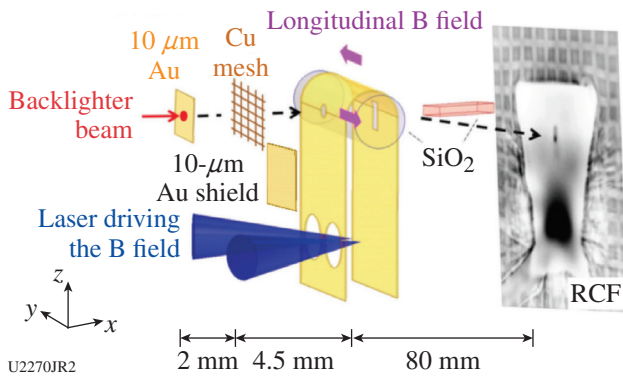
U2388JR

Figure 156.109  
Experimental configuration for the (a) sidelighter and (b) backlighter. LOS: line of sight. EPPS: electron positron proton spectrometer.



U2389JR

Figure 156.110  
Electron temperature measurements at (a) constant power and (b) constant intensity. (c) X-ray  $K_{\alpha}$  yields for all shots.



U2270JR2

Figure 156.111  
Experimental configuration for BFieldLoop experiments.

inside the U through hole/slot pairs in the target surfaces, where the flat-to-curved transition occurs. The protons are produced through TNSA by the backlighter beam on a thin Au foil.

Previous experiments demonstrated that for a 1-TW long-pulse laser drive, fields of  $\sim 200$  T can be produced in the interior of the loop portion of the target in  $\sim 1$  ns. The first FY18 experiment looked at the evolution of the magnetic field at later times, although while the drive pulse was still on. These measurements from 3 to 10 ns showed that the field continued to increase while the 0.5-TW long-pulse drive remained on, albeit at a slower rate than expected in the first nanosecond. The second experiment repeated some of these measurements, but also looked again at time  $< 1$  ns with a reduced 0.5-TW drive beam power (compared to 1 TW in previous shot days). Additionally, these targets added two more hole/slot pairs along the target length to enable measurement of the axial uniformity of the field inside the target.

The field measurements from the second day do show a faster rise of the magnetic field during the first 1 ns of the drive. The slope by 3 ns has become much less steep, even though it

appears the field continues to increase thereafter, as seen in the first day. The representation of this target as a lumped-element circuit with a constant voltage implied a linear ramp in the current with respect to time. The finding of a slope change may drive a different interpretation at later times, but substantial additional analysis is still needed. Furthermore, the proton measurements of the field inside the target seem to indicate that the field is asymmetric along the target length. Improved modeling of the current distribution is underway to assess this observation; there are several experimental methods available to test the controllability of this behavior if it is borne out by modeling. Other hypotheses include target deformation during the drive, but this again will require additional investigation.

**Study of Shock Fronts in Low-Density Single- and Multi-Species Systems**

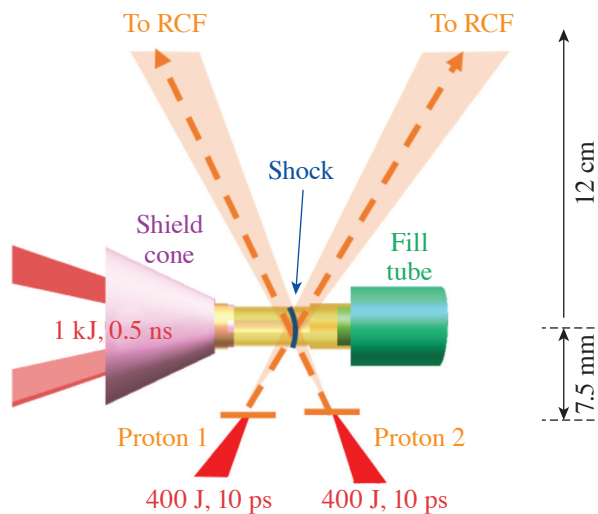
Principal Investigator: R. Hua (UCSD)  
 Co-investigators: Y. Ping, S. C. Wilks, G. W. Collins (now at LLE), R. F. Heeter, and J. A. Emig (LLNL); H. Sio (MIT); and C. McGuffey, M. Bailly-Grandvaux, and F. N. Beg (UCSD)

This series of shots studied the plasma shock structure, especially the associated field structure, of single and multiple species in a low-density system under a planar geometry using TNSA protons and x-ray spectroscopy (Fig. 156.112).

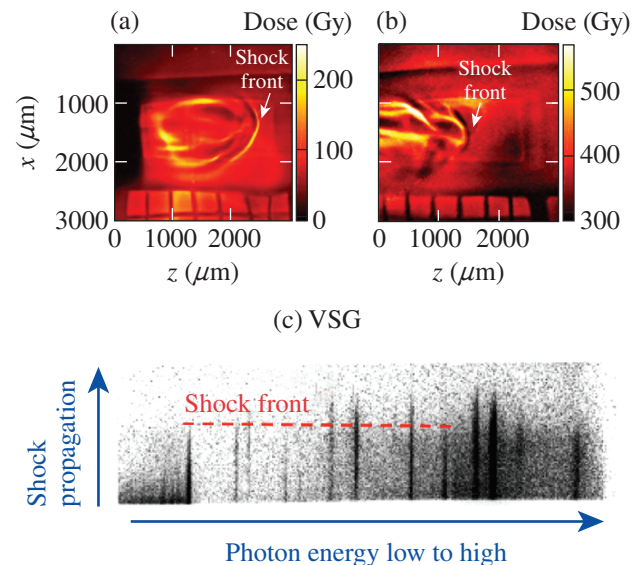
Two or three synchronized long-pulse beams from OMEGA EP delivered several kilojoules of total energy in a

few nanoseconds onto a 2- $\mu\text{m}$  SiO<sub>2</sub> foil that pushed into pure helium or mixed (helium and neon) gases, thereby initiating strong shocks. A short pulse of 400 J in 10 ps illuminated a side-on copper foil a few nanoseconds after the shock creation, creating a burst of protons that probed the propagating shock through two 1- $\mu\text{m}$  windows along the tube. The protons with energies spanning  $\sim 20$  MeV were collected by a radiochromic film (RCF) stack. The relative position from the proton source to the shock front was varied intentionally to distinguish magnetic-from electric-field effects. A 1-D-resolved x-ray spectrometer recorded the emission from the shock front for the inference of temperature and density. The details of the design and its feasibility have been published.<sup>9</sup>

The contrary proton deflection pattern, higher flux ahead (bright ring) or lower flux ahead (dark ring), from two source positions confirms the domination of magnetic field at the shock front since the electric fields deflect protons in a manner that is independent of incident angle (Fig. 156.113). Details of this analysis have been recently submitted. Data analysis of a shock in multi-species composed of 90% helium and 10% neon is in progress. In this shot, radiography data show a double peak of proton flux at the shock front, indicating more-complex field structures. The added neon gas provided useful data for the 1-D-resolved spectroscopy, allowing for the inference of density and temperature profiles along the shock-propagation direction. In addition, spatial correlation between the RCF and x-ray data was achieved from the designed spatial references.



U2391JR  
 Figure 156.112  
 Experimental configuration.



U2271JR2  
 Figure 156.113  
 Raw radiographs and 1-D-resolved spectrum.

## High-Energy-Density Experiments

### 1. Material Equation of State and Strength Measured Using Diffraction

#### *X-Ray Diffraction of Ramp-Compressed Copper up to 1.2 TPa*

Principal Investigator: A. Fernandez-Panella

Co-investigators: R. F. Smith, J. K. Wicks, D. E. Fratanduono, and J. H. Eggert

Copper is an abundant element that has been extensively studied, both experimentally and theoretically, by itself and within the different alloys it forms. It is also commonly used as a pressure standard, flyer plate, and ablator material within the high-pressure community. Its electronic structure is simple with the 3d shell completely filled; accurate shock wave and ramp-compression data are available up to a few Mbar (Refs. 76–80); and copper's fcc (face-centered cubic) phase structure is predicted to remain stable up to very high pressures.<sup>81</sup>

Along the Hugoniot, Cu melts above 200 GPa. To determine its stable solid-phase structure at higher pressures, a low-temperature, off-Hugoniot compression path is required. The purpose of the CuDiff-18B Campaign was to measure x-ray diffraction data of ramp-compressed Cu up to 1.2 TPa. Figure 156.114

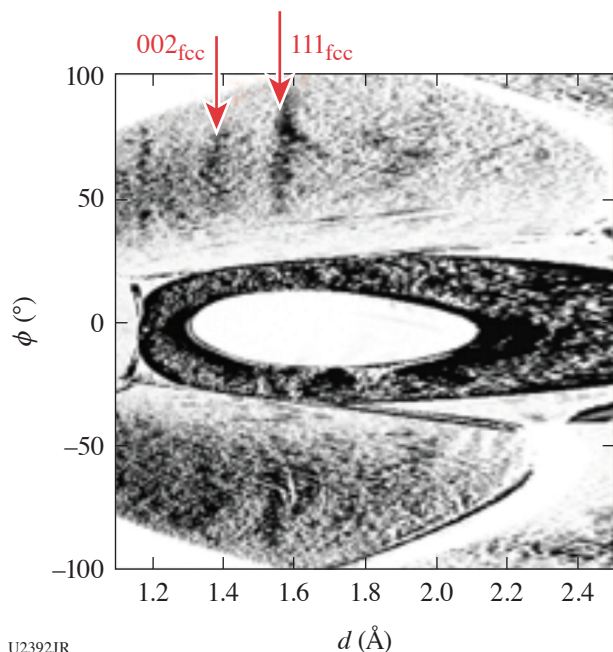


Figure 156.114

X-ray-diffraction measurement of ramp-compressed Cu at 1165 GPa. The observed lines (marked with red arrows) correspond to the fcc phase structure.

shows an example of x-ray diffraction data at 1165 GPa. The results are summarized in Fig. 156.115. They indicate that, along the isotherm, copper remains in the fcc phase structure up to the highest pressures explored in this study, 1.2 TPa. These results supplement the recent EOS ramp-compressed data measured on the NIF up to 2.4 TPa and have been included in the manuscript for publication.

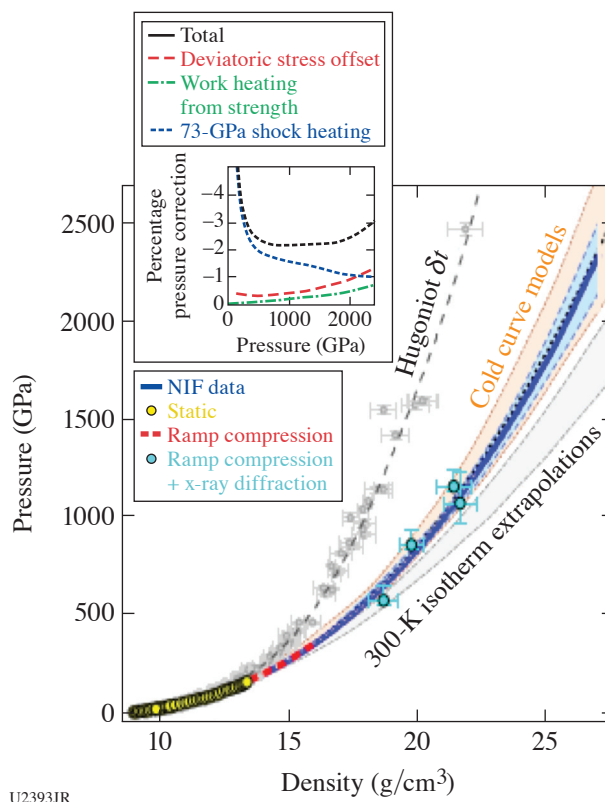


Figure 156.115

Pressure-density plot of copper. Hugoniot data,<sup>80</sup> ramp compressed (red<sup>82</sup> and blue curves<sup>84</sup>), and several theoretical cold curves (dashed gray lines) and the extrapolated isotherm at 300 K (solid gray line) are shown. The corresponding fcc pressure states measured on the OMEGA laser are indicated with solid blue circles.

#### *Examination of the High-Pressure Structures of Ramp-Compressed Germanium and Zirconium*

Principal Investigator: J. V. Bernier

Co-investigators: R. Kraus, C. Wehrenberg, A. Krygier, and J. H. Eggert

This campaign was designed to quantify the hydrodynamic responses and high-pressure crystal structures in both germanium and zirconium subject to ramp compression. Both of

these materials are commonly used as x-ray backlighter sources ( $\text{He}_\alpha$ ) across the HED campaigns, and they are also used as filter layers in physics packages. There is, however, a dearth of data regarding the crystal structures in these materials at moderately high pressures relevant to many ramp-compression experiments. The specific objectives were (1) to assess the fidelity of the modeled hydrodynamic responses (as a check on the available EOS's); and (2) to measure the high-pressure structures of both materials via diffraction patterns measured on the powder x-ray diffraction image-plate (PXRDP) diagnostic. The second goal is particularly important for identifying the contribution of Ge/Zr filter layers to diffraction data for physics packages using those materials.

This campaign used a single day on OMEGA EP, with two shot designs for each material: one for ramp compression to 1.2 Mbar, and another for ramp compression to 2.4 Mbar. This comprised four unique target material/drive configurations, which were duplicated to mitigate risk of a missed measurement. The drive designs consisted of two stitched pulse shapes (two sequential beams) to define a 20-ns ramp, while the Ge backlighters were driven using the same pulse shape on each of the remaining two beams. The physics packages consisted of beryllium ablaters, 20  $\mu\text{m}$  of Ge or Zr, and a LiF window mounted to W pinholes on the PXRDP diagnostic. Germanium backlighters were used to generate  $\sim 1$ -ns duration x-ray pulses to interrogate the target material at the predicted peak pressure state. Velocimetry of the LiF/Ge (or Zr) interface was measured via active shock breakout (ASBO) for comparison to simulations. Lastly, the x-ray spectrometer, pinhole cameras, and single-photon counting (SPC) spectrometer were fielded to assess backlighter performance.

Excellent ASBO measurements delivered high-fidelity velocimetry for each material/pressure configuration, which demonstrated good agreement with post-shot simulations (see Fig. 156.116). This suggests adequate fidelity in the EOS's used for Ge and Zr over these pressure ranges. Issues with backlighter performance, however, led to a loss of PXRDP data for both shots studying Ge at 1.2 Mbar. The 2.4-Mbar Ge data indicated fairly weak scattering from a non-cubic solid phase. The diffraction data for the Zr shots also show diffraction from solid, non-cubic phases, but with strong preferred orientation. Analysis of these results is ongoing, with the goal of producing a peer-reviewed publication. The results of this campaign—specifically the positions of strong Bragg lines—will be used to help interpret diffraction data for targets using Ge and/or Zr filter layers in the future.

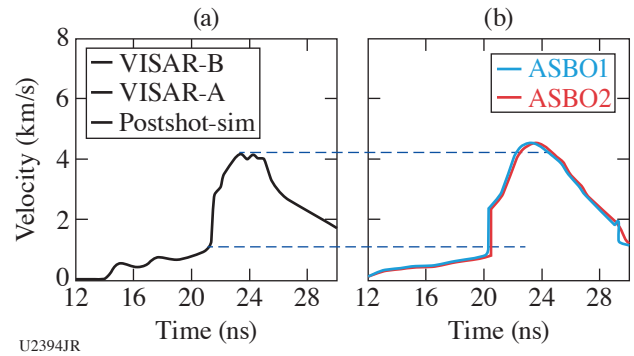


Figure 156.116

Velocimetry results for 1.2-Mbar Ge. The Ge/LiF interface velocity from the (a) post-shot simulation shows good agreement with (b) ASBO measurements.

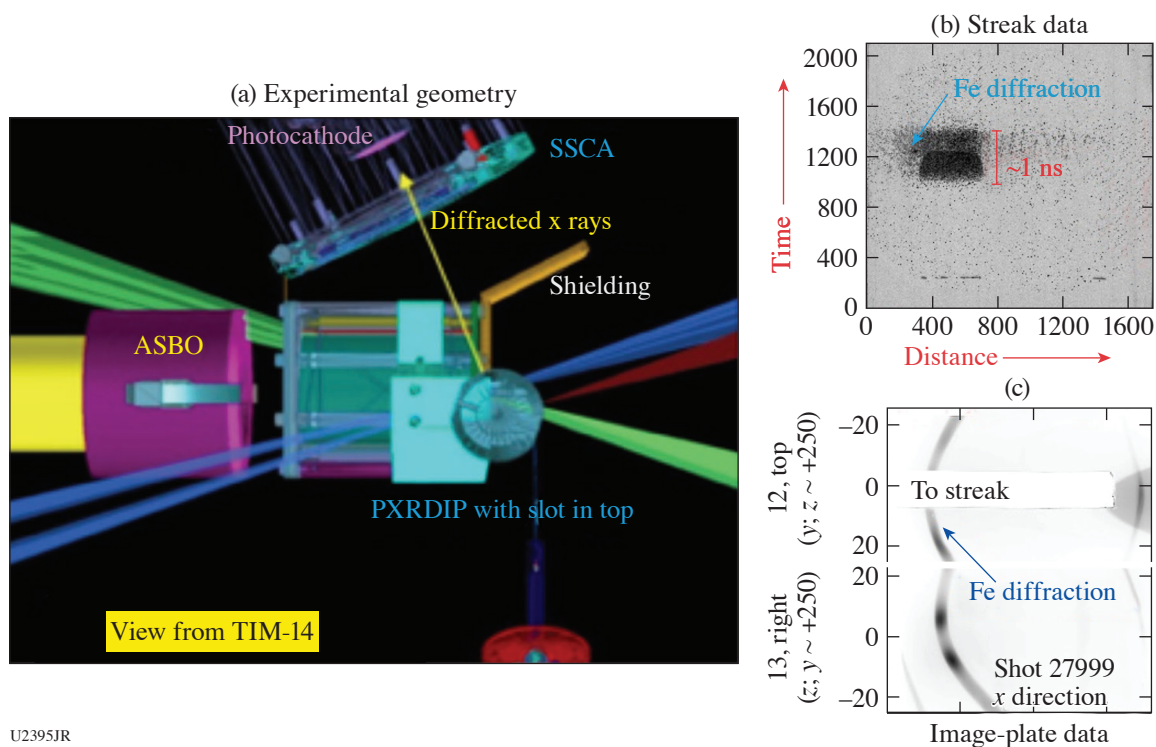
### Development of Time-Resolved X-Ray Diffraction Techniques

Principal Investigator: L. R. Benedetti

Co-investigators: F. Coppari, J. R. Rygg, A. E. Jenei, J. H. Eggert, G. W. Collins, D. K. Bradley, and J. D. Kilkenny

Two FY18 shot days on OMEGA EP were used for development of a capability to measure x-ray diffraction of compressed materials at multiple times during a single-laser experiment. The experimental design is based on the PXRDP platform that has already been successfully used to measure x-ray diffraction of compressed materials onto image plates. The idea of this campaign was to adapt the PXRDP platform to allow access to an x-ray streak camera to measure a continuous record of x-ray diffraction in addition to the image-plate measurement (see Fig. 156.117).

The entire series of shots used an iron target and a laser pulse designed to drive the iron through the  $\alpha$ - $\epsilon$  phase transition. The first shot day confirmed the pressure history and phase transformation with VISAR and image-plate data. However, no coherent data were found on the x-ray streak camera. The second shot day reduced electronic noise to the streak camera by moving it from TIM-14 to TIM-10 and substantially reduced x-ray backgrounds by adding additional shielding. With these changes and also an enlarged target, the first streaked x-ray diffraction was seen for an undriven (uncompressed) target [Fig. 156.117(b)]. Streak diffraction has not yet been observed in a compressed target, and the data suggest that the streak-camera gain mechanism is substantially upset by the interaction of the drive laser pulse with the PXRDP target. An upcoming campaign in FY19 is planned to address the electromagnetic upset of the streak camera by replacing the PXRDP with a smaller target geometry, and to explore the use of imaging diagnostics to complement the streaked diffraction data.



U2395JR

Figure 156.117

(a) Experimental geometry showing the close approach of the x-ray streak camera to the PXRDIP. (b) X-ray diffraction of uncompressed iron streaked on film and (c) integrated on an image plate.

### Development of an In-Situ Pressure Standard for Diffraction Experiments

Principal Investigator: F. Coppari

Co-investigators: J. H. Eggert and R. Kraus

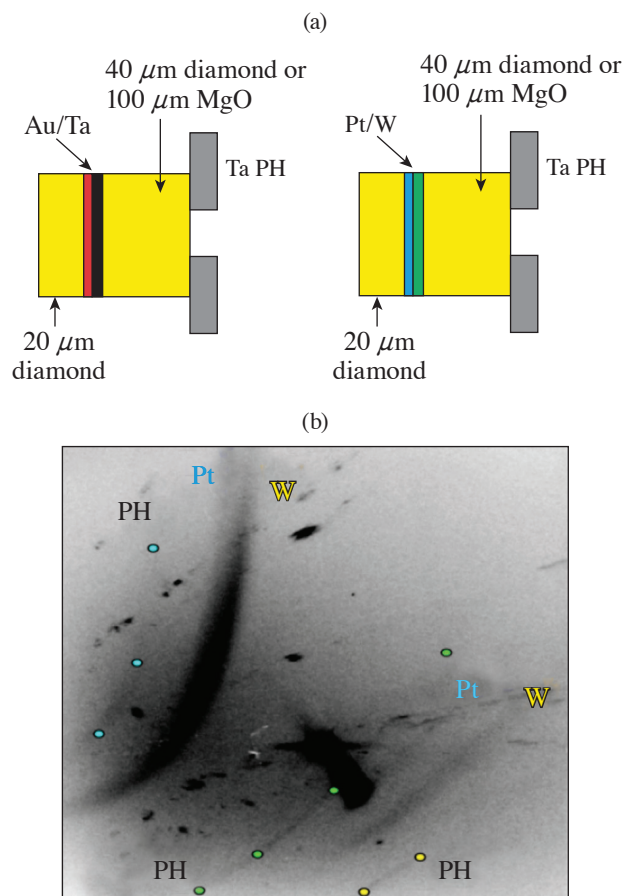
The goal of this campaign is to develop a new way of determining pressure in diffraction experiments based on the use of an *in-situ* pressure gauge. By measuring the diffraction signal of a standard material (whose equation of state is known) compressed together with the sample, one can determine the pressure upon ramp compression.

Currently, pressure is determined from VISAR measurements of diamond free-surface velocity or particle velocity through a transparent window (such as LiF or MgO). This method is, in some cases, ambiguous (lack of reflectivity or shock formation) or relies on assumptions and EOS models. Cross-checking the VISAR measurement with *in-situ* pressure determination using the diffraction signal of a standard material will improve the diffraction platform by providing a complementary way of determining the pressure state within the sample, with great impact to the broader effort of determining structures and phase transitions at high pressure and temperature. In addition, com-

binning pressure determination from VISAR and from the *in-situ* gauge can give information about the temperature of the sample by measuring the calibrant thermal expansion.

Building upon the results obtained in previous campaigns that focus on diamond windows and ramp compression at 200 GPa, the goals for the half-day campaign in FY18 were to push to higher pressure and to extend the study to other window materials, such as MgO and LiF. Half of the shots looked at the diffraction patterns of the Au/Ta and Pt/W pairs coated on diamond windows [Fig. 156.118(a)] and ramp compressed to 400 GPa. The other half were ramp-compression experiments to 200 GPa using MgO windows. All shots gave good-quality data [Fig. 156.118(b)] and analysis is being finalized. Comparison of the pressures obtained from VISAR analysis and from the diffraction patterns provides information regarding the accuracy of the VISAR method as well as the possible existence of preheating.

Future directions of this work will look at characterizing the pressure standards at higher pressure and implementing this technique into a real diffraction experiment. Although this platform still needs some development effort before it can be routinely used in diffraction experiments, the data collected so



U2396JR

Figure 156.118

(a) Schematic of the target assembly. Diamond or MgO windows were coated with 1- $\mu\text{m}$ -thick Au/Ta or Pt/W pairs used as pressure standards in the diffraction experiment. All targets had a 20- $\mu\text{m}$  diamond ablator and were mounted on Ta pinholes. (b) Representative raw diffraction data. The dots overlap with the diffraction signal from the Ta pinhole, while labels point to the signals from compressed Pt and W. At least two diffraction lines are observed for each standard.

far are extremely encouraging and suggest that the use of an *in-situ* pressure gauge can be a viable path forward in future x-ray diffraction measurements on both OMEGA and the NIF.

## 2. Material Equation of State Using Other Techniques

### **Development of a Platform for Equation-of-State Measurements Using Mo Flyer-Plate Impact**

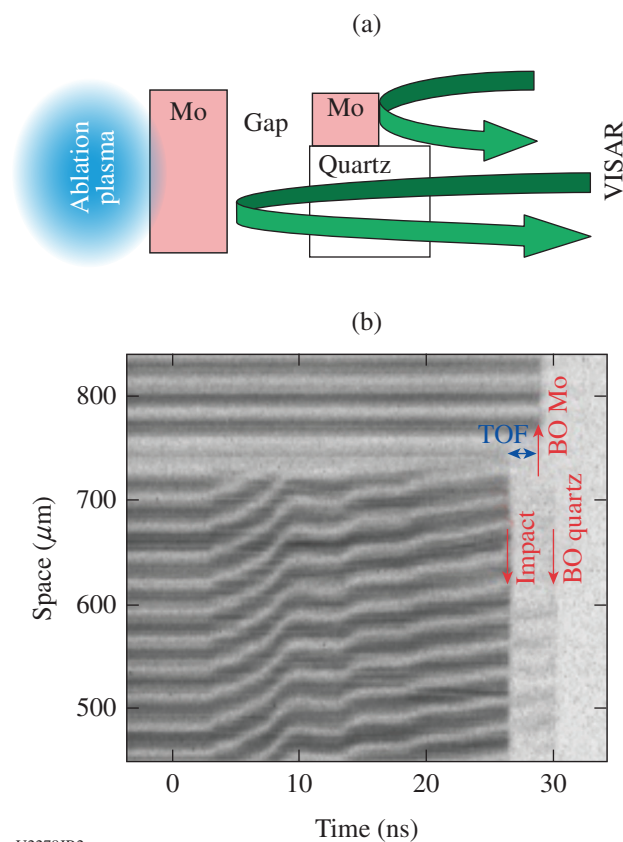
Principal Investigator: F. Coppari

Co-investigators: R. London, P. M. Celliers, M. Millot, D. E. Fratanduono, A. Lazicki, and J. H. Eggert

This campaign is developing a platform to use the OMEGA laser to accelerate flyer plates to hypervelocity for absolute

EOS measurements by symmetric impacts. The concept is to use ramp compression to accelerate a molybdenum (Mo) foil across a vacuum gap through indirect laser ablation and observe the flyer impact on a same-material sample mounted side by side with a transparent quartz window (see Fig. 156.119). By measuring the flyer-plate velocity prior to impact through the transparent window, and the resulting shock velocity in the Mo sample using transit-time measurements, the principal Hugoniot of Mo can be determined *absolutely* (e.g., without needing a known pressure reference), enabling the development of an EOS standard. This platform will be valuable for all activities interested in EOS and Hugoniot measurements at pressures higher than 12 Mbar, where currently there are no materials whose EOS has been experimentally determined.

The FY18 shots built on the results obtained in FY17. Target design was improved by changing window material from LiF



U2278JR2

Figure 156.119

(a) Schematic of the experimental setup. A Mo foil is accelerated across a vacuum gap and impacted on a transparent quartz window, side by side with a Mo foil. Simultaneous VISAR measurements of the flyer velocity and shock velocity upon impact give a measurement of the Mo EOS without the need to rely on the EOS of a reference material. (b) Representative VISAR record. The main events are indicated by arrows.

to quartz. This allows both a better measurement of the flyer velocity prior to the impact and also enables shock velocity to be measured in the quartz after the impact, therefore being able to cross check the shock state obtained in the Mo. The first half-day explored the Hugoniot of Mo up to shock speeds of 18 km/s. The second half-day pushed to higher velocities (higher pressure) and filled in data-set gaps at lower velocity, to be able to better compare these results with different measurements and validate the platform.

**Development of a Platform for Absolute Equation-of-State Measurements Using Diamond Flyer-Plate Impacts**

Principal Investigator: F. Coppari

Co-investigators: R. London, P. M. Celliers, M. Millot, D. E. Fratanduono, A. Lazicki, and J. H. Eggert

This campaign develops a platform to accelerate diamond flyer plates to hypervelocity for absolute (i.e., reference-free) EOS measurements. Ramp compression of diamond through direct laser ablation results in a slow acceleration of the diamond across a vacuum gap. After propagating a known distance, the diamond flyer impacts on a transparent diamond window. By measuring the diamond flyer-plate velocity prior to impact and the resulting shock velocity in the diamond witness, the principal Hugoniot of diamond can be determined *absolutely* (e.g., without needing a known pressure reference),

enabling the development of diamond as an EOS standard. Figure 156.120 illustrates the approach and sample data. Note that this campaign is relevant to all activities interested in EOS and Hugoniot measurements at pressures higher than 12 Mbar, where currently there are no materials whose EOS has been experimentally determined.

The specific goal of the FY18 half-day was to fill in gaps in the data set and push to higher pressure. With eight successful shots, the diamond Hugoniot EOS was characterized up to about 30 km/s (corresponding to 15 Mbar). Experience gained in past campaigns led to improvements in target design, resulting in extremely high-quality data. Data analysis now underway is expected to result in an accurate EOS for diamond measured without relying on the EOS of reference materials.

**Equation-of-State Measurements from CH Foam in a Spherically Convergent Geometry**

Principal Investigator: A. M. Saunders

Co-investigators: A. Jenei, T. Doepfner, M. J. MacDonald, D. Swift, H. Whitley, and J. Nilsen

This experimental campaign aimed to develop a technique to make off-Hugoniot EOS measurements in CH by compressing half-density CH foam in a spherically convergent geometry. The lower starting density allows the spheres to reach higher

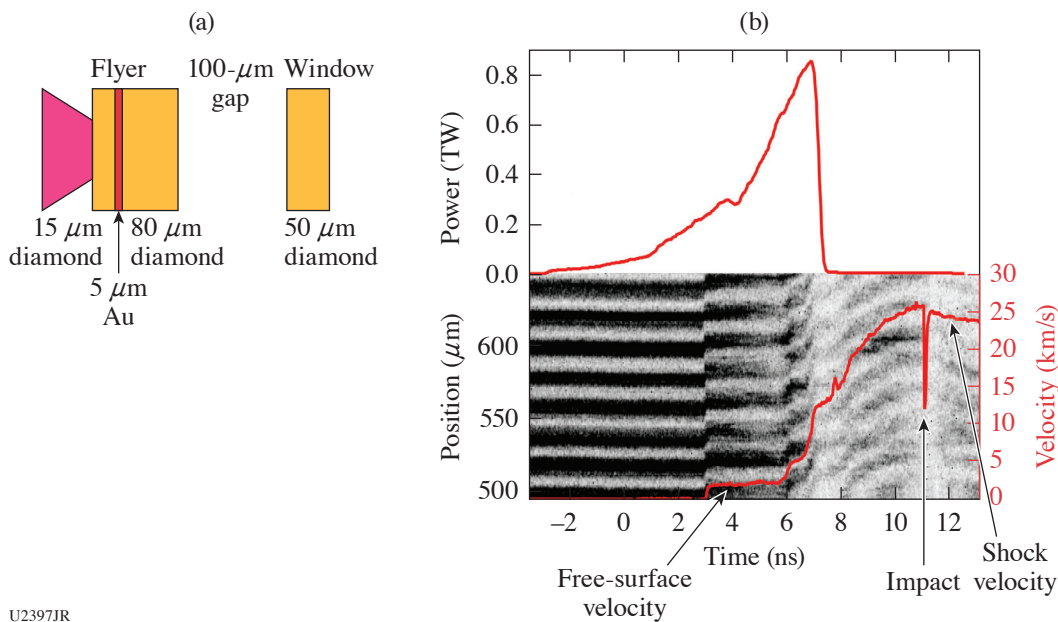


Figure 156.120  
 (a) Diamond-flyer experimental configuration. (b) Sample VISAR data.

temperatures as the shock coalesces, which can provide EOS measurements at pressures exceeding 100 Mbar. There is currently a dearth of experimental data to benchmark EOS models at such extreme conditions. In addition, the campaign sought to establish a new technique to measure temperature within the shock front: x-ray fluorescence spectroscopy.

Figure 156.121(a) shows a schematic of the experimental configuration. Fifty-two laser beams directly drive a foam capsule for 1 ns. As the sphere compresses, eight laser beams heat a foil suspended at the bottom of a plastic cone to generate a He $\alpha$  x-ray backlighter; the plastic cone contains the spread of plasma. An x-ray framing camera (XRFC) with a pinhole array takes backlit 2-D time-gated images of the capsule as it implodes, and the XRS spectrometer measures the emission spectrum from the backlighter foil and the capsules. The half-density CH foam capsules are 500  $\mu$ m in diameter with 20- $\mu$ m-thick ablator layers of glow-discharge polymer (GDP) plastic. This is the first time such capsules were used and required significant R&D from General Atomics. Several of the foam spheres are doped with 1 at.% Cu; this doping process is also new, and dopant concentrations were uneven inside the spheres. Pictures of the assembled targets from the OMEGA shot day can be seen in Fig. 156.121(b). The backlighter foil

is vanadium for the undoped capsules and germanium for the Cu-doped capsules.

The FY18 shots acquired high-quality data from the Cu-doped capsules, but the vanadium He $\alpha$  backlighter proved too high in energy to resolve the shock front in the capsules without a dopant. Figure 156.121(c) shows four framing-camera images from a Cu-doped capsule. The shock front is seen progressing toward the center until shock coalescence, around 1 ns. XRFC data were also collected for the Cu-doped spheres and will be compared with simulations in order to benchmark the temperatures of the samples. Analysis of the data is ongoing. In addition, the foam capsules developed as a result of this campaign were subsequently used in a NIF discovery science shot day. Future campaigns will improve upon the platform to provide benchmarking EOS measurements of materials at extreme conditions.

**Developing a Conically Convergent Platform for Measuring Hugoniot Equation of State in the 100-Mbar–Gbar Pressure Regime**

Principal Investigator: A. E. Lazicki  
 Co-investigators: M. C. Marshall, D. Swift, F. Coppari, R. London, D. Erskine, H. Whitley, and J. Nilsen

This campaign continued to develop a platform for measuring Hugoniot EOS of arbitrary (including high-Z) materials at pressures much higher than can be achieved using a standard planar drive. This platform is intended to collect data in the >100-Mbar pressure regime, where currently very little data exist for any material, for the purpose of constraining EOS models.

To achieve the desired pressure amplification, converging shock waves are launched into a plastic cone inset in a half-raum. For appropriate cone angles, nonlinear reflections of the shock wave result in formation of a Mach stem: a planar high-pressure shock that propagates along the axis of the cone.

This new platform was tested during one half-day in FY16 and one half-day in FY17, showing that a high-pressure Mach stem formed, but it was not supported through the full thickness of the cone and impedance-matching physics package, primarily because of the pulse-length limitations for the highest energy drives; a release wave rapidly degrades the Mach wave after the 1-ns drive turns off. The two half-day campaigns in FY18 tested a reduced-scale hohlraum and cone, longer pulse lengths, and a low-pressure gas fill to support the Mach stem long enough to perform an EOS measurement. The campaigns

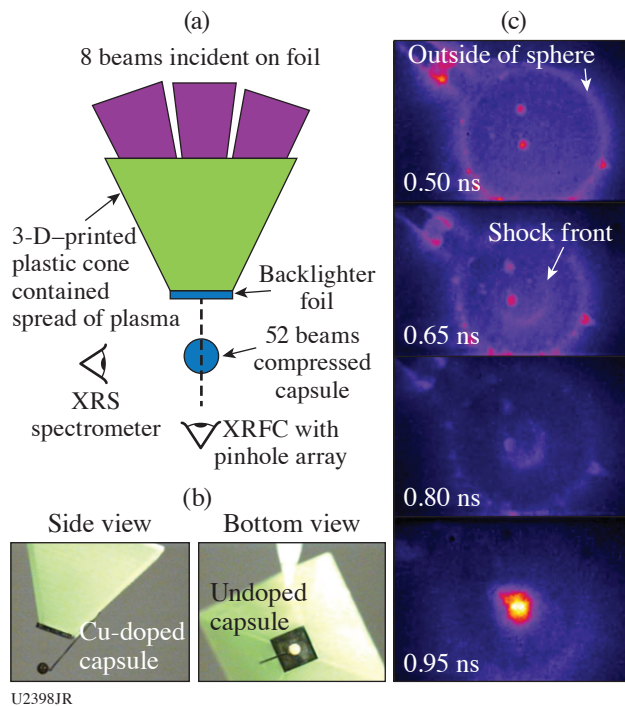


Figure 156.121  
 (a) Experimental configuration, (b) target photos, and (c) x-ray framing-camera data from shot 88630.

also experimented with various thicknesses of Au heat shielding in the targets, as well as bromine-doping of the Mach cones to mitigate preheat.

In the FY18 shots, the small hohlraums easily generated 100-Mbar states in the targets [Fig. 156.122(a)] but also generated sufficient hard x rays to cause the target surfaces to quickly lose reflectivity, even when thick (25- $\mu\text{m}$ ) Au heat shields were employed. In the absence of reflected VISAR light, shock-wave breakouts were registered using the thermal signature in the streaked optical pyrometer. Longer pulse lengths effectively delayed the release waves [Fig. 156.122(b)], but the surface area of the Mach wave is too small at this reduced scale to make a high-accuracy EOS measurement with the current VISAR optics. Inclusion of a gas had no consistent observable effect on the Mach-wave propagation. The second half-day added diagnostics to collect data on hard x-ray and hot-electron production, which are being analyzed to understand how to mitigate the preheat. Future shots will increase the hohlraum scale and the length of the drives, and we will experiment with techniques for quantifying the preheat.

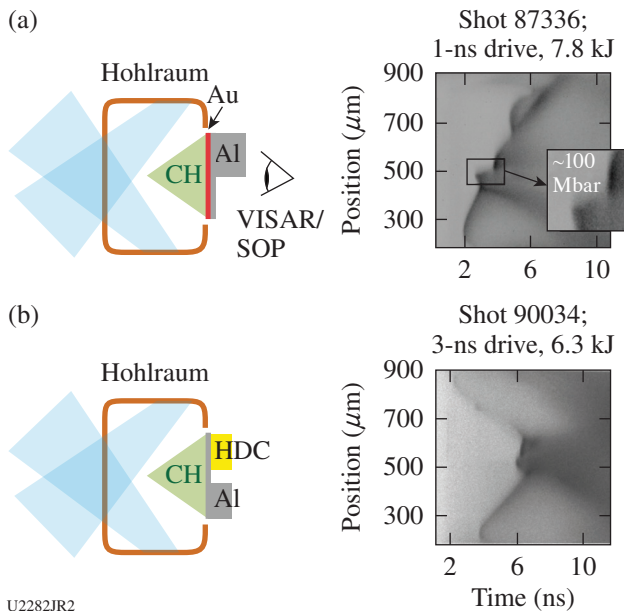


Figure 156.122 Target configuration and shock-wave breakout measured with the streaked optical pyrometer (SOP) for two FY18 shots. (a) The effect release waves degrading the central quasi-planar region of the driver. The breakout times from 20- $\mu\text{m}$  and 100- $\mu\text{m}$  Al steps indicate a shock velocity corresponding to  $\sim 100$  Mbar in Al. (b) Data obtained with a longer (3-ns) drive and lower energy, effectively delaying the release waves. However, the planar region of the Mach drive is too small to encompass both Al and high-density carbon (HDC) steps and the Al base in the impedance-matching target.

### Experiments to Test the Effect on Target Reflectivity of Release Across a Phase Boundary

Principal Investigator: R. F. Smith

Co-investigators: A. Fernandez Pañella and D. E. Fratanduono (LLNL) and J. Wicks (Johns Hopkins University)

The goal for the PhaseTransRelEP-18A (6 December) Campaign was to determine how pressure release across a phase boundary affects target reflectivity. These experiments were in support of ramp EOS experiments conducted on the NIF.<sup>82</sup> The target design for these experiments is shown in Fig. 156.123 and consists of a 50- to 75- $\mu\text{m}$  CH ablator, a 20- to 30- $\mu\text{m}$  layer of either Pb, Sn, or Fe, and over the 1-mm VISAR field of view, a free-surface region, a region with a LiF window, and a region with an MgO/sapphire window. These experiments used the 10-ns ERM99v016 pulse shape to drive a temporally steady shock into the target assembly. Sample free-surface velocity ( $u_{fs}$ ), particle velocity ( $u_p$ ), and reflectivity were monitored with the line-VISAR (ASBO) system. Drive-beam energies were varied from 67 to 755 J to generate different initial pressure states along the shock Hugoniot.

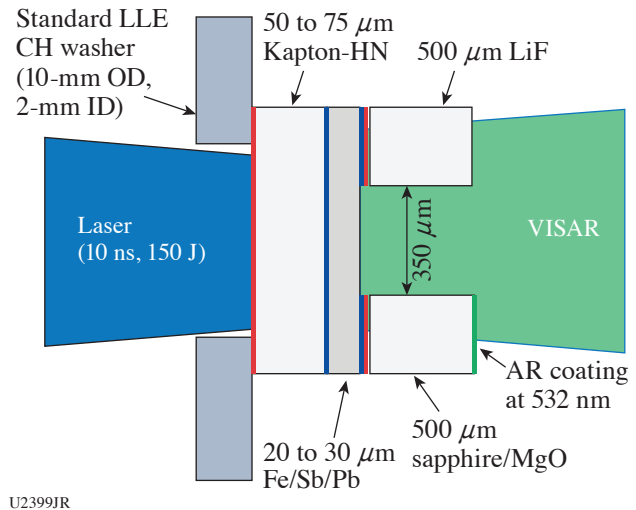


Figure 156.123

Target design for phase transformation release on OMEGA EP. Under steady-shock conditions, VISAR measures the sample free-surface velocity and sample window particle velocity.

In this experiment, shock compression is followed by isentropic pressure release. Depending on the initial shock-compression state, isentropic pressure release may cause the material to decompress across a solid–solid phase boundary or a solid–liquid phase boundary. These experiments measured the

correlation between free-surface target reflectivity with release from different shock states and found that while the free-surface reflectivity was virtually unperturbed by isentropic release across solid–solid phase boundaries, it dropped precipitously for pressure release paths across solid–liquid phase boundaries.

In addition, these data allow a test of the commonly used approximation of  $u_{fs} = 2 \times u_p$ . Some preliminary VISAR data are shown in Fig. 156.124. Figure 156.124(a) shows the VISAR fringe movement from the Fe/sapphire and Fe free-surface velocity interfaces. The associated extracted velocity profiles are shown in Fig. 156.124(b) (red traces). Predicted outputs from a *HYADES* 1-D hydrocode simulations are shown as black dashed traces. Velocity structure on the way to peak velocity is caused by changes in material sound speed associated with the  $\alpha$ – $\epsilon$  phase transformation.

### Liquid–Ice VII Phase Transition Kinetics in Ramp-Compressed Water

Principal Investigator: M. C. Marshall

Co-investigators: D. E. Fratanduono, M. Millot, and R. F. Smith

The goal of the FY18 RampWater shot series was to observe the liquid–ice VII phase transition in water ramp compressed along its principal isentrope at ultrahigh strain rates ( $>10^6 \text{ s}^{-1}$ ). The isentrope crosses the phase boundary at  $\sim 2.5 \text{ GPa}$ ; however, ramp-compression experiments at the Sandia Z machine showed an overpressurization of the phase transition at  $7 \text{ GPa}$  (Ref. 83). An LLNL kinetics algorithm predicts freezing at  $\sim 9 \text{ GPa}$  for the OMEGA experiments, which have  $\sim 10\times$  higher strain rates than the Z experiments.

Two half-day campaigns were performed on OMEGA. Water was ramp compressed using a release reservoir design in which shocked CH releases across a vacuum gap and isentropically loads the water cell, as shown in Fig. 156.125. A thin water layer ( $\sim 20 \mu\text{m}$ ), created using a sapphire “diving-board” configuration inside the water cell, was ramp compressed to  $\sim 15 \text{ GPa}$ . The experiments were designed to observe two signatures of the phase transition using VISAR. The first is a stress release on the rear sapphire window of the thin water layer caused by volume collapse during the transition (ice VII is 60% more dense than liquid water). The second is a coincident dip in transmission through the water layer from optical scattering of the coexisting liquid and ice phases with different refractive indices.

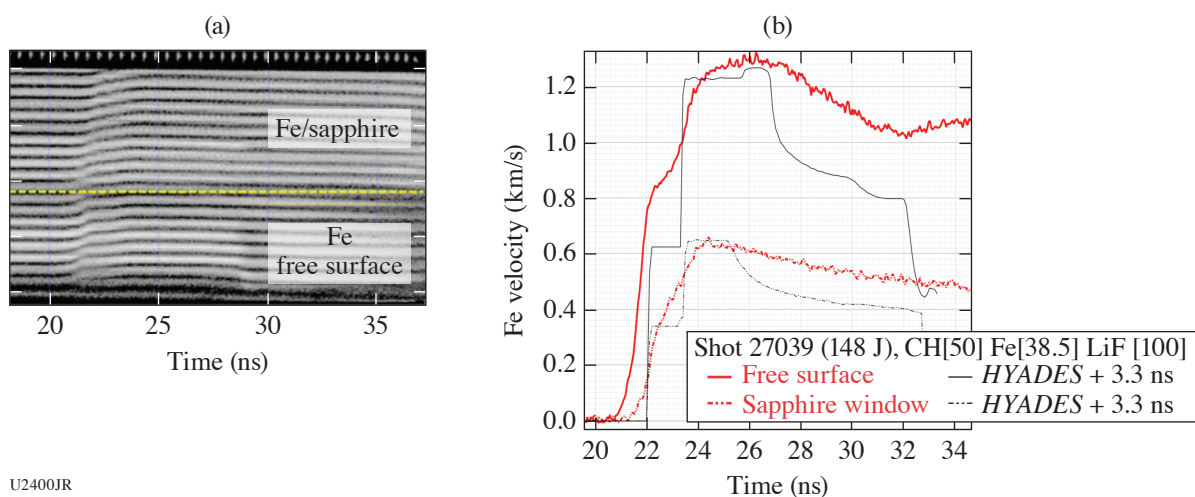
Preliminary analysis indicates possible stress-release signatures near the predicted pressure of  $9 \text{ GPa}$  in several shots, but no clear evidence for transient opacity has been identified so far. Analysis is ongoing to discern the stress release on the water/Al/sapphire interface [Fig. 156.125(b)] and a follow-up campaign is scheduled on OMEGA EP in FY19.

### First Measurements of the Single-Crystal TATB Hugoniot to 80 GPa

Principal Investigator: M. C. Marshall

Co-investigators: A. Fernandez Pañella, T. Myers, J. H. Eggert, T. Bunt, L. Lauderbach, and L. D. Leininger

The purpose of the HEEOSEP-18A Campaign was to measure the Hugoniot of TATB (triamino-trinitrobenzene) shocked to high pressure. TATB is a high explosive known for its insensitivity to high temperatures and impacts. Experiments were



U2400JR

Figure 156.124

(a) Raw VISAR data showing regions of Fe/sapphire and Fe free surface. (b) Extracted velocity profiles and simulations from the *HYADES* hydrocode.

done on the OMEGA EP laser, where TATB [Fig. 156.126(a)] was shocked to a range of pressures (15 to 80 GPa) over eight shots. Hugoniot data were obtained by impedance matching relative to an aluminum standard. Planar targets had a Kapton

ablator, aluminum base plate (standard), single-crystal TATB sample, and LiF witness used to correct for shock unsteadiness. Three laser beams with total energies of 580 to 2300 J were stacked in time, producing a 30-ns drive to support a

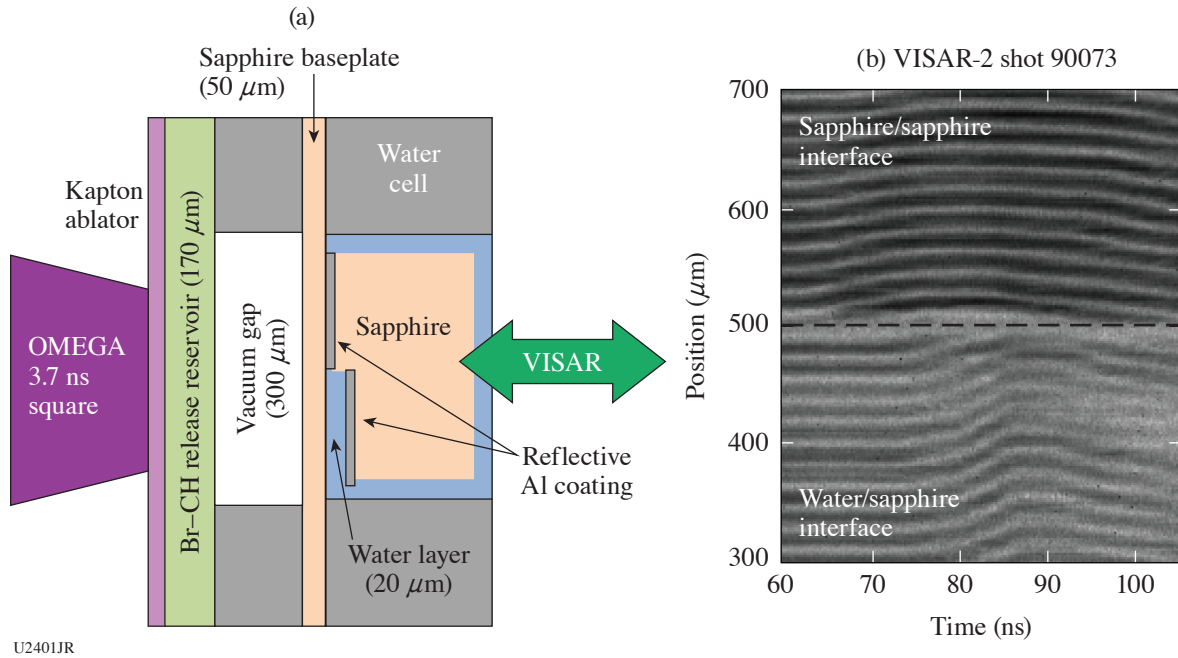


Figure 156.125

(a) Target design for a stress-release measurement. (b) Corresponding VISAR image showing interface motion of the two Al-coated surfaces inside the water cell. The velocity of the sapphire/Al/sapphire interface (upper region in water cell and VISAR data) provided a drive measurement for each target shot.

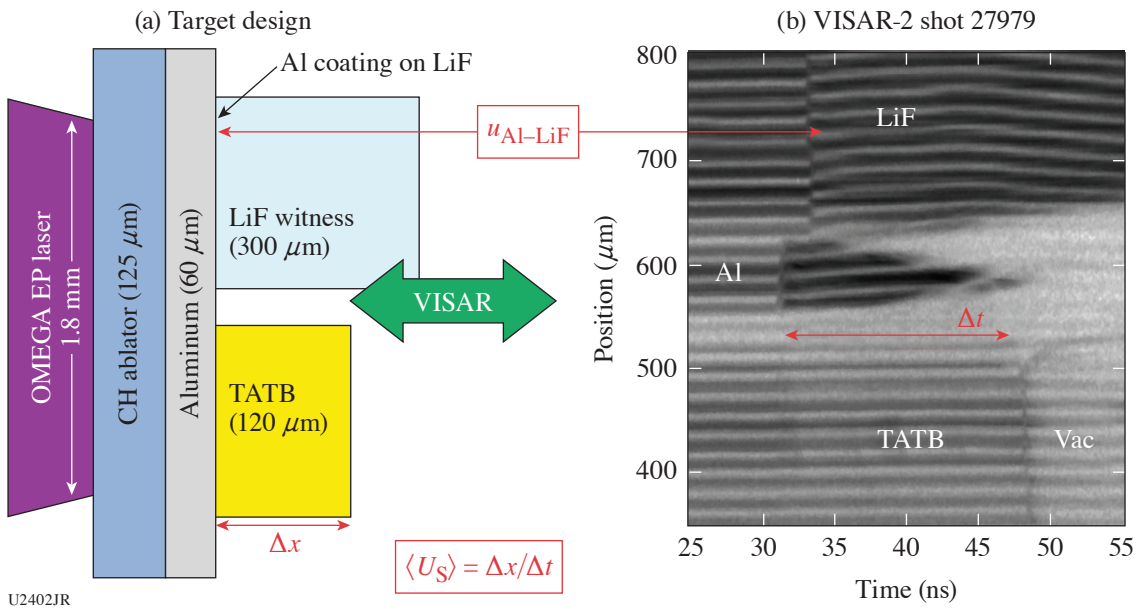


Figure 156.126

(a) TATB target design and (b) VISAR data showing the shock transit time ( $\Delta t$ ) in TATB, and the Al/LiF interface velocity.

nearly steady shock in the TATB. VISAR was used to measure interface velocities and shock transit times needed for the impedance-match analysis. The results [Fig. 156.126(b)] will be used to improve predictive modeling for TATB.

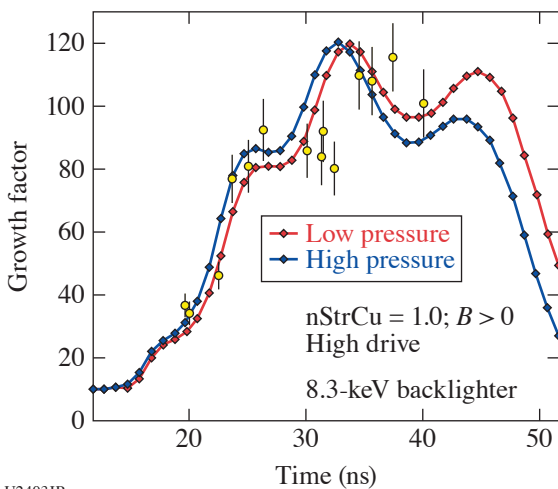
### 3. Material Dynamics and Strength

#### Rayleigh–Taylor Growth in Ramp-Compressed Copper

Principal Investigator: J. M. McNaney

Co-investigators: S. Prisbrey, A. Krygier, and H.-S. Park

The CuRT-EP-18A series of shots investigated inconsistencies in the liquid copper Rayleigh–Taylor (RT) data from previous FY17 campaigns. The previous campaigns indicate that the simulated growth behavior is not capable of matching the liquid RT growth throughout the entire loading history (Fig. 156.127). As RT growth is driven by acceleration of the ripples into a lower-density medium, it appears the acceleration history in the simulations did not sufficiently represent the driving force actually seen in the experiment.



U2403JR

Figure 156.127  
Comparison of simulations (solid lines from bounding cases) and experiments (yellow points from CuRT-EP-17A and B).

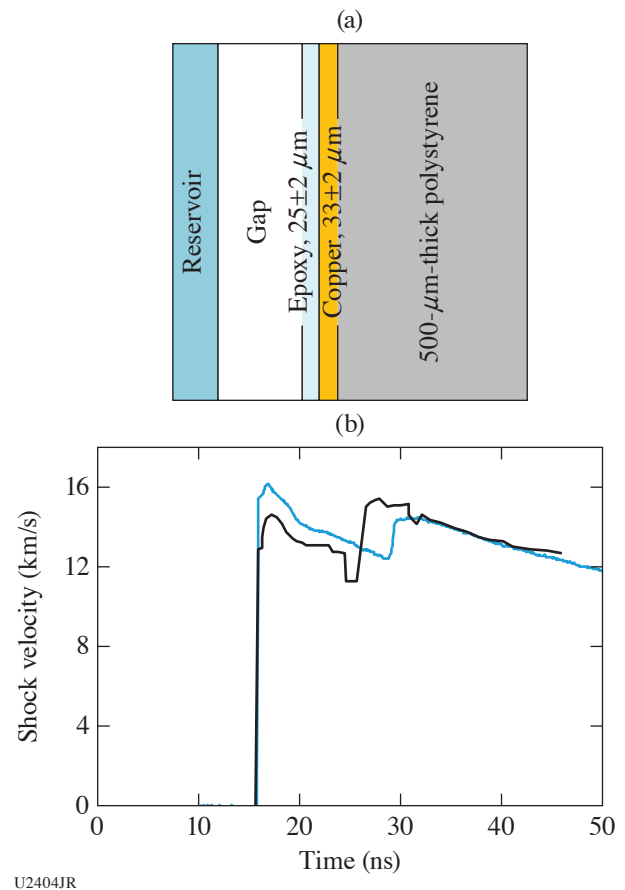
Considerable experimental and simulation sensitivity analysis led to a hypothesis that reverberations interact with the incoming drive plasma column and lead to complicated shock–release–reshock paths that are not well represented by the existing equations of state.

The FY18 campaign made use of drive analog targets and the ASBO diagnostic to measure the magnitude and timing of reverberation features expected from the simulations to assess the sensitivity of the experiment to various EOS assumptions.

Multiple target designs were used to mitigate risk associated with uncertainties in the behavior of target materials under shock loading.

The primary result of the single day of experiments is shown in Fig. 156.128. The expectation was for a reverberation to appear at about 25 ns; this reverberation is associated with the RT growth that occurs at about 30 ns in the simulations shown in Fig. 156.127. The actual reverberation appears about 3 to 4 ns later and is somewhat smaller than expected. Other shots confirmed this observation and provided additional observations that will help in characterizing dependency on sample dimensions and drive strength.

Based on this observation we believe we understand the origin of the disagreement between experimentally measured and simulated RT growth in liquid copper. Future work will incorporate these results into modeling the RT growth and



U2404JR

Figure 156.128  
(a) Target used for shot 28641. (b) Comparison of pre-shot simulated (black line) and experimental (blue line) shock velocity. The measured reverberation arrives about 3 ns later than was simulated.

re-assess the ability of the simulations to accurately represent the observed growth.

**Development of Pressure–Time Pulse Shaping in Ramp-Compression Experiments**

**Using Graded Density Additively Manufactured Foams**

Principal Investigator: R. Smith

Co-investigators: S. Ali, J. Oakdale, J. Biener, H.-S. Park, S. Prisbrey, and P. Amendt

In support of Material Strength experiments on the NIF, the goal of these experiments is to shape the pressure profile in a piston-driven, ramp-compression platform<sup>57</sup> by incorporating an additive manufactured foam layer (AM foam) into the sample design [see Fig. 156.129(a)]. The 3-D–printed foams are characterized as follows:<sup>84</sup> The  $100 \times 100 \times 16\text{-}\mu\text{m}^3$  log pile blocks composed of individually printed lines are stitched together to form layers that are  $1.7 \text{ mm}^2$  in diameter. Seven  $16\text{-}\mu\text{m}^3$  layers are then stacked on top of one another to arrive at cylindrical “AM foams” that are  $1.7 \text{ mm}^2$  in diameter and 112 mm tall (Ref. 84). These foams are glued onto a  $25\text{-}\mu\text{m}$  Br +  $120\text{-}\mu\text{m}$  12% Br/CH assembly [Fig. 156.129(a)]. For some

shots the overall thickness was varied. Following the prior ramp-compression design,<sup>57</sup> 15 beams of the OMEGA laser with 300 J in 2 ns launch a ramp-compression wave into an Al/LiF sample [Fig. 156.129(a)]. Throughout these campaigns, different shots have varied the thickness and density of the 3-D–printed foam with the goal of optimizing the temporal ramp profile. Changing the laser energy causes the pressure in the Al sample to vary. In the example velocity profiles in Fig. 156.129(b), as determined by VISAR, the rise time of the compression wave increases several fold as a result of the inclusion of the AM foam layer. Further modification of the compression-wave pulse shape is possible by varying the thickness of the AM foam layer [Fig. 156.129(c)]. Here, a velocity plateau is evident but diminishes with decreasing AM foam thickness.

**Rayleigh–Taylor Growth Measurements in Depleted Uranium**

Principal Investigators: J. M. McNaney, R. Smith, and H.-S. Park

This campaign is designed to develop a new ramp drive by laser-pulse shaping that can maintain the depleted uranium

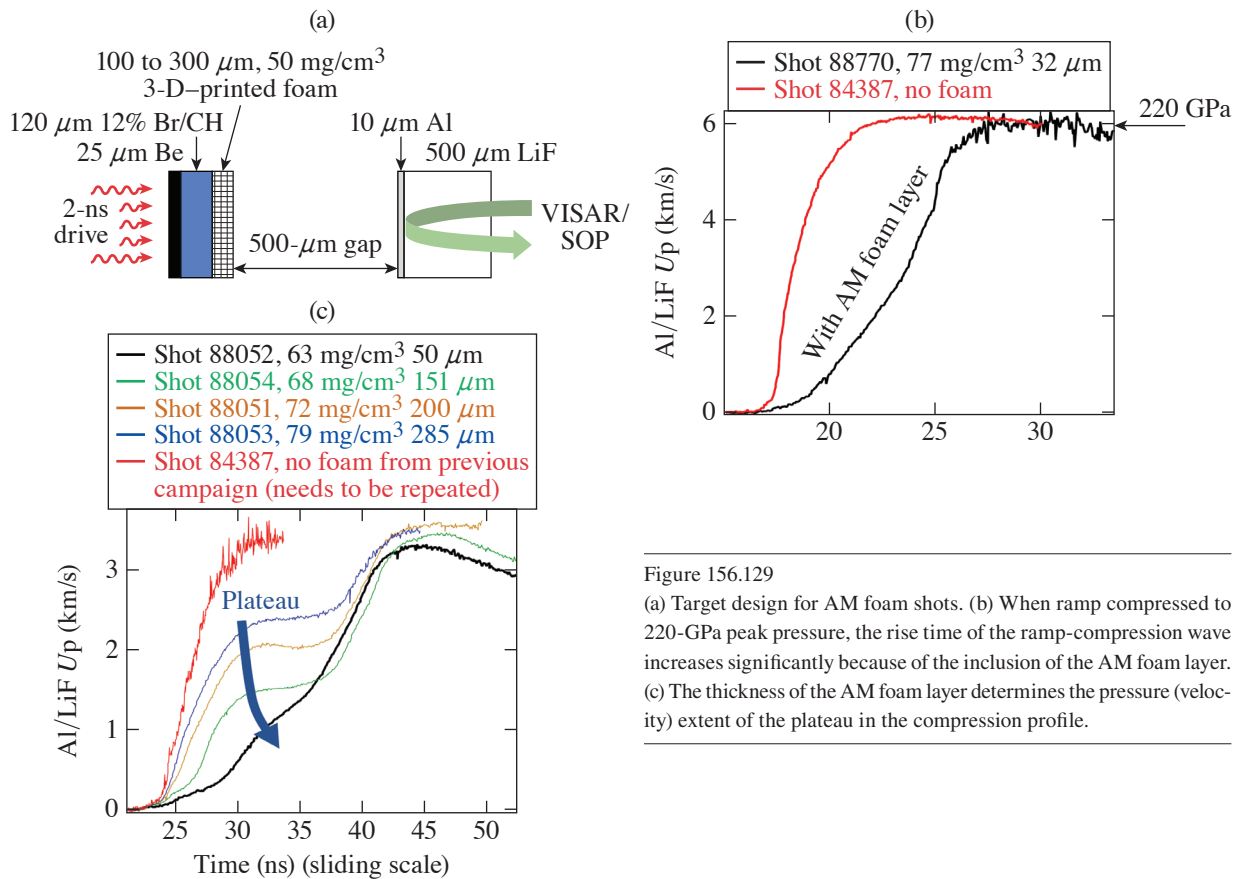


Figure 156.129 (a) Target design for AM foam shots. (b) When ramp compressed to 220-GPa peak pressure, the rise time of the ramp-compression wave increases significantly because of the inclusion of the AM foam layer. (c) The thickness of the AM foam layer determines the pressure (velocity) extent of the plateau in the compression profile.

U2405JR

(DU) sample in solid state while driving to 1- to 2-Mbar peak pressure. If successful, this drive will be used to measure DU strength by measuring the ripple growth amount from Rayleigh–Taylor instability. A 30-ns-long pulse shape was designed by stitching three 10-ns-long beams, as shown in Fig. 156.130(a), and the drive is measured with the VISAR diagnostic. The VISAR targets consist of an ablator (Be), a witness plate (Ta or Cu), and a LiF window. The first campaign used a variety of targets with different styles of witness samples. The VISAR produced meaningful data as shown in Figs. 156.130(b) and 156.130(c). The raw fringe traces are shown in Fig. 156.130(b), and the analysis of this shot is shown in Fig. 156.130(c). Also shown is the 1-D *HYADES* simulation. The agreement is remarkable except for a small amount of timing shift. During the first of two shot days in FY18, however, the shot-to-shot repeatability was not very good, mainly because of nonuniform glue thicknesses and a nonplanar target component. The second day attempted to fix this issue. Glue usage was removed by depositing rather than adhering the Cu witness sample, and planarity was improved by polishing the target component. The repeatability was greatly improved, and the campaign returned data to understand the effect of composite pulse shaping through beam “stitching.” The next step is to apply this drive on rippled targets and measure growth factors.

**Modulation Transfer Function Accuracy for Rayleigh–Taylor Growth Experiments**

Principal Investigator: E. Gumbrell

Co-investigators: H.-S. Park, C. Huntington, A. Krygier, and J. M. McNaney

This campaign aimed to quantify and reduce the systematic error induced by uncertainties in the modulation transfer function (MTF) used to analyze ripple growth for the material strength campaign. The MTF is a measure of spatial resolution in an optical imaging system and mathematically is the Fourier transformation of the line-spread function. The strength campaign radiographs the ripple growth and corrects for the MTF as measured by an x-ray knife-edge included with the target. The uncertainty of this method arises mainly from uncertainty in the spatial profile of the x-ray backlighter, which very often consists of two sources—one sharp spot that achieves high resolution and a second, broader spot from the transmission of high-energy x rays through the thin section of the collimator. This campaign obtained data on the MTF using large-amplitude undriven ripples in a single shot. The systematic error was determined by comparing the analyses between the ripple-amplitude measurement using the steps and the MTF, and the known ripple amplitudes from the target metrology. High-quality radiography images were obtained as shown in Fig. 156.131(a) from this

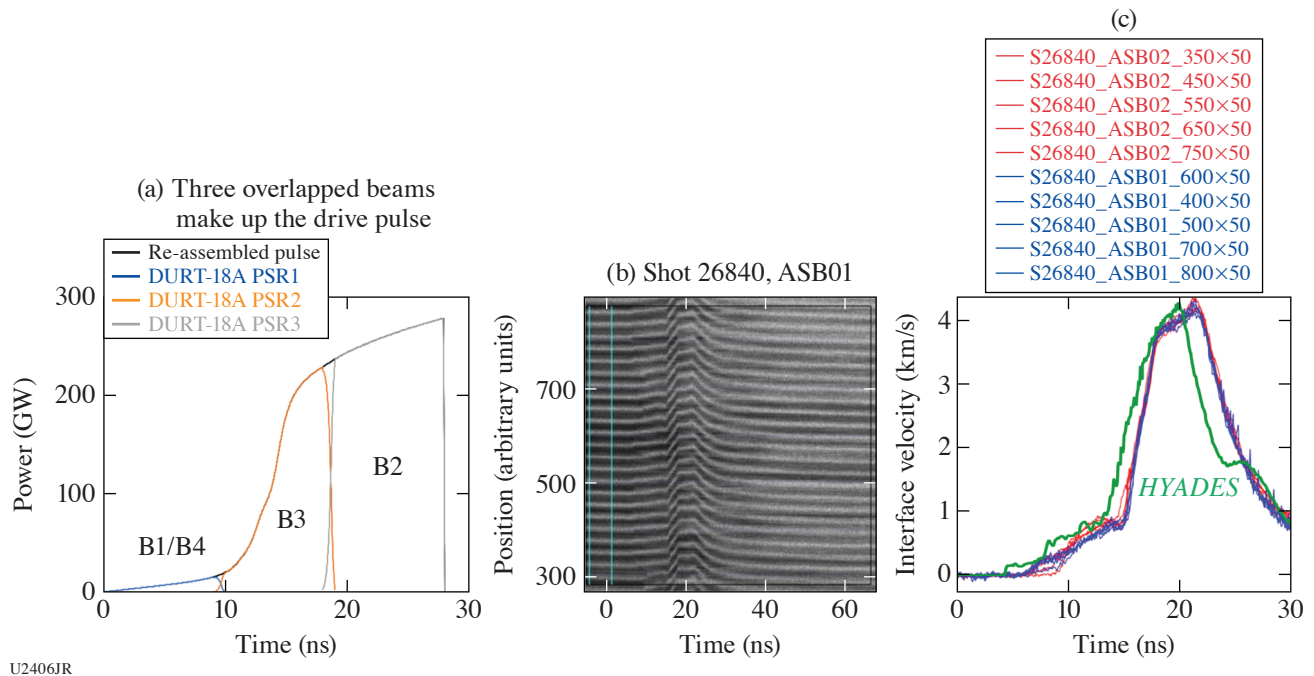


Figure 156.130 (a) Three-beam “stitched” pulse shape to create a directly driven ramp drive for the strength campaign. (b) Raw VISAR data using the designed pulse shape. (c) Analyzed VISAR data and comparison with a 1-D *HYADES* simulation.

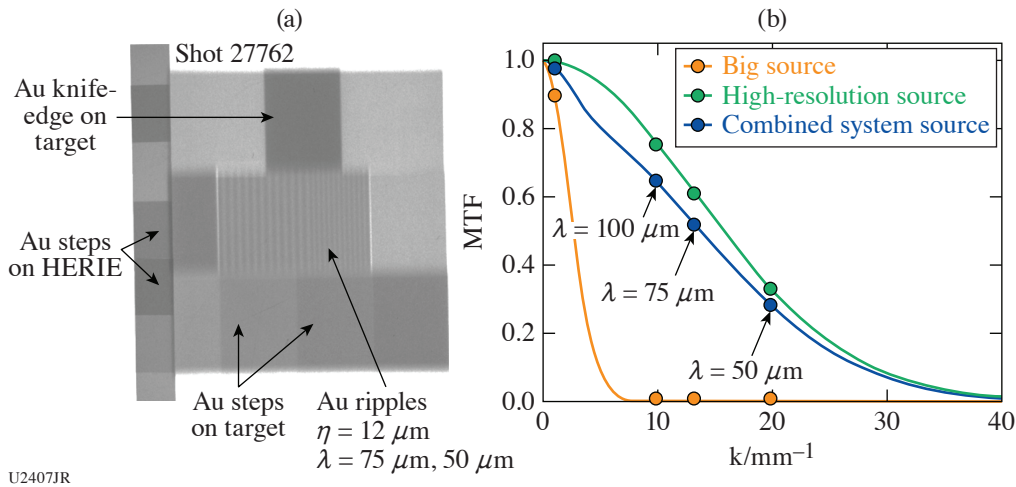


Figure 156.131

(a) Radiography of known large-amplitude ripples and x-ray knife edge (shot 27762). (b) MTF derived from (a) showing inferred contributions from two backlighter sources.

campaign. The analysis of the MTF from this image is shown in Fig. 156.131(b), including the high-resolution source (green curve), the lower-resolution source (orange curve), and the combined system MTF derived from the convolution of these sources (blue curve). Using this MTF and comparing with the known ripple amplitudes leads to the conclusion that the systematic error of the ripple-growth-factor analysis is less than 10%. The results of this campaign were published in Review of Scientific Instruments.<sup>85</sup>

#### 4. National Security Applications

##### *SolarCellESD: Solar Cell Electrostatic Discharge Experiments*

Principal Investigator: K. Widmann

Co-investigators: P. Jenkins (NRL); S. Seiler and H. Jiles (DTRA); and P. Poole and B. Blue (LLNL)

The SolarCellESD Campaign seeks to determine experimentally whether prompt x rays can induce failure modes in solar arrays that are not accounted for by simply testing the individual solar cells alone because the voltage difference between neighboring cells can be hundreds of volts, depending on the overall layout of the array. These experiments at Omega have been fielding the smallest possible array, i.e.,  $2 \times 1$  cells with electronic controls that allow the user to dial in a voltage difference (bias voltage) between the two cells and thereby study the failure modes as a function of incident x-ray flux and bias voltage, respectively. The FY18 campaign continued using the partial electromagnetic-interference (EMI) shield previ-

ously tested during the FY17 campaign and added the option of installing permanent magnets in the front of the enclosure (Fig. 156.132) to deflect charged particles, mainly electrons, away from the solar cell samples.

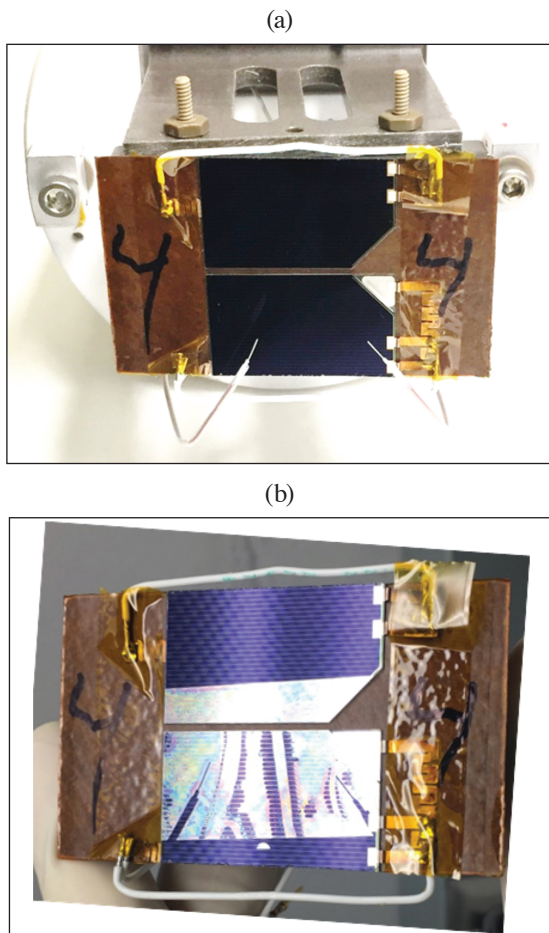


Figure 156.132

EMI enclosure with permanent magnets installed behind the x-ray aperture. The resulting magnetic-field strength is 300 gauss at the center and over 2000 gauss near the edge of the aperture.

The laser-driven x-ray source of choice for these solar cell experiments remains the small gold halfraun ( $600 \mu\text{m}$  diameter,  $600 \mu\text{m}$  long) but without the pinhole on the closed end. After having demonstrated x-ray-induced sustained arcing for the first time during the FY17 campaign, the conditions indicated that it was not necessary to keep the very low flux

option for these x-ray sources. One additional variation in the experimental configuration for the FY18 shots was the view angle between the x-ray source and the solar cell samples. The FY18 shots tested view angles of approximately 35°, 45°, 60°, and 70°, respectively. Post-shot inspections of the solar cell samples indicated a strong dependence of debris on the view angle. Especially at 70°, significant changes are seen in the surface conditions of the area that was exposed to the x rays through the x-ray aperture. Figure 156.133 shows a before and after comparison of one of these solar cell sample coupons, in which one can clearly see the shadow cast onto the surface by the two Langmuir probe tips that are in front of the solar cells. On the contrary, shots where the view angle was 35° and 45° had no visible alteration of the surface of the solar cells.



U2409JR

Figure 156.133

(a) Solar-cell array with two Langmuir probes before a shot. (b) The same solar cell coupon after the shot shows significant amount of debris in the area that is exposed to the x rays. The shadow of the Langmuir probe wire tips can be seen in the bottom left and bottom right corners of the “coated” area of the solar cells.

The FY18 campaign was able to further constrain the parameter space with respect to x-ray flux and bias voltage that causes x-ray-induced, sustained arcing between the solar cells. By comparing the results obtained with and without the magnetic field at the x-ray aperture, it was also confirmed that the impact of charged particles from the laser-generated plasma is negligible compared to the x-ray-induced effects.

### ***Plasma Instability Control to Generate a High-Energy Bremsstrahlung X-Ray Source***

Principal Investigator: P. L. Poole

Co-investigators: R. Kirkwood, S. C. Wilks, M. May, K. Widmann, and B. E. Blue

FY18 continued a campaign to develop a high-fluence x-ray source in the 30- to 100-keV range by optimizing plasma instabilities. High-fluence sources at lower energies are currently used for materials effects studies in extreme environments, but no good source exists for >30-keV x rays. This project aims to enhance laser conversion to plasma instabilities like stimulated Raman scattering (SRS) and two-plasmon decay (TPD), which accelerate electrons in plasma waves that will convert to high-energy x rays via bremsstrahlung in the high-Z hohlraum wall.

Two half-day campaigns during FY18 explored the effects of different hohlraum fills and the resulting plasma environment on backscattered light and hard x-ray emission. A critical goal was the ability to control which plasma instability was dominant in the plasma between SRS and TPD, and which could be optimized to produce the strongest hot-electron spectrum. Figure 156.134 summarizes this effort, showing the SRS backscatter signal time resolved and compared to the hard x-ray signal: hohlraums with inner CH lining were dominated by the SRS interaction and emitted the hardest x rays late in the drive pulse. The foam-filled targets instead produced conditions optimum for TPD, generating all energies of x rays early in time before any SRS backscatter initiated. Additionally, C<sub>5</sub>H<sub>12</sub> gas fills were studied on the same hohlraum designs (demonstrating low hard x-ray yield but providing a critical comparison of the CH-lined and foam-filled results to historical data), as well as a range of foam densities to investigate scaling.

The results from the OMEGA campaign were used to design a complementary NIF shot day in Q2 FY18, which achieved the same hard x-ray signal as the previous campaign but used only 40% of that laser energy. The campaign is now focused on using subsequent OMEGA days to optimize plasma conditions for SRS with more unique targets, including foam fills

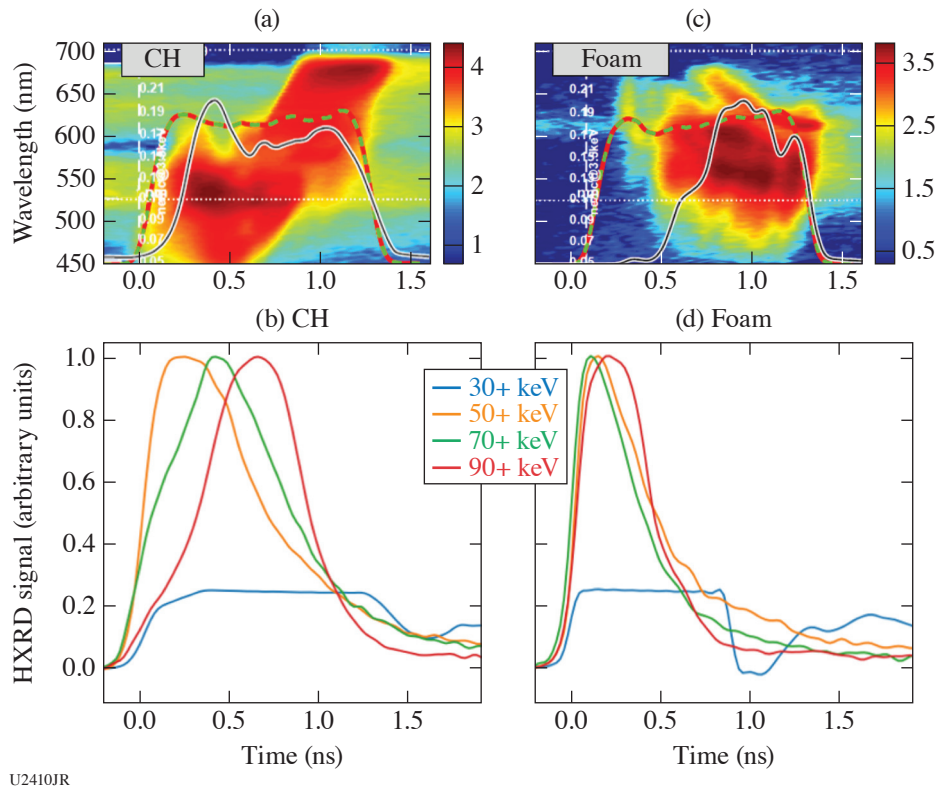


Figure 156.134

(a) Time-resolved SRS backscatter data and (b) hard x-ray signal for CH-filled hohlraum increased x-ray emission at later times, and higher plasma densities. By contrast, the foam-filled targets show only (c) late-time SRS backscatter and (d) a corresponding drop in x-ray signal at those times.

with density gradients, but the initial success has led the next planned NIF shots to include samples to be studied under this unique hard x-ray environment, despite still being in the source development phase. As such, these FY18 results have reached the cusp of a new x-ray source that will represent a large capability increase for national security applications and related materials under extreme conditions studies, with the additional benefit of broadening the understanding of plasma instability control for fusion and other applications.

#### ***Enhancing Multi-KeV Line Radiation from Laser-Driven Nonequilibrium Plasmas Through the Application of External Magnetic Fields***

Principal Investigator: G. E. Kemp

Co-investigators: P. L. Poole, D. A. Mariscal, G. F. Swadling, J. D. Colvin, K. B. Fournier, M. J. May, and B. E. Blue (LLNL); A. Dasgupta, A. L. Velikovich, and J. Giuliani (NRL); and C. K. Li and A. Birkel (MIT)

A recent LLNL Laboratory Directed Research and Development effort (17-ERD-027) has been studying the influence of externally applied magnetic fields on laser-driven x-ray

sources—like those typically used for high-fluence radiography or backlighters—with the ultimate goal of improving multi-keV x-ray conversion efficiency through thermal transport inhibition. This series of shots was designed to test and qualify a platform for fielding externally generated magnetic fields on previously fielded x-ray sources on the OMEGA laser. This platform is intended to collect data in the >10-T magnetic-field regime, where currently very little data exist for such high-Z, non-LTE (local thermodynamic equilibrium), magnetized plasma conditions. The collected data will be used for constraining thermal transport inhibition and magnetohydrodynamics models currently used in the multi-physics radiation-hydrodynamic code *HYDRA*.

The experimental configuration is illustrated in Fig. 156.135. Thin-walled, cylindrical Kr gas pipes (1.5 atm), Cu foams (~10 mg/cm<sup>3</sup>), and Cu hohlraums were driven by 20 kJ of laser energy in a 1-ns pulse (40 beams) as typical sources of K-shell line radiation. A total of 12 shots were taken, half of which had externally imposed B fields. The pulsed-power magneto-inertial fusion electrical discharge system (MIFEDS) was used to provide axial external B-field strengths of roughly 13 T. Quantifying changes in x-ray emission with increasing external

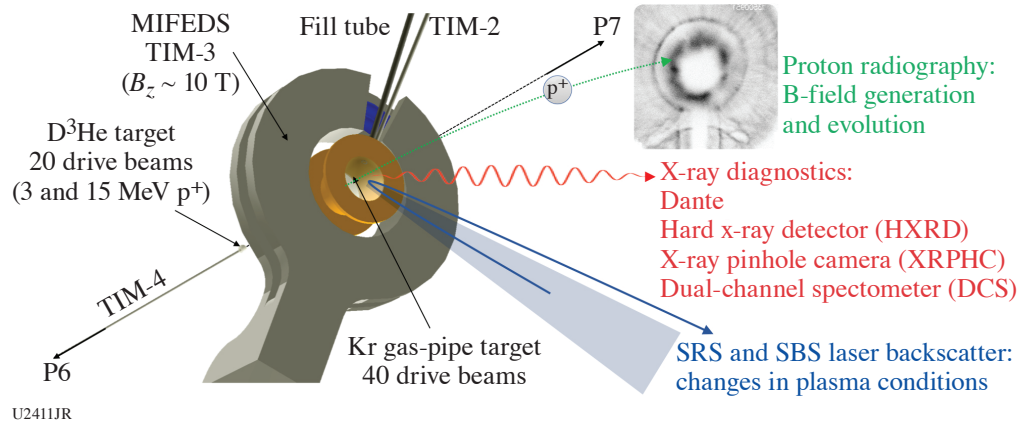


Figure 156.135

Experimental configuration for MagXRSA-18A. X-ray emission, laser backscatter, and proton radiography data were simultaneously obtained to quantify the evolution and influence of external B fields in these interactions.

B-field strength was the primary goal of the shots, recorded with Dante (0 to 20 keV), hard x-ray detectors (20 to 500 keV), pinhole cameras ( $>2$  keV), and the dual-channel spectrometer (11 to 45 keV). Secondary diagnostics included proton radiography and stimulated Raman/Brillouin laser backscatter. A  $D^3He$  backlighter capsule (driven by the remaining 20 beams) provided a source of 3- and 15-MeV protons. Analysis is ongoing, but initial results suggest 10% to 30% enhancements in multi-keV Kr emission when the B field is present, consistent with the pre-shot modeling,<sup>86</sup> with only modest changes in laser backscatter. Neither the Cu foams nor cavities showed significant changes in x-ray emission.

Preliminary results from this campaign were presented at the 2018 HEART Technical Interchange Meeting in Tucson, AZ, and are being used to further optimize the platform to make more measurements in Q1 FY19 using a dual-MIFEDS configuration, with expected magnetic fields in excess of 20 T.

## 5. Plasma Properties

### *Investigation of High-Velocity Plasma Flow into a Low-Density Magnetized Background Plasma Region*

#### **Background Plasma Region**

Principal Investigator: B. B. Pollock

Co-investigators: G. Swadling, J. S. Ross, and H.-S. Park

This “Debris Plasma” Campaign continued the Magnetized Collisionless Shock–Weapons Effect Campaign from previous years. The goal for this series of experiments is to quantify the interaction of high-velocity plasma flow into a region containing a low-density, weakly magnetized background plasma. This is

relevant for understanding the effect of high-altitude detonations and the resulting interaction with plasma in the atmosphere. The intent is to compare with both fluid and PIC modeling to determine if a less computationally intensive fluid code can capture enough of the relevant physics to reproduce the data, or if kinetic effects like collisions are required in the simulations (pushing toward a PIC treatment). The field is supplied by the LLE MIFEDS, which delivers 4 to 8 T at the interaction region of the experiments (depending upon the specific geometry of the MIFEDS coils). The plasma flows originate from two separate foil targets, one of which is mounted to the MIFEDS structure (in either, the position occupied by the green foil or the red foil in Fig. 156.91); the second foil is independently mounted outside the MIFEDS. The foil material compositions, spacing, and plasma arrival time to the interaction region can be varied for each shot, as can be the laser drive onto each foil.

The interaction region of the two flows is simultaneously probed with  $2\omega$  Thomson-scattering diagnostic and protons from the implosion of a  $D^3He$ -filled capsule. Initial measurements of the electron density and temperature from the Thomson-scattering diagnostic do not indicate a strong dependence on the strength or direction of the background magnetic field. The proton deflectometry data do show structural differences in the measured proton distribution with and without the field, but further modeling and simulations are needed in order to quantify these differences. During these experiments the field of view of the proton-probed region has been enlarged significantly by reducing the magnification from  $\sim 30$  (as in the beginning of the series) to  $\sim 10$ . This was achieved by inserting the CR-39 detector to  $\sim 11$  cm from the target chamber’s center and allows the entire region between the MIFEDS coils to be visible in the proton data.

**Measurement of Gold Thermal Transport and M-Shell Emission Using a Buried-Layer Platform**

Principal Investigator: E. V. Marley  
 Co-investigators: L. C. Jarrott, M. B. Schneider, G. E. Kemp, M. E. Foord, R. F. Heeter, D. A. Liedahl, K. Widmann, C. W. Mauche, G. V. Brown, and J. Emig

This campaign was designed to measure the thermal transport through gold layers as well as measure the emitted M-shell gold spectra from a well characterized and uniform plasma for comparison to atomic kinetic models. The buried-layer target geometry used for this experiment is capable of generating plasmas with an electron temperature of  $\sim 2$  keV at electron densities of  $10^{21}$  electrons per cubic centimeter. These are also the conditions found inside gold hohlraums used on experiments on the NIF, providing a stable laboratory setting for radiation transport and atomic kinetic studies.

Planar, buried-layer targets were illuminated equally on both sides (Fig. 156.136) to heat the sample. Two sample types were used during the campaign: The first was a  $700\text{-\AA}$ -thick Au/V mixture designed to burn through completely before the end of the laser pulse, providing uniform plasma conditions to measure the M-shell emission of the gold. The second sample

type was composed of three layers: the outer two layers were  $500\text{-\AA}$ -thick Au while the final central layer was  $600\text{-\AA}$ -thick Sc. These targets were designed to measure the thermal transport of Au using the K-shell emission of the Sc. Both sample types were buried between two  $5\text{-}\mu\text{m}$ -thick layers of Be, which acted as an inertial tamp to slow the expansion of the sample.

Time-resolved 2-D images of the target's x-ray emission, viewed both face on and side on, were recorded using pinhole cameras coupled to framing cameras [see Fig. 156.136(b)]. The K-shell spectra from the Sc and V were used to determine the electron temperature of the plasma. The time-resolved spectra were recorded using a crystal spectrometer coupled to a framing camera as well as a crystal spectrometer coupled to an x-ray streak camera. Two crystal spectrometers were used to record the full range of the Au M-shell emission, also time resolved. All of the framing cameras used, those for imaging as well as those for spectroscopy, were co-timed so the plasma conditions could be determined for the measured Au M-shell emission.

Two different pulse shapes were used to determine the most efficient shape for coupling laser energy into the buried-layer target: a 3-ns square pulse and a 3-ns square pulse with a 100-ps picket arriving 1 ns before the main pulse. A complete (all six diagnostics, correctly timed) set of data was recorded for both target types, using both pulse shapes during the campaign at temperatures  $\sim 2$  keV.

6. Hydrodynamics

**Experiments of Single-Mode Rayleigh–Taylor Growth in the Late Nonlinear Stage and Dependence on Density Contrast**

Principal Investigator: L. Elgin (U. Michigan)  
 Co-investigators: C. Huntington (LLNL) and T. Handy, G. Malamud, S. R. Klein, M. R. Trantham, R. P. Drake, A. Shimony, and C. C. Kuranz (University of Michigan)

This campaign completed four shot days in FY17–FY18 to observe the evolution of single-mode Rayleigh–Taylor instability (RTI) growth from the early nonlinear stage to the transition to turbulent mixing, in both low- and high-Atwood-number systems (Fig. 156.137). Potential flow models of classical RTI growth predict that spikes and bubbles will reach a terminal velocity. When the density contrast of the two fluids is small, numerical simulations show an unexpected re-acceleration of RTI growth in the late nonlinear stage.<sup>87</sup> Prior experimental studies of single-mode RTI growth have not created the conditions necessary to observe or refute the behavior in question,

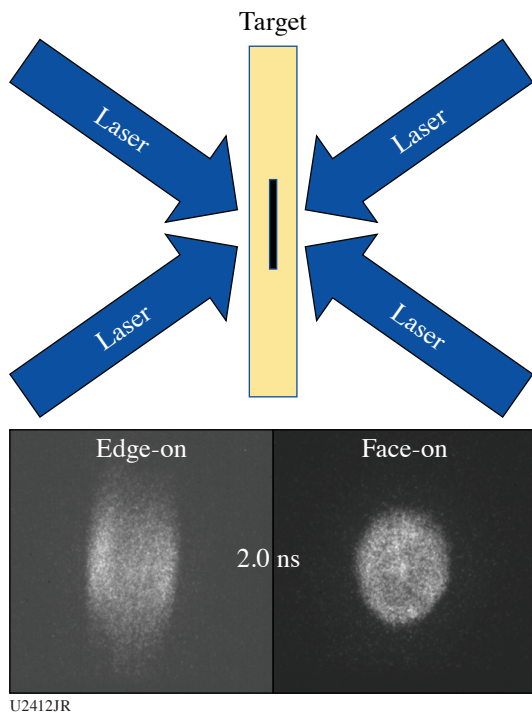
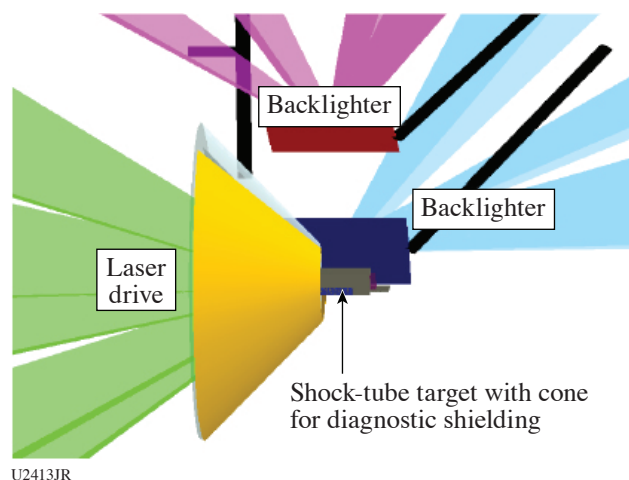


Figure 156.136  
 Experimental configuration and pinhole images of the emission area at 2 ns of shot 89435.



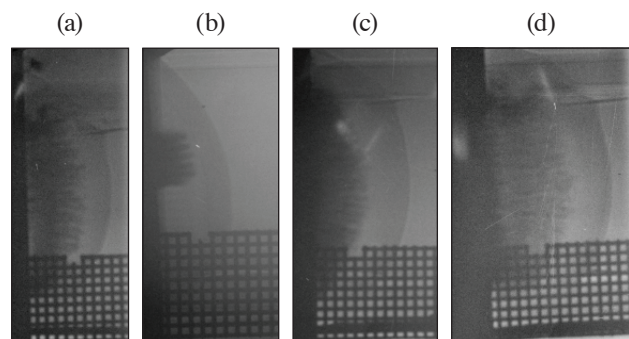
U2413JR

Figure 156.137  
Experimental configuration.

which requires large aspect ratios of the spike and bubble amplitudes to the perturbation wavelength ( $1 \leq h/\lambda \leq 3$ ).

In these experiments, a planar blast wave drives RTI growth at an embedded interface seeded with a single-mode pattern. Target variations include 2-D and 3-D perturbations and post-shock Atwood numbers of 0.17 and 0.6. A series of x-ray radiographs along dual orthogonal axes captures the evolution of RTI growth. FY17 shots successfully demonstrated dual-axis radiography capabilities with  $\sim 10\text{-}\mu\text{m}$  spatial resolution and observed RTI growth in high-Atwood ( $A = 0.6$ ) targets with 3-D  $\lambda = 40\text{-}\mu\text{m}$  spikes and bubbles (Fig. 156.138). FY18 shots obtained data in low-Atwood ( $A = 0.17$ ) targets with 2-D and 3-D perturbations and extended the high-Atwood data sets. Results from the FY17 experiments were presented in several venues,<sup>88</sup> and FY18 results will be presented at APS DPP 2018 and thereafter.

This work funded by Lawrence Livermore National Laboratory under subcontract B614207.



U2414JR

Figure 156.138  
Radiography data of 3-D  $\lambda = 40\text{-}\mu\text{m}$ , low- $A$  targets: (a) RID 90385 at 20 ns; (b) RID 90387 at 20 ns; (c) RID 90381 at 25 ns; and (d) RID 90382 at 30 ns.

### Development of Novel Diagnostic and Target-Fabrication Techniques for X-Ray Imaging of Rayleigh–Taylor Instabilities

Principal Investigator: C. M. Huntington

Co-investigators: S. Nagel, K. Raman, J. Bender, and S. Prisbrey

“Foam bubbles” is an ongoing effort to improve target and diagnostic methods for imaging of planar hydrodynamic interfaces. In these experiments a hohlraum is used to drive a plastic ablator package, launching a shock wave into the plastic. The high-density plastic ablator ( $1.43\text{ g/cm}^3$ ) is paired with a low-density foam [ $80\text{-mg/cm}^3$  carbon resorcinol foam (CRF)], creating an interface that is unstable after the passage of the blast wave. The primary diagnostic for this campaign has been point-projection x-ray radiography, and the targets have been optimized for contrast at the 9-keV  $\text{He}\alpha$  line from zinc. Previous shot days have used this configuration to develop foams with novel x-ray transmission properties and to maximize shock planarity across the interface.

There were two principal goals of the September 2018 shot day. A range of targets were prepared with different interface initial conditions, including single-mode (sine wave), multi-mode (roughened), and flat initial interfaces, to quantify the relative growth of different initial conditions. Additionally, several shots were used to image the system with the Kirkpatrick–Baez (KB) “fixed” diagnostic, which boasts a higher resolution than point-projection backlighting, although at a lower energy. Excellent data were collected in the point-projection data set [Fig. 156.139(a)], capturing high-resolution data for all target types of interest. The first images of a hydrodynamically unstable planar interface were also recorded with the KB diagnostic [Fig. 156.139(b)], demonstrating the viability of the technique. With targets optimized for the KB diagnostic (thinner, with higher x-ray transmission at lower energy, to improve data signal-to-noise), it is anticipated that this instrument will be able to record high-resolution images of hydrodynamic instabilities in future Foam Bubbles Campaigns.

### Mix-Width Measurements in Metallic Foams

Principal Investigator: D. A. Martinez

Co-investigators: S. F. Khan, M. Rubery, T. Dittrich, S. G. Glendinning, T. Woods, J. Ward, M. Arend, R. Wallace, and T. Baumann

This experiment series was designed to determine which foam-manufacturing technique for  $0.9\text{-g/cm}^3$  Cu foam produces the smallest mix width for use in hydrodynamic experiments on the NIF. The two Cu foam techniques have a different structure

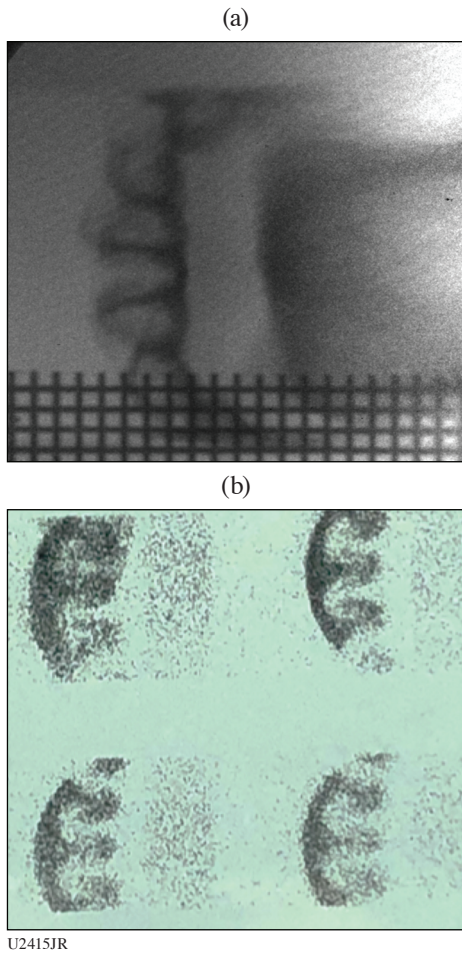


Figure 156.139  
 (a) Example image from the point-projection x-ray radiography data set. In this image the unstable interface is being driven from right to left, and dark Rayleigh–Taylor spikes can be seen penetrating into lighter x-ray transmissive foam. (b) Example image from the KB, with clear evidence of RT spikes, which are light colored in this film negative photograph.

but a primary pore size of  $\sim 1 \mu\text{m}$ . In addition, the experiment assessed a  $\text{Ta}_2\text{O}_5$  foam at  $0.9 \text{ g/cm}^3$  to determine if a smaller cell size (estimated between 10 and 100 nm) will produce a smaller mix width compared to the Cu foam.

This joint experiment used a half-hohlraum connected to a shock tube. The shock tube consisted of a polyethylene ablator, a metallic foam sample of either Cu or  $\text{Ta}_2\text{O}_5$  at  $0.9 \text{ g/cm}^3$ , and followed by a  $50\text{-mg/cm}^3$  CRF foam reservoir. The hohlraum was driven using 12 beams with a 1-ns square pulse to produce a peak radiation temperature of 200 eV. The resulting blast wave causes the metallic foam/reservoir interface to become unstable, resulting in RT instability growth. The shock tube was imaged using a point-projection backlighter technique with a

$10\text{-}\mu\text{m}$ -diam Ag wire on a polystyrene substrate and illuminated with the OMEGA EP short-pulse beam. The interface mix was characterized by 90% to 10% transmission contour between the CRF–sample interface. Figure 156.140(a) shows a typical radiograph obtained during the experiment. The interface position was estimated using the Au washer around the shock tube [seen as the dark band on the bottom of Fig. 156.140(a)] and the position of the steepest gradient at the interface. The mix width was measured at 15 ns, 19 ns, and 23.5 ns for the Cu foam samples, and the  $\text{Ta}_2\text{O}_5$  was imaged at 23.5 ns from the start of the OMEGA laser drive. Figure 156.140(b) shows preliminary measurements of the mix width as a function of interface position. The AWE and GA copper foams produced similar mix widths, suggesting the mix width is insensitive to the micron-scale structure of the foam. Although only one data point was obtained for  $\text{Ta}_2\text{O}_5$ , the measured mix width follows

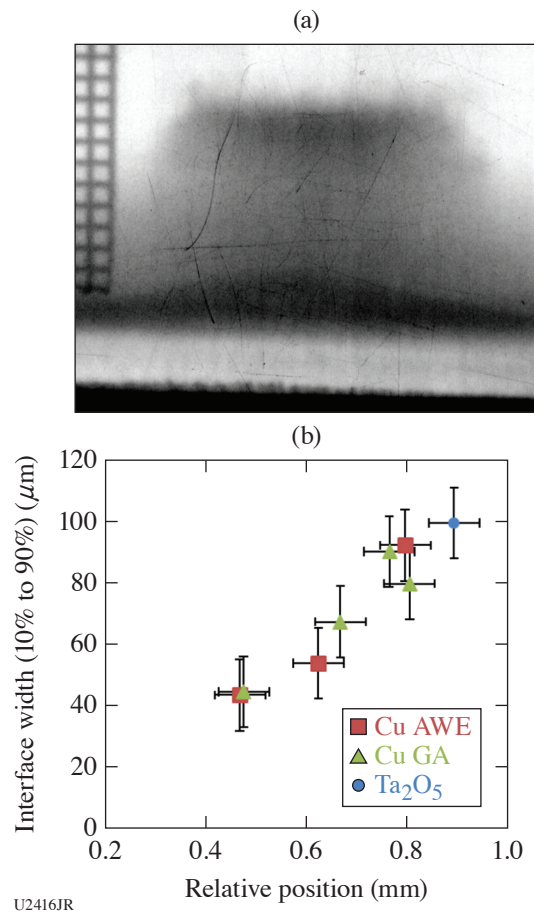


Figure 156.140  
 (a) Background-subtracted radiography of AWE Cu foam (shot 90839) at 23.5 ns. (b) Measured mix width as a function of interface position extracted from the radiographs.

along the Cu foam trend, which could also confirm that mix width is insensitive to the internal structure of the foam. Further work is required to confirm these observations.

**Carisbrook Radiography–Velocimetry Campaign**

Principal Investigators: M. Rubery and D. Martinez  
 Co-investigators: S. McAlpin, W. Garbett, G. Glendinning, T. Dittrich, and S. Prisbrey

A full shot day on the OMEGA Laser System in September 2018 continued the LLNL/AWE Carisbrook Campaign. This platform consists of a halfraum with a shock-tube package, driven using  $15 \times 500\text{-J}$  beams along the OMEGA H7 axis as shown in Fig. 156.141. The objective was to diagnose the evolution of a hohlraum-driven interface using simultaneous point-projection x-ray radiography and VISAR. The FY18 shots extended data from FY16 and FY17.

To generate the 7.8-keV (4.95-keV)  $\text{He}_\alpha$  point-projection x-ray source, a  $600\text{-}\mu\text{m}$  square nickel (titanium) microdot was driven to  $\sim 2 \times 10^{15} \text{ W/cm}^2$  using  $4 \times 400\text{-J}$ , 1-ns backlighter beams. The x-ray emission is projected through a  $20\text{-}\mu\text{m}$  Ta pinhole plate aligned along the shock tube and toward the TIM-6 cranked snout axis of  $\theta = 123.1$  and  $\phi = 172.76$ . Images

are recorded on film using a gated XRFC. Titanium was used instead of nickel on two shots to produce higher contrast in one region of the shock-tube package.

A quartz window, aluminum flash coating, and light shield cone on the rear of the target enable simultaneous VISAR measurements along the TIM-5 H14 axis. Figures 156.142(a) and 156.142(b) show good-quality VISAR streak-camera images from shots 91078 and 91085, respectively, with similar targets.

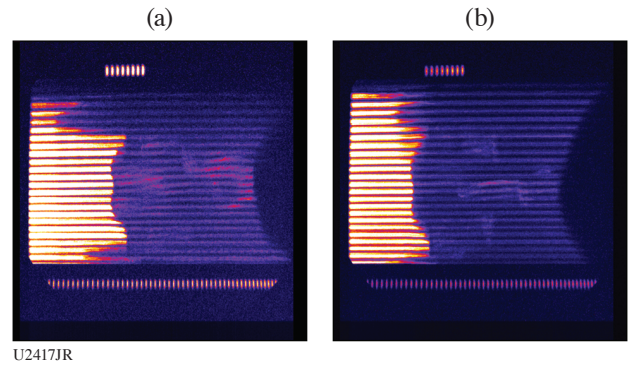


Figure 156.142  
 VISAR streaked images from OMEGA shots (a) 91078 and (b) 91085.

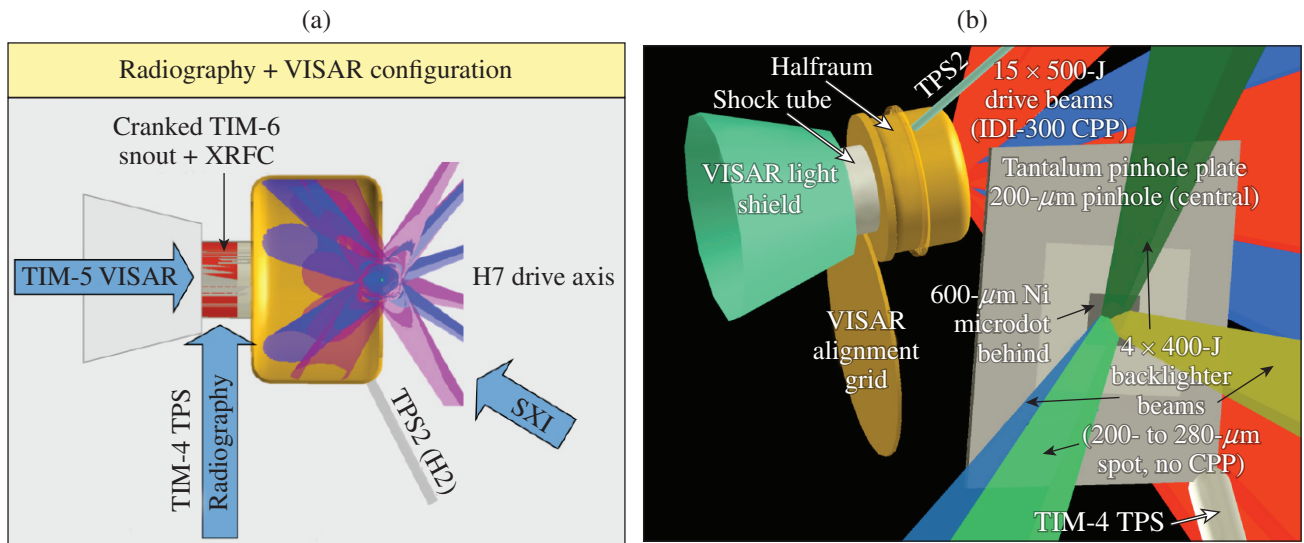


Figure 156.141  
 (a) Radiography + VISAR configuration overview. (b) VidRad isometric view of the experiment. BL: backlighter; CPP: continuous phase plate; DDS: disposable debris shield; SXI: soft x-ray imaging; TIM: ten-inch manipulator; TPS: Target Positioning System; VISAR: velocity interferometer for any reflector; XRFC: x-ray framnig camera.

Beams	# CPP's	CPP size	Pulse	Special/DDS
6 + 9 H7	15	IDI 300	1-ns square	500 J/beam
4x BL	Removed	280 $\mu\text{m}$	1-ns square	400 J/beam

U2295JR

The shot day returned excellent data on both primary diagnostics. The reproducibility is sufficient for the physics goals of the campaign. Initial analysis suggests the results are sufficient to close out the Carisbrook OMEGA effort and begin scaling up the platform to the NIF.

**Interaction of Dual High-Energy Backlighters**

Principal Investigator: S. F. Khan

Co-investigators: D. A. Martinez, S. C. Wilks, S. Prisbrey, S. G. Glendinning, D. T. Woods, and T. Dittrich

The objective of these OMEGA EP experiments is to study the interaction between dual wire backlighters, a configuration required for campaigns on the NIF. On the NIF, the wires will be used for point-projection radiography of an indirectly driven spherical implosion of a large target. With the large field of view (>3 mm), and the long time interval required between the two sources (>3 ns), some degradation of the second wire is expected because of the energy from the first wire. These OMEGA EP experiments used two 12.5- $\mu\text{m}$ -diam Ag wires with a separation of 4 mm. Each wire was illuminated by infrared 50-ps, 1-kJ short pulses. The time interval and order of wire illumination were varied from 0 to 7.5 ns.

It was found that the resolution obtained from the second hit wire was degraded from 19  $\mu\text{m}$  to 28  $\mu\text{m}$  with a time interval of 5 ns (Fig. 156.143). Fourth-harmonic shadowgraphs of the second wire before it was illuminated (Fig. 156.144) show an expanded material diameter of  $\sim 37 \mu\text{m}$  at 5 ns, larger than the resulting resolution from the wire. This could indicate that the emission distribution from the wire is nonuniform. Further analysis as well as simulations are ongoing. The results from this experiment will be used to design shielding for additional backlighter development experiments on the NIF.

**Measurements of Preheat and Instability Reduction with Tamping Layer Relevant to NIF Double-Shell Designs**

Principal Investigator: Y. Ping

Co-investigators: V. A. Smalyuk, P. Amendt, R. Tipton, S. Prisbrey, O. L. Landen, and F. Graziani

The goal of this campaign is to identify sources of preheat and reduction of instability growth using tamping layers under conditions relevant to the double-shell design on the NIF. The target consists of an ablator, CRF foam, and a Cu shell attached to a halfraum. Two half-days were fielded, with a total of 11 shots. For the preheat study, time-resolved side-on x-ray radiography was employed with the hard x-ray

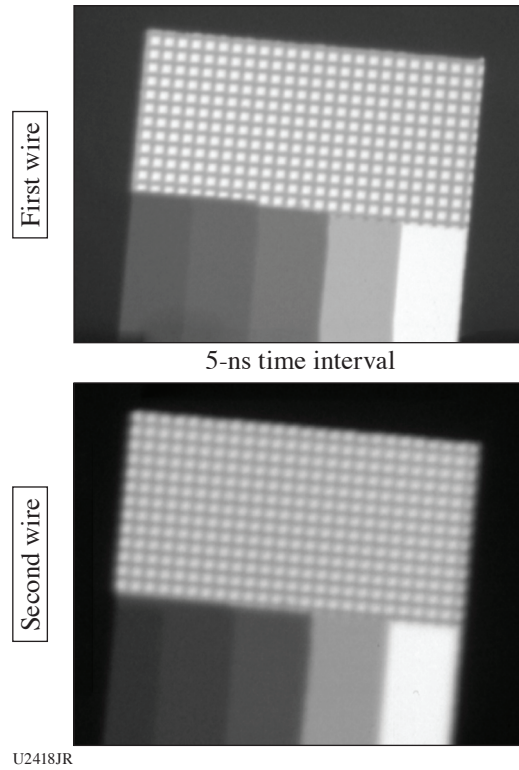


Figure 156.143  
Resolution grid x-ray radiographs from two sequential backlighters.

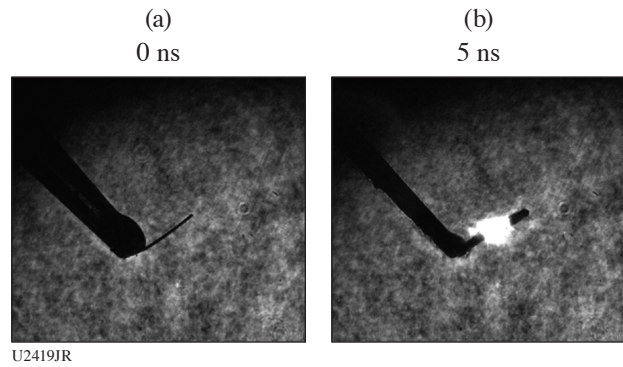


Figure 156.144  
Shadowgraphs of the second wire using the fourth-harmonic probe beam.

TCS (transmission crystal spectrometer). A clear correlation was observed between the preheat and gas fill as shown in Fig. 156.145, indicating that hard x rays generated by laser-plasma interaction in the halfraum contributed to the preheat. For instability-growth measurements, ripples with 30- $\mu\text{m}$  and 60- $\mu\text{m}$  periods and 1.5- $\mu\text{m}$  amplitude were imprinted on the Cu inner surface and face-on x-ray radiography with a fram-

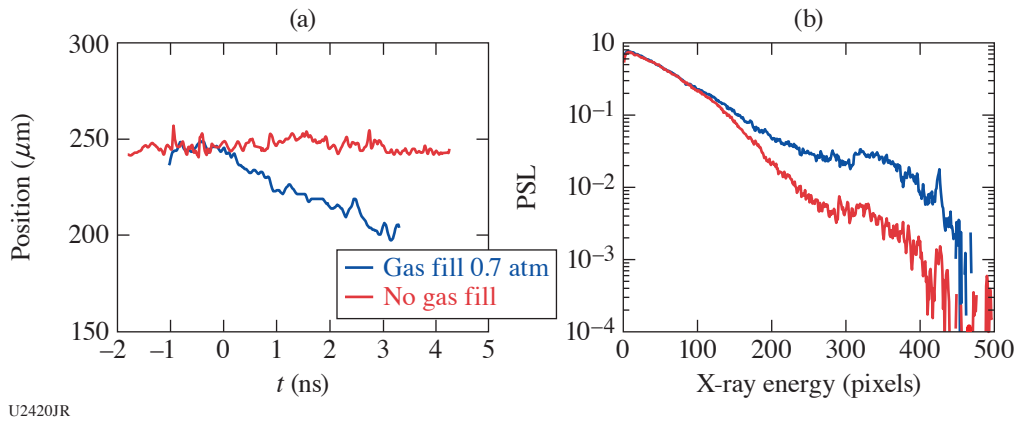


Figure 156.145  
(a) Position of Cu shell versus time before shock arrival. (b) Hard x-ray spectra with and without gas fill in the halfraum.

ing camera was employed to measure the ripple growth over time. Data analysis (Fig. 156.146) shows less growth with an Al tamping layer than without one.

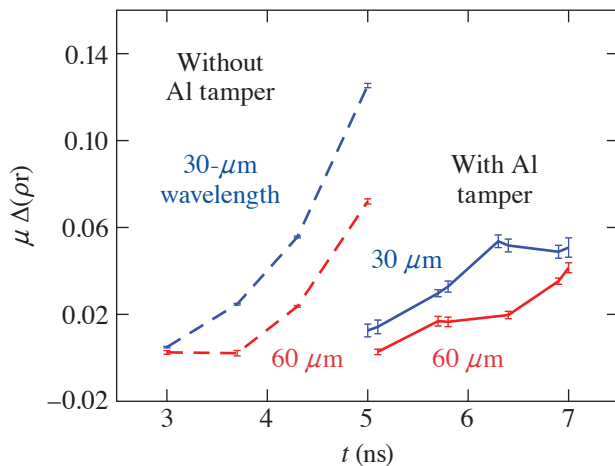


Figure 156.146  
Amplitude of ripples versus time with and without Al tamping layer.

### FY18 LANL Experimental Campaigns at the Omega Laser Facility

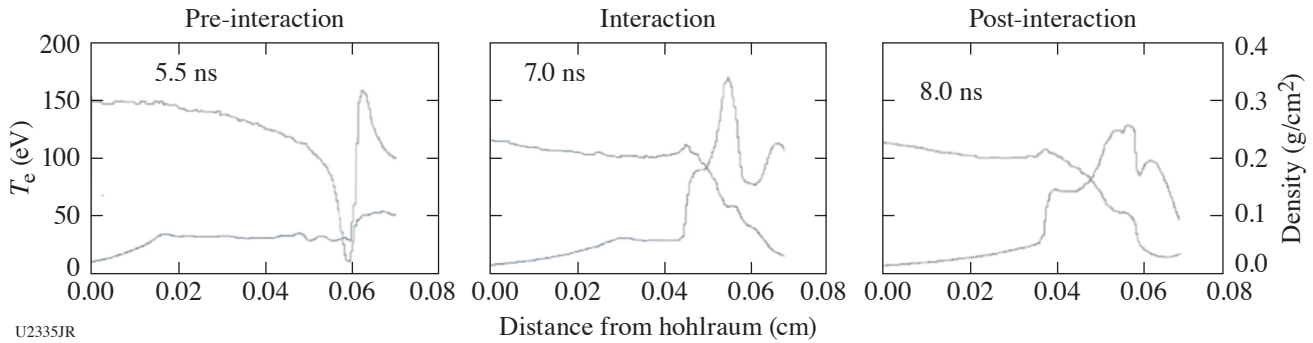
In FY18, Los Alamos National Laboratory carried out 21 shot days on the OMEGA and OMEGA EP Laser Systems in the areas of high-energy-density (HED) science and inertial confinement fusion (ICF). Our focus areas were on radiation flow, hydrodynamic turbulent mix and burn, and coupled Kelvin–Helmholtz (KH)/Richtmyer–Meshkov (RM) instability growth including convergent geometry. We also had several shot days that focused on transport properties in the kinetic regime. We continue to develop advanced diagnostics such

as neutron imaging and performed tests of a new imaging concept to be installed at the National Ignition Facility (NIF). We executed experiments in support of our double-shell campaign, and we began initial experiments using the new *Revolver* platform. Below is a summary of our campaigns, their motivation, and main results from this year.

#### Coax-18A/Radishock

In 2018 we had three shot days: Coax-18A in April 2018, Radishock-18A in August 2018, and Radishock-18B (a replacement day for another campaign) also in August 2018. The last Coax shot day, Coax-18A, was used for platform development and to obtain proof-of-principle data for the Radishock Campaign that began in FY18. The goal of the Radishock Campaign is to study the interaction between a supersonic radiation flow and an opposing shock. Supersonic flows and shocks interact in a number of astrophysical systems, such as solar coronas and pulsars. This process also provides a valuable experimental test for radiation-hydrodynamic models. The Radishock Campaign intends to provide high-resolution spatial temperature profiles and density profiles to study the radiation transport using the Coax platform.

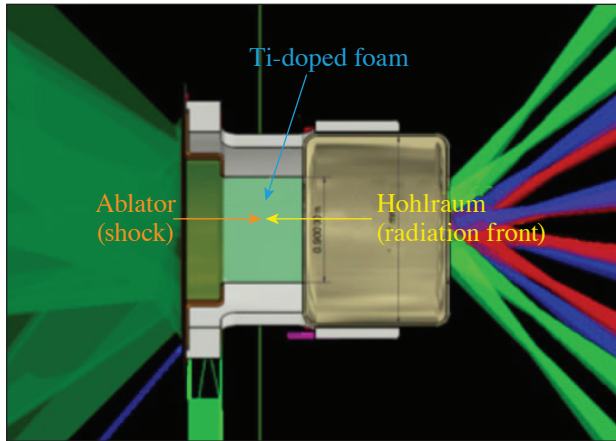
Figure 156.147 shows the density and temperature lineouts from three simulations at different times during the interaction between a supersonic flow and an opposing shock. At 5.5 ns the shape of the supersonic flow is unperturbed by the incoming shock, so this time is before the interaction. At 7 ns, the supersonic flow has hollowed out behind the interaction, and a 10- to 15-eV temperature spike occurs at the interaction. Only 1 ns later, the high-density peak of the shock has passed and the radiation flow has started to decay, but the perturbation is still observable. This is the beginning of the post-interaction phase.



U2335JR

Figure 156.147  
Density and temperature lineouts from three simulations at different times during the interaction between a supersonic flow and an opposing shock.

We used a Be ablator on one side of the target (left) to generate the shock and a hohlraum (right) to generate a supersonic flow. The two met in the middle of the Ti-doped aerogel in the physics target as shown in Fig. 156.148. The physics target was backlit by a Kr-filled glow-discharge polymer (GDP) capsule to produce K-shell absorption spectra observable by the 1-D space-resolving NIF-5 spectrometer. We used a vanadium foil point-projection backlighter with a 25- $\mu\text{m}$  pinhole to radiograph the target using a LANL CIPs-6x-6mm nose tip. Both primary diagnostics were mounted on x-ray framing cameras (XRFC's). Our last primary diagnostic was Dante, which views the hohlraum temperature through the laser entrance hole.



U2336JR

Figure 156.148  
The Radishock physics target showing the interaction region where the shock and radiation front meet.

In Coax-18A we tested the Radishock physics target design and the use of an extended hohlraum drive to prolong the life of the supersonic phase. We delayed half the hohlraum beams 1 ns after the other half, providing a longer duration drive but at

lower temperature. The two halves both provided a symmetric hohlraum drive. We tested a 24-beam drive on the Kr-filled capsule backlighter, which produces a significantly brighter x-ray flash with a shorter duration. We successfully observed the interaction and collected shock-only and hohlraum-only data for comparison. However, we discovered an “early-time light” effect on the x-ray radiography, which is caused by something (soft x rays, hard x rays, electrons) interacting with the microchannel plate before the camera is actually triggered, resulting in a bright diffuse “x” pattern on the radiograph.

In Radishock-18A we modified the physics target with additional shielding and focused on the beginning of the post-interaction phase. While we collected high-quality spectra of the interaction, we did not ameliorate the early-light effect. We switched to the use of an LAPC (Los Alamos pinhole camera) on D3,4,7,8 AGFA film to look for comparisons between self-emission of the (not backlit) target and the radiograph. We ruled out x-ray self-emission from the target between 1 and 10 keV as a cause for the early-light effect. We had unusual difficulty timing the spectrometer to the capsule flash. The capsule diameter was out of spec (too small), which reduced the repeatability of the capsule performance. We have discussed this problem with GA and do not expect a repeat of this issue in FY19.

Radishock-18B occurred two weeks after Radishock-18A as a replacement day for another campaign. We used targets that had been built for COAX-18A and Radishock-18A. We added two additional beams and tightened the focus to  $-2$  mm from  $-6$  mm on the V-foil backlighter. These changes allowed us to overcome the early-light effect and optimize our radiography to observe interaction between the radiation flow and the shock. We additionally fielded a shot where we looked for fast electrons with the single-channel electron spectrometer (SC-ESM) and soft x rays with the soft x-ray diagnostic. We had the hard x-ray detector on all day as well. These data are being

used to plan potential changes to the target design for FY19 to eliminate the cause of the early-light effect on the radiography.

Figure 156.149 shows examples of the data collected studying the interaction between the radiation flow and the shock for the three shot days. At 6.2 ns, the interaction barely started: the emission from the shock is barely visible but the spectral lines are not perturbed. At 7 to 7.8 ns we observed bright emission from the shock and clear perturbation of the spectral features, as well as the behavior of the shock itself in the radiograph. We did not see hydrodynamic motion from the hohlraum side because the radiation flow is supersonic. After 8 ns we observed that the shock continues to propagate but is significantly more diffuse and the disturbance of the radiation flow is still pronounced but the radiation flow has also cooled (fewer  $1s-2p$  lines). The shock and details of the target design including the window in the rexolite tube are highly visible in the radiographs taken in Radishock-18B. Analysis of this very recently collected data is still in progress.

**CylDRT**

In FY18, we had two CylDRT shot days at the Omega Laser Facility. The first shot day was on 8 March 2018 and the second shot day was completed on 19 September 2018. The CylDRT platform was developed to measure the Rayleigh–Taylor (RT) growth of the engineered sine wave initial perturbations on the inner side of an aluminum marker layer in cylindrical geometry. Both face-on and side-on x-radiographies were used as main

diagnostics. Figure 156.150 shows the axial and transverse views of the nominal cylindrical target. The cylinder was 2.5 mm long with a 986- $\mu\text{m}$  outer diameter. The inner diameter of the cylinder was 860  $\mu\text{m}$ . In the middle of the cylinder, there was a 500- $\mu\text{m}$ -long aluminum marker band on the inner side of the cylinder. The inner aluminum layer had sine-wave perturba-

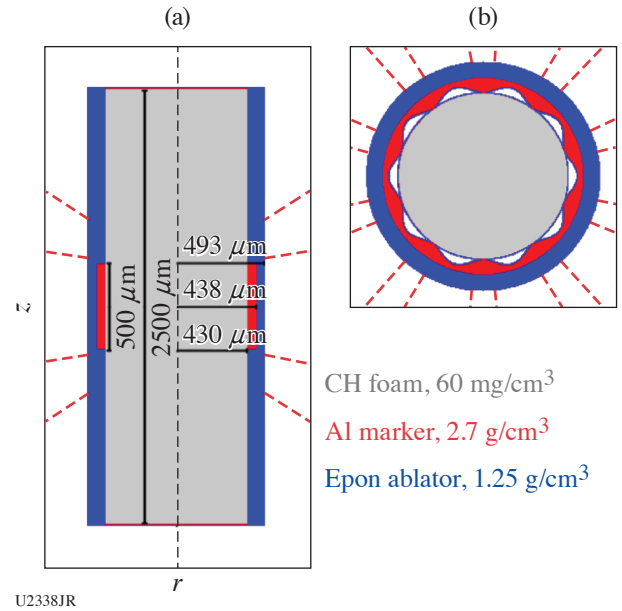


Figure 156.150 Sketch of (a) transverse and (b) axial views of the CylDRT target.

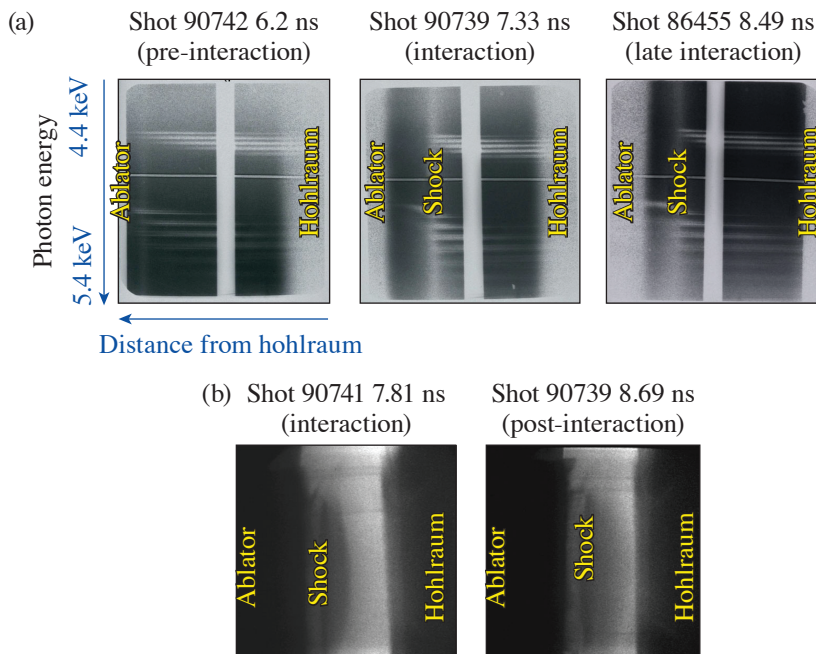


Figure 156.149 Examples of Radishock data: (a) 1-D spatially resolved spectra and (b) radiographs of the interaction.

tions. Figure 156.151 shows the experimental geometry. The cylinder was driven by 40 beams with a 1-ns square pulse. A nickel backlighter was attached to the TIM-4 end of the cylinder. The x-ray framing camera was used for face-on radiography in TIM-6. We used 12× magnification with a 10- $\mu\text{m}$  pinhole onto a four-strip charge-coupled device (CCD) (XRFC3). We also used a TIM-2/TIM-3 side imaging of the target to see the uniformity of the implosion with a 6× magnification.

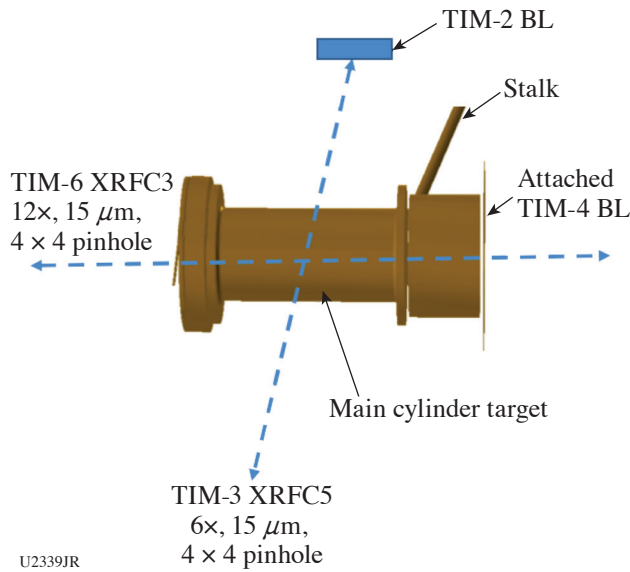


Figure 156.151  
Experimental geometry for the CyLDRT experiments.

Figure 156.151 shows the experimental geometry from Vis-Rad. The cylinder is aligned along the P6–P7 axis. The TIM-4 backlighter is attached to the main cylinder target. The cylinder was inserted via TPS2. The TIM-2/TIM-3 axis was used for the sidelighter imaging with a vanadium sidelight.

During the CyLDRT-18A shot day on 8 March, we measured the RT growth of mode-10 and mode-20 initial sine-wave perturbations (Figs. 156.152–156.154). The measured growth rate of these engineered perturbations agrees well with the *xRAGE* hydrodynamic simulations.

**DarkMix**

During an ICF implosion, a mixing of capsule ablator material into the DT fuel rapidly cools the fuel and inhibits fusion burn. Gamma-ray–based measurements from this campaign seek to estimate how much material is being mixed into the hot spot that is not being observed through other mix measurements (separated reactants/high-Z dopant spectra). The Dark

Mix Campaign utilizes a non-gamma-emitting capsule (e.g., beryllium) doped with a gamma-emitting layer (e.g., carbon). The time-dependent measurement of the gamma-emitting layer’s  $\rho R$  near bang time gives a measure of the “dark mix” or movement of material near the hot spot that is not heated to high temperatures (Fig. 156.155).

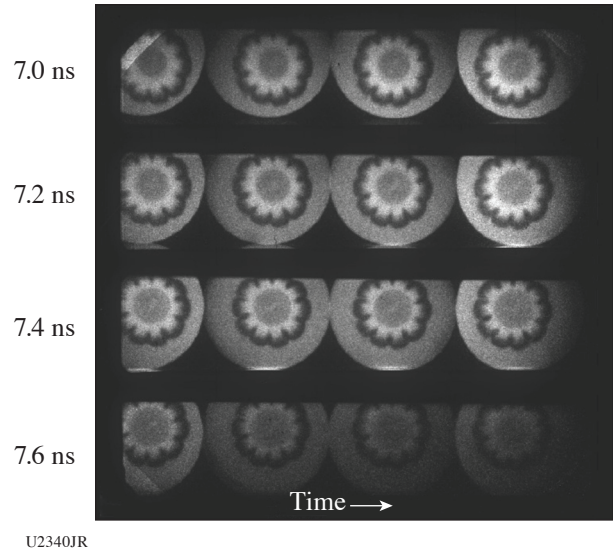


Figure 156.152  
Axial x-ray radiographs of a mode-10 sine-wave perturbation target (shot 88900: mode 10 with 2- $\mu\text{m}$  initial amplitude).

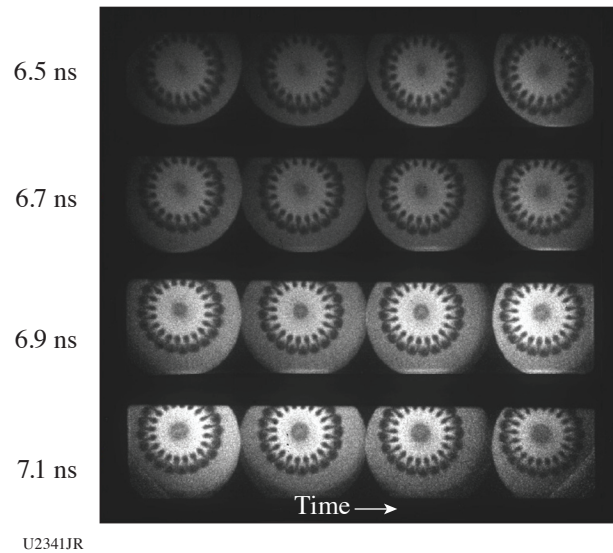


Figure 156.153  
Axial x-ray radiographs of a mode-20 sine-wave perturbation target (shot 88902: mode 20 with 4- $\mu\text{m}$  initial amplitude).

The design of the capsules for the 2018 shot day had a high degree of risk because of the difficulty in fabricating (Fig. 156.156). Most of the dark-mix capsules were cracked during the carbon layering process. In order to fill the beryllium/carbon capsule, a hole was laser drilled into the surviving capsules and plugged with a plastic glue, giving the capsules an appropriate diffusion half-life for a DT fill. On the shot

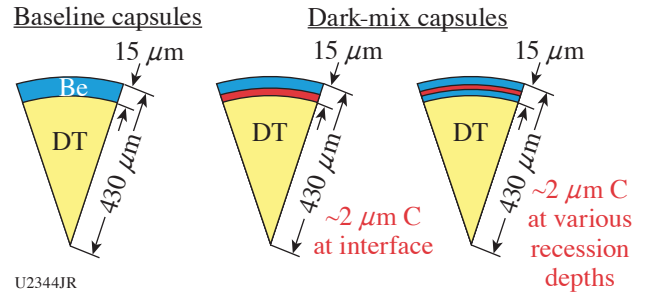


Figure 156.156  
Pie chart of dark-mix capsule designs.

day, however, it was observed that all the capsules were unsatisfactory with no measurable neutron yield. It is believed the cryogenic cycle from having capsules at liquid nitrogen and then warming them to room temperature caused the plug or the capsules themselves to fail, releasing all the DT gases.

**DSPlanar**

The LANL Double Shell team completed two planar double-shell (DSPlanar) experiments on the OMEGA laser in FY18. DSPlanar is part of a larger effort to study the 1-D and 2-D physics relevant to double-shell capsule implosions in a simpler, nonconvergent geometry. These experiments used an indirectly driven shock tube to study shock propagation, momentum transfer, and hydrodynamic instability growth and mitigation through novel material and density gradient inner shells, recently developed by GA.

The first DSPlanar experiment in FY18 used the velocity interferometer system for any reflector (VISAR) to perform drive standardization measurements. The data from these targets were intended to validate and calibrate our models and predict shock propagation through material-gradient inner shells. The measured shock breakout times are consistent with hydrodynamic simulation predictions. However, there was roughly a factor of 2 difference between the measured shock velocity between leg 1 and leg 2. It is not clear whether this difference was the result of the quality of the VISAR data or issues related to the VISAR data analysis. One contributor to the inconsistent data quality may have been preheat; significant hard x-ray signal levels were detected throughout the shot day coinciding with blanking of the VISAR data. We addressed this by adjusting our hohlraum gas fill and using a pre-pulse to burn off our hohlraum window. These changes contributed to an improved design for the following experiment.

The second DSPlanar experiment in FY18 studied the mitigation of hydrodynamic instabilities along the unstable inter-

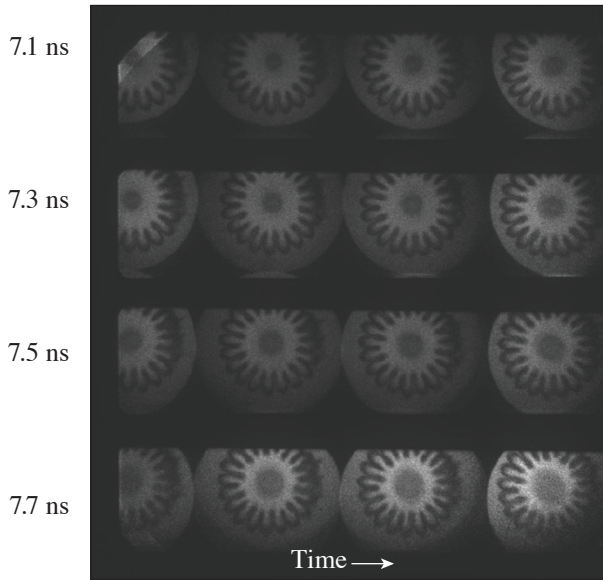


Figure 156.154  
Axial x-ray radiographs of a two-mode (mode-10 and mode-20) sine-wave perturbation target (shot 91097: mode 10 with 2-μm amplitude and mode 20 with 4-μm initial amplitude superimposed).

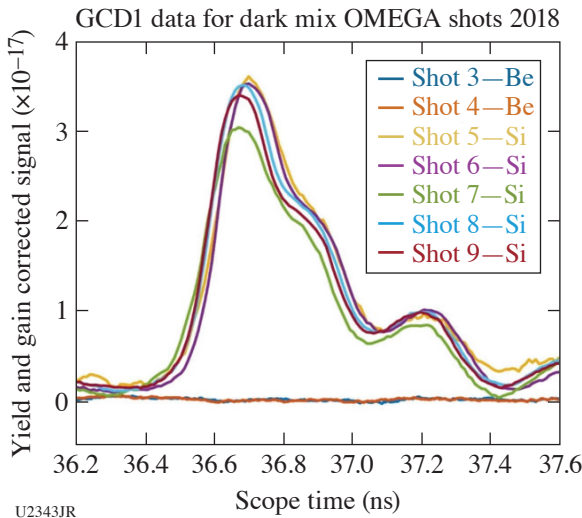


Figure 156.155  
Shot data showing that the dark-mix capsules were unsatisfactory.

face between the low-density foam and the high-density inner shell. Hydrodynamic instabilities are a significant degradation mechanism in ICF and are especially problematic at interfaces with large and sudden density jumps. Analytic theory suggests that we can mitigate instability growth by replacing these large density jumps with a smooth density gradient,<sup>89</sup> but these models do not account for complex effects of material gradients such as mixed opacities or mixed equations of state. Furthermore, there are significant challenges to simulating material gradients with our computational models, and these simulations have not yet been verified to accurately predict the behavior of material gradients. This experiment studied the mitigation of hydrodynamic instabilities along the inner shell by comparing the growth of precision-machined seed perturbations at three different density-change conditions [Fig. 156.157(a)]: a high-density inner shell (Zr), an inner shell (Zr) with a mid-density tamper (Be), and a novel inner shell that consists of a material and density gradient (Be to Zr). The preliminary analysis of the data [Fig. 156.157(b)] supports the theory that density-gradient inner shells can inhibit hydrodynamic instability growth to a greater degree than the current tampered-inner-shell design. An upcoming experiment is planned to further mitigate preheat, improve the quality of our side-on radiography, and iterate our

target design to more closely represent the physics of the NIF double-shell capsule now that we have verified our ability to diagnose instability growth in these upcoming targets.

**IonSepPlasma**

Two counterstreaming jets have been created by ablating two targets; for a given shot the two targets were made of the same material, and from shot to shot the material was changed: Au, Ag, Cu, Al, C, and Be targets have been used. Streaked Thomson scattering (TS) at the midplane showed that for higher-Z material, the two peaks in the velocity distribution merge, which can be attributed to collisional shock thermalization. Figure 156.158 shows such merging for Au obtained with three consecutive time frames in three shots. In the second half of the day, imaging TS was used to investigate the spatial shock structure. After post-processing it should provide further information about the achieved shock conditions. Post-processing of the proton radiography showed finer-scale field structures for lower-Z materials, which was washed out for higher-Z materials.

**Marble\_VC**

The Marble Void Collapse Campaign has been developed to address fundamental issues relevant to understanding marble

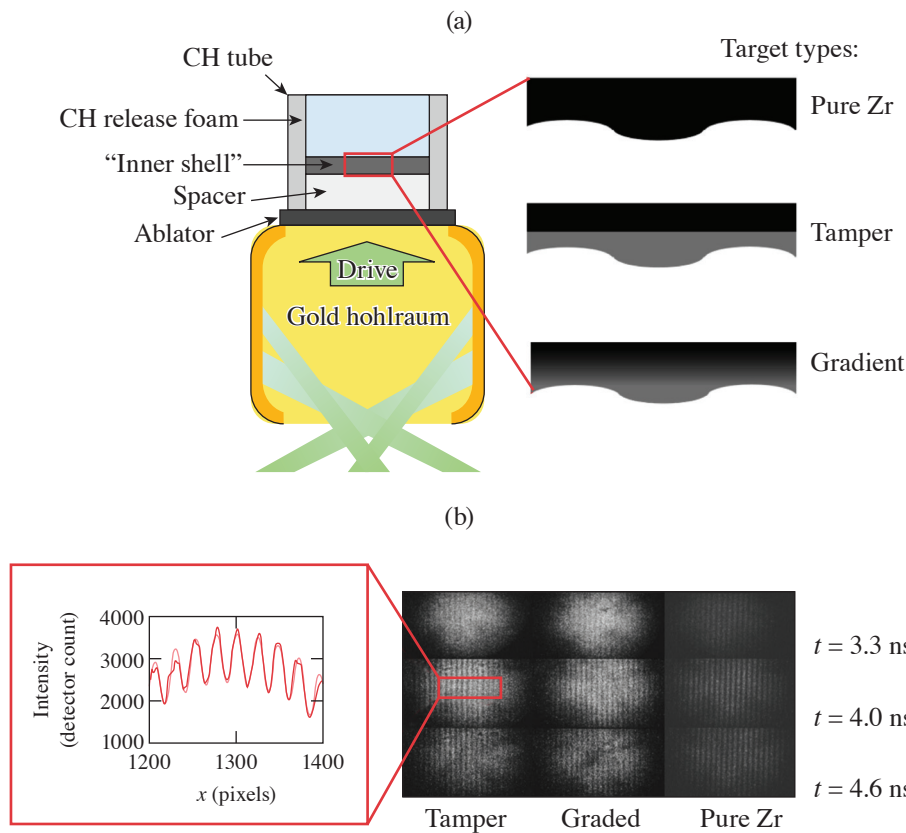
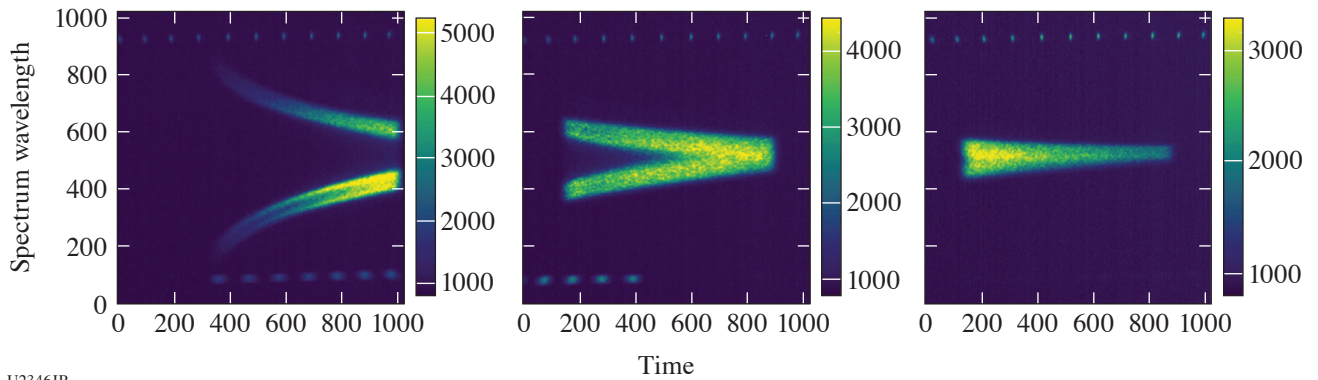


Figure 156.157  
 (a) DSPlanar target diagram showing the different "inner-shell" configurations driven;  
 (b) example data from the three types of targets.

U2345JR



U2346JR

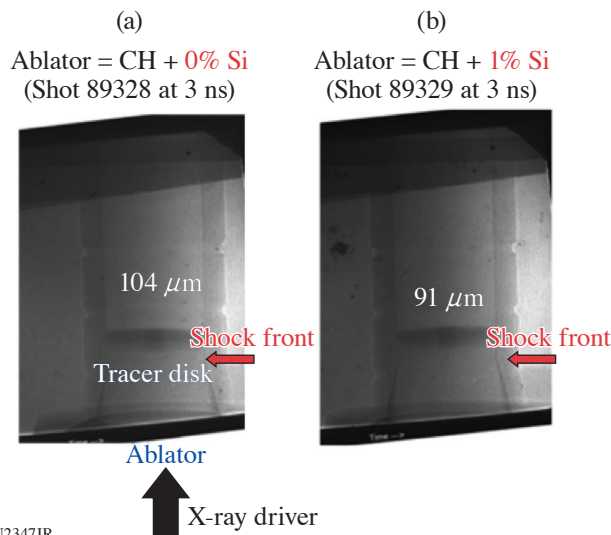
Figure 156.158 Merging of Au jets. Data are from three shots and represent consecutive times showing the merging of the jets.

implosions on the NIF and simulation capability of macropore engineered foams. This year, the Marble team adopted (1) an indirect-drive shock-tube platform to study preheat effects on marble foams and (2) a gas-filled shock tube to create a gas-filled void collapse condition on OMEGA.

For the preheat study, the shock tube was irradiated by x-ray flux produced inside a gold hohlraum. The shock tube was filled with a low-density CH foam and a thin layer of a plastic tracer disk (40  $\mu\text{m}$  thick), which was used as a preheat tracer marker. The expansion of the thin plastic layer indicates the amount of preheat deposited into foam. As shown in Fig. 156.159, the thickness of the plastic tracer disk increased as the shock propagated through the foam. Figure 156.160 shows a net growth width ( $L-L_0$ ) of the tracer disk as a function of time,

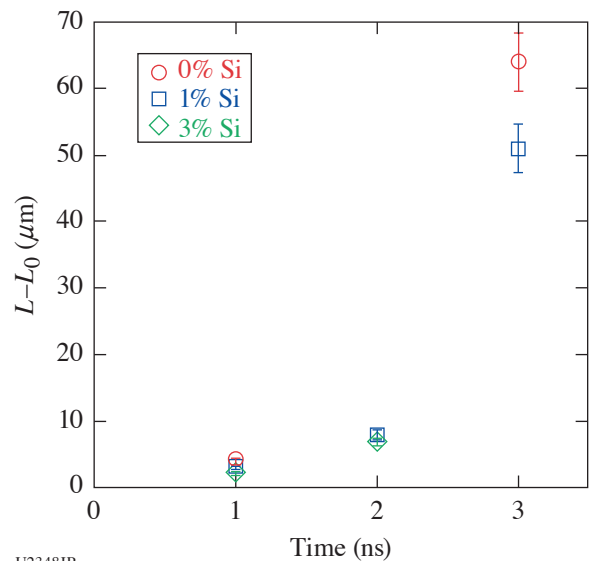
where the initial thickness  $L_0$  is 40  $\mu\text{m}$ . At early times up to 2 ns, the expansion rate is  $\sim 4 \mu\text{m}/\text{ns}$  and depends weakly on ablator compositions. Between 2 and 3 ns, the expansion rate increased significantly, as a shock front approached the plastic tracer disk. We began to see an influence of ablator compositions on the expansion rate. The undoped pure plastic ablator showed an  $\sim 15\%$  higher expansion rate than a plastic ablator doped with 1% Si. Currently, a RAGE simulation is underway to differentiate the effects of an M-band x ray and shock-front heating on the expansion rate.

A gas-filled void collapse platform was a new effort upgrading our previous foam-filled void collapse campaign. In FY16–FY17, a foam-filled void collapse platform demonstrated the ability to simulate the NIF Marble Campaign. However, the



U2347JR

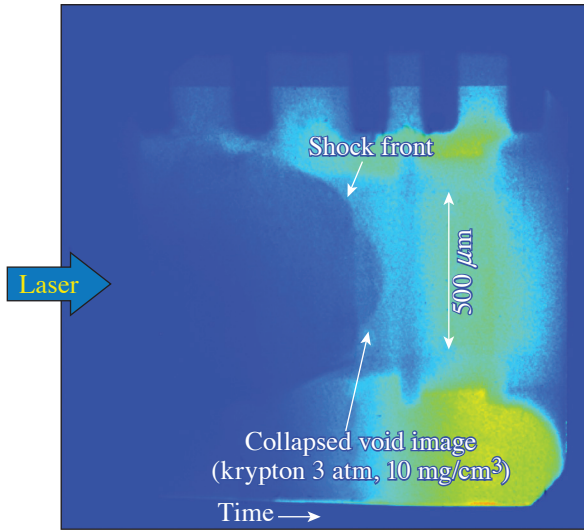
Figure 156.159 X-ray radiograph data recorded at  $t = 3 \text{ ns}$  for (a) an undoped plastic ablator and (b) an ablator doped with 1% Si.



U2348JR

Figure 156.160 Net growth width of the plastic tracer layer as a function of time.

density of foam void (50 to 70 mg/cm<sup>3</sup>) was still higher than the NIF marble condition. The goal was to create a gas-filled void collapse condition in a shock tube and radiograph the evolution of gas-filled void as the foam heats and expands. Adding an opaque gas, such as krypton, provided sufficient contrast from a chlorine-based backlit imaging. X-ray radiographic data shown in Fig. 156.161 shows a shock front passing through a single void (200 μm in diameter) filled with a 3-atm krypton gas. A collapsing-void image captured by an x ray shows that the shock compresses a spherical void without much turbulence.



Shot 90887, image taken at 12.5 ns

U2349JR

Figure 156.161  
Shock front passing through a single void (200 μm in diameter) filled with 3 atm of krypton. A collapsing-void image was captured by an x-ray back-lighter image.

The newly developed gas-filled void-collapse platform can be used to benchmark LANL simulations, relevant to a NIF Marble Campaign.

**ModCons**

The LANL ModCons Campaign has successfully tested the new 15× version of the spherical crystal imager with a quartz crystal cut to look at the Mn He<sub>α</sub> line, ~6.2 keV. Moving from the old 10× configuration to the new 15× configuration allows us to resolve much finer features, with a feature size down to below 5 μm, using a CCD instead of image plates. This will allow the ModCons platform to begin taking a series of data aimed at understanding mode competition in RM by shock-driven flows. Figure 156.162 is an example of a test object in the image plane (slightly over exposed) and a data shot showing the breakup of the RM/RT-induced fingers.

**mShock**

The mShock Campaign tested a number of new target configurations for looking at preheat in the targets (Fig. 156.163). The preheat campaign measured the electron and x-ray production from our ablators and the effects of those components on the physics package. Electrons with energies over 300 keV were observed, as well as a rough spectrum of the high-energy x rays using HERIE. Data were taken in two configurations, which allowed us to look at both the electron and x-ray data from two points, each for the same set of targets and condition. These results will allow us to tune the heating of the target in the coming fiscal year. In addition to the preheat studies, the mShock Campaign also took data for shock and reshock from the opposite side of the tube on a thin layer inside the tube to study the effects of feedthrough on a RM unstable pair of surfaces and to scope out the parameters we would like to test on the NIF.

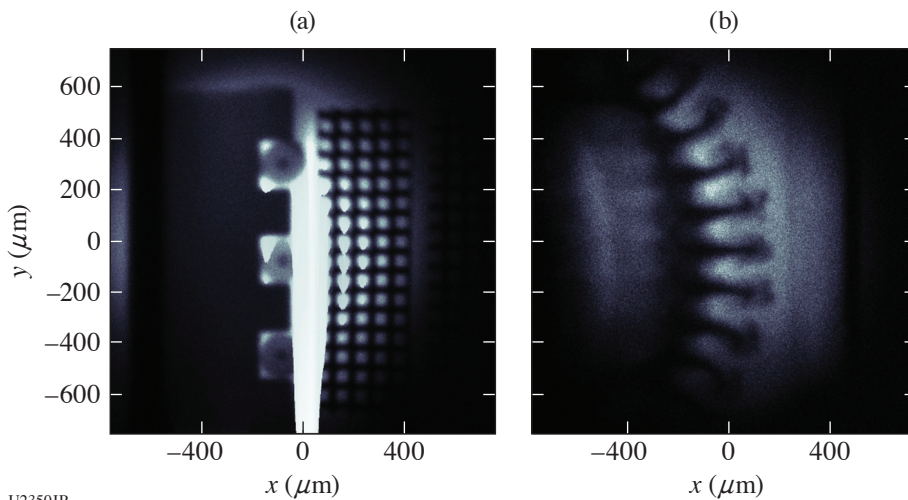


Figure 156.162  
(a) Test object at target chamber center with a 400-lpi grid with a 10% to 90% width of ~5 μm. Also seen are end-on 100-μm-radius boron rods with tungsten wires inside. (b) Data shot showing the growth of fingers from a shock-driven flow and the fine features at the tips showing breakup of the fingers.

U2350JR

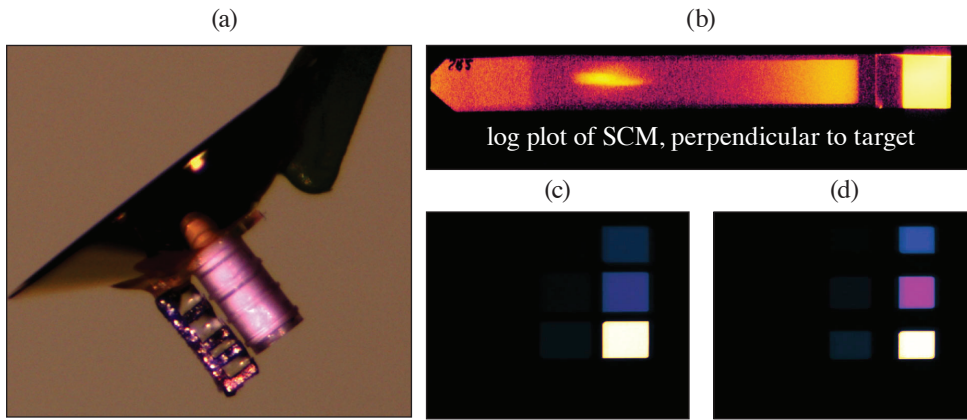


Figure 156.163  
 (a) A variant of the mShock target setup for single-sided drive and preheat conditions. (b) Preheat data from the single-channel electron spectrometer and from the HERIE filters on IP from looking (c) toward the target and (d) through the target.

U2351JR

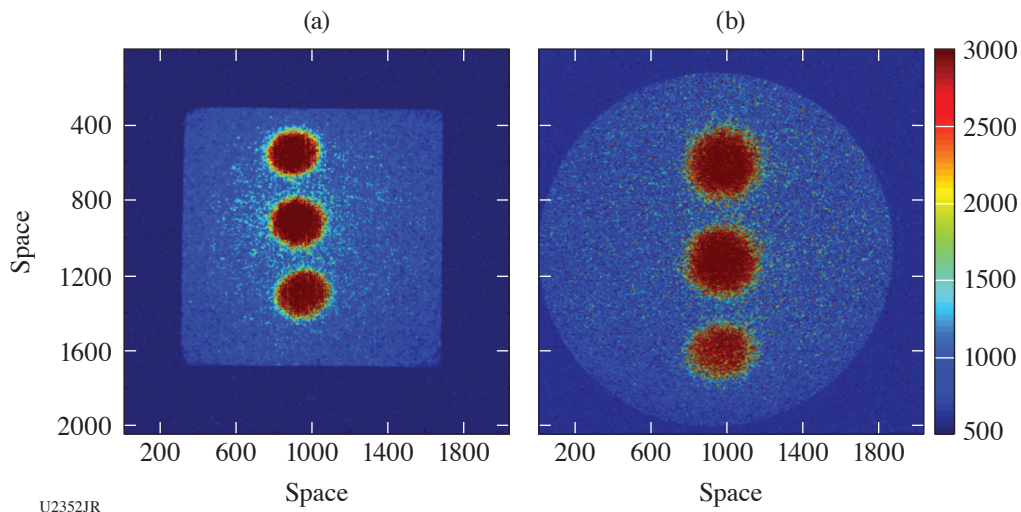
**NIS**

The LANL P-23 Advanced Imaging team fielded experiments for one ride-along and two full days at Omega in December 2017. The analysis of NIS-18A and -18B Campaign data is ongoing but has already strongly influenced design decisions for the construction of a new neutron-imaging line of sight on the NIF in 2019.

With NIS-18A “Neutron Pinhole Imaging with NIF Prototype Scintillators,” the team was able to show the feasibility of a lens-coupled neutron-imaging system based on a monolithic scintillator for the NIF. The campaign included fielding the novel prototype on the same line of sight with a previously used fiber scintillator system. Radiographic test objects were studied using a mix of plastic and Hoppe glass DT targets to collect performance data on the new system with different scintillator

choices: an EJ-262 plastic scintillator and a Liquid-VI liquid scintillator cell.<sup>90</sup> The team was able to field a penumbral aperture array for the second part of the campaign and obtain proof-of-principle penumbral neutron images. Figure 156.164 shows penumbral images obtained with the fiber array and the new monolithic system, demonstrating the feasibility of the monolithic scintillator lens-coupled prototype for the NIF.

NIS-18B was a continuation of NIS-Multiview-16A, a campaign to develop 3-D imaging of asymmetric implosions using x rays and neutrons. The previous x-ray imaging experiments laid the groundwork for the development of 3-D reconstruction algorithms that will allow limited-view tomography in neutron imaging on the NIF.<sup>91</sup> The goal for NIS-18B was to complete the multiview x-ray imaging data for highly asymmetric high-yield implosions in order to compare the full set to radiation-



U2352JR

Figure 156.164  
 The proof-of-principle penumbral neutron images obtained with (a) the existing plastic fiber array system and (b) the novel monolithic scintillator lens-coupled prototype for the NIF.

hydrodynamic simulations. In addition, the team attempted to add pseudo two-view neutron imaging by rotating the target symmetry and drive configuration to align with the TIM-4/TIM-6 axis for some shots. The second axis neutron imaging could not be completed since all targets on TIM-4 were lost as a result of issues with the target positioner. The multiview x-ray images for the successful asymmetry shots confirm, however, the -16-A data and strengthen an upcoming publication on the comparison to simulations.

**Revolver**

*Revolver* is a triple-shell, direct-drive ignition concept for ICF<sup>92,93</sup> aimed at coupling the maximum amount of laser energy into a compressed core of liquid DT fuel. As currently conceived, *Revolver* ignition targets have an outer Be ablator shell, a middle Cu driver shell, and an inner Au pusher shell filled with liquid-DT fuel. *Revolver* has been designed to couple >35 kJ of inward kinetic energy into the inner Au shell and fuel, producing a fuel convergence ratio C of 9 and a fusion yield of 4.4 MJ, using 1.5 MJ of the NIF's laser energy. *Revolver*'s large 6-mm-diam outer Be ablator shell allows for low laser illumination intensity  $\leq 3 \times 10^{14}$  W/cm<sup>2</sup> and small laser-spot-radius to capsule-radius ratio of <0.4. Both of these characteristics mitigate the deleterious effects of laser-plasma instabilities including cross-beam energy transfer (CBET) and couple the maximum amount of energy into capsule inward kinetic energy.

The Revolver-18A/B Campaigns on OMEGA (23–24 January 2018) successfully measured laser-coupling energetics,

symmetry control, and CBET mitigation of 1/6-scale outer Be ablator shells. Three different capsule diameters (870, 1040, and 1220  $\mu\text{m}$ ) were employed to validate the increase in capsule kinetic energy as the ratio of laser/capsule radius was reduced. We obtained sufficient experimental data to validate our ability to model the Be-shell implosion trajectory (Fig. 156.165) and symmetry, and we verified the increasing absorbed laser energy with decreasing laser-spot-radius to capsule-radius ratio (Fig. 156.166). Agreement between the simulated and measured scattered energies was validated down to the few-percent level; Fig. 156.166 indicates that the experiments did not exhibit

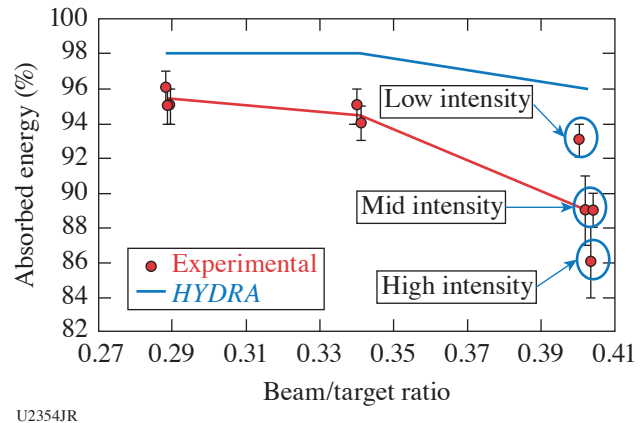


Figure 156.166 Capsule absorbed energy (red data points are inferred from scatter calorimeters; blue line represents 2-D HYDRA simulations) versus laser-spot-radius to capsule-radius ratio, showing that absorbed energy decreases with both increasing laser/capsule ratio and laser intensity.

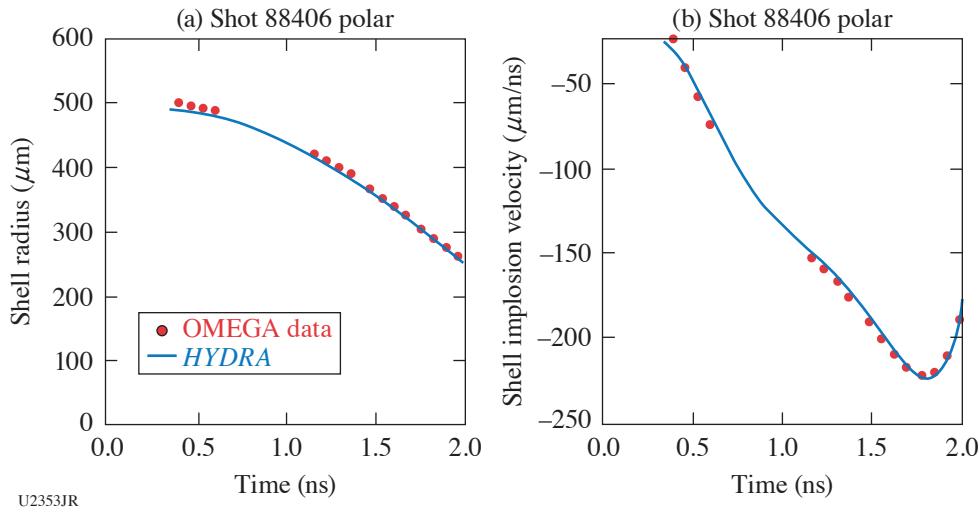


Figure 156.165 Example Be-shell (a) radius and (b) velocity versus time for a polar-direct-drive shot, as inferred from x-ray self-emission imaging and 2-D HYDRA simulations.

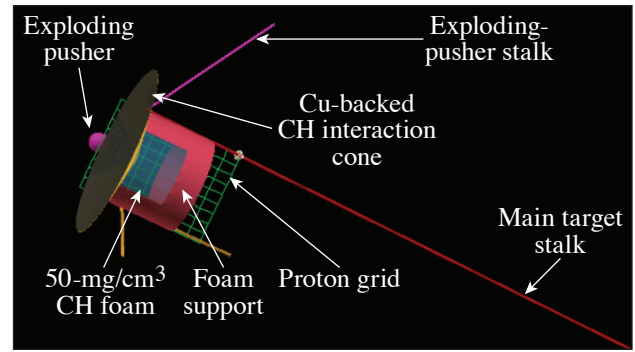
significant loss of laser energy at *Revolver* laser conditions. In addition, during *Revolver-18B*, we demonstrated the use of Cu shell dopant and a Fe backlighter target for backlighting full-scale NIF ablator shots in FY19.

**FY18 NRL Report on Omega Laser Facility Experiments**

During FY18 NRL, in collaboration with LLE, executed two shot days on OMEGA EP. Using an x-ray prepulse, the OMEGA EP experiments determined the minimum high-Z coating thickness (300 Å Pd) as well as the minimum expansion time (6 ns) needed for imprint reduction (Fig. 156.167). This information is being used to design OMEGA spherical target experiments. The OMEGA EP experiments also investigated whether an unsmoothed laser prepulse could be used to pre-expand the high-Z coating for imprint suppression. These shots showed persistent laser imprint despite a range of coatings and prepulse parameters tested. This result indicates that smoothing by spectral dispersion will be necessary for the OMEGA experiments utilizing a laser prepulse.

**FY18 RAL Report on the Omega Facility Experiments**

The goal of this work is to characterize laser-plasma interactions and the resulting hot electrons at intensities relevant to shock ignition ( $1 \times 10^{15}$  to  $10^{16}$  W/cm<sup>2</sup>) in the ablation plasma conditions anticipated to occur in NIF direct-drive implosions (density scale length 500 μm, electron temperature ~4 keV). Simulations indicated this was not possible with a planar target with density scale lengths of the order of 250 μm; however, by using a new experimental platform (Fig. 156.168) that employs a novel open-cone geometry target in combination with beam repointings, ablation plasma conditions of 500-μm density scale length and 2.8-keV electron temperature were established at the point when the high-intensity beams switched on. Simulations indicate the high-intensity beams reached a peak incident intensity of  $8.5 \times 10^{15}$  W/cm<sup>2</sup>, with the intensity at a quarter critical of  $6 \times 10^{15}$  W/cm<sup>2</sup>. This raised the electron temperature to 3.5 keV.



U2334JR

Figure 156.168  
Experimental setup with a novel open-cone geometry target.

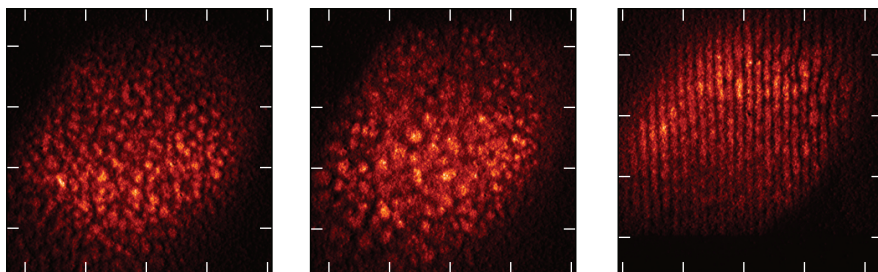
Analysis suggests the interaction of the high-intensity beam with this hot, long-scale-length plasma is entirely dominated by stimulated Raman scattering, with no two-plasmon-decay (TPD) signature visible in the backscattered-light spectra. Of particular interest is that initial analysis suggests the hot-electron temperature is significantly lower than previously measured at 25 to 30 keV. If verified, this is sufficiently low that hot electrons may prove beneficial for shock ignition. Interestingly, when the scale length was deliberately shorted by using a planar target, a TPD signature became visible. Analysis is ongoing.

OMEGA provided an excellent data set, which has enabled us to realize our project's goals.

REFERENCES

1. W. Fox, G. Fiksel, D. Haberberger, D. B. Schaeffer, J. Matteucci, M. Rosenberg, S. X. Hu, K. Lezhnin, A. Bhattacharjee, and K. Germaschewski, "A Novel Kinetic Mechanism for the Onset of Fast Magnetic Reconnection and Plasmoid Turbulence in Collisionless Plasmas," submitted to Nature.
2. D. B. Schaeffer, W. Fox, D. Haberberger, G. Fiksel, A. Bhattacharjee, D. H. Barnak, S. X. Hu, and K. Germaschewski, Phys. Rev. Lett. **119**, 025001 (2017).

(a) 800-Å Pd, 30-μm ripple laser prepulse at -5 ns    (b) 600 -Å Pd, flat laser prepulse at -10 ns    (c) 400-Å Pd, 30-μm ripple x-ray prepulse at -12 ns



U2355JR

Figure 156.167  
X-ray radiography of accelerated foil with a high-Z coating pre-expanded by a laser prepulse with [(a),(b)] no smoothing and (c) x-ray prepulse.

3. D. B. Schaeffer, W. Fox, D. Haberberger, G. Fiksel, A. Bhattacharjee, D. H. Barnak, S. X. Hu, K. Germaschewski, and R. K. Follett, *Phys. Plasma* **24**, 122702 (2017).
4. D. B. Schaeffer, W. Fox, R. K. Follett, G. Fiksel, C. K. Li, J. Matteucci, A. Bhattacharjee, and K. Germaschewski, "Particle Velocity Distributions in Developing Magnetized Collisionless Shocks in Laser-Produced Plasmas," to be submitted to *Physical Review Letters*.
5. S. Brygoo, M. Millot, P. Loubeyre, A. E. Lazicki, S. Hamel, T. Qi, P. M. Celliers, F. Coppari, J. H. Eggert, D. E. Fratanduono, D. G. Hicks, J. R. Rygg, R. F. Smith, D. C. Swift, G. W. Collins, and R. Jeanloz, *J. Appl. Phys.* **118**, 195901 (2015).
6. A. E. Raymond, C. F. Dong, A. McKelvey, C. Zulick, N. Alexander, A. Bhattacharjee, P. T. Campbell, H. Chen, V. Chvykov, E. Del Rio, P. Fitzsimmons, W. Fox, B. Hou, A. Maksimchuk, C. Mileham, J. Nees, P. M. Nilson, C. Stoeckl, A. G. R. Thomas, M. S. Wei, V. Yanovsky, K. Krushelnick, and L. Willingale, *Phys. Rev. E* **98**, 043207 (2018).
7. H. Sio, "Using Time-Resolved Nuclear Diagnostics to Probe Kinetic/Multi-Ion Physics and Shock Dynamics On OMEGA and the NIF," Ph.D. thesis, Massachusetts Institute of Technology, 2018.
8. H. Sio, J. A. Frenje, A. Le, S. Atzeni, T. J. T. Kwan, M. Gatu Johnson, G. Kagan, C. Stoeckl, C. K. Li, C. E. Parker, C. J. Forrest, V. Glebov, N. V. Kabadi, A. Bose, H. G. Rinderknecht, P. Amendt, D. T. Casey, R. Mancini, W. T. Taitano, B. Keenan, A. N. Simakov, L. Chacón, S. P. Regan, T. C. Sangster, E. M. Campbell, F. H. Séguin, and R. D. Petrasso, "Exploring the Dynamics of Kinetic/Multi-Ion Effects and Ion-Electron Equilibration Rates in ICF Plasmas at Omega," submitted to *Physical Review Letters*.
9. H. Sio, R. Hua, Y. Ping, C. McGuffey, F. Beg, R. Heeter, C. K. Li, R. D. Petrasso, and G. W. Collins, *Rev. Sci. Instrum.* **88**, 013503 (2017).
10. C. K. Li, V. Tikhonchuk, Q. Moreno, A. Bott, S. Feister, H. Sio, E. D'Humieres, P. Tzeferacos, G. Gregori, R. D. Petrasso, D. Q. Lamb, X. Ribeyre, P. Korneev, S. Atzeni, R. Betti, E. M. Campbell, R. Follett, J. A. Frenje, S. X. Hu, C. M. Huntington, M. Koenig, H. S. Park, B. A. Remington, A. Rigby, J. S. Ross, D. D. Ryutov, Y. Sakawa, T. C. Sangster, F. H. Séguin, S. C. Wilks, and S. Zhang, "Weibel-Mediated Collisionless Shocks Driven by Supersonic Plasma Flows," submitted to *Science*.
11. M. Gatu Johnson, B. D. Appelbe, J. P. Chittenden, A. Crilly, J. Delettrez, C. Forrest, J. A. Frenje, V. Yu. Glebov, W. Grimble, B. M. Haines, I. V. Igumenshchev, R. Janezic, J. P. Knauer, B. Lahmann, F. J. Marshall, T. Michel, F. H. Séguin, C. Stoeckl, C. Walsh, A. B. Zylstra, and R. D. Petrasso, *Phys. Plasmas* **26**, 012706 (2019).
12. M. Gatu Johnson, B. D. Appelbe, J. P. Chittenden, J. Delettrez, C. Forrest, J. A. Frenje, V. Yu. Glebov, W. Grimble, B. M. Haines, I. Igumenshchev, R. Janezic, J. P. Knauer, B. Lahmann, F. J. Marshall, T. Michel, F. H. Séguin, C. Stoeckl, C. Walsh, A. B. Zylstra, and R. D. Petrasso, *Phys. Rev. E* **98**, 051201(R) (2018).
13. J. A. Frenje, R. Florido, R. Mancini, T. Nagayama, P. E. Grabowski, H. Rinderknecht, H. Sio, A. Zylstra, M. Gatu Johnson, C. K. Li, F. H. Séguin, R. D. Petrasso, V. Yu. Glebov, and S. P. Regan, *Phys. Rev. Lett.* **122**, 015002 (2019).
14. M. Gatu Johnson, J. Katz, C. Forrest, J. A. Frenje, V. Yu. Glebov, C. K. Li, R. Paguio, C. E. Parker, C. Robillard, T. C. Sangster, M. Schoff, F. H. Séguin, C. Stoeckl, and R. D. Petrasso, *Rev. Sci. Instrum.* **89**, 101129 (2018).
15. M. Gatu Johnson, C. J. Forrest, D. B. Sayer, A. Bacher, J.-L. Bourgade, C. R. Brune, J. A. Caggiano, D. T. Casey, J. A. Frenje, V. Yu. Glebov, G. M. Hale, R. Hatarik, H. W. Herrmann, R. Janezic, Y. H. Kim, J. P. Knauer, O. Landoas, D. P. McNabb, M. W. Paris, R. D. Petrasso, J. E. Pino, S. Quaglioni, B. Rosse, J. Sanchez, T. C. Sangster, H. Sio, W. Shmayda, C. Stoeckl, I. Thompson, and A. B. Zylstra, *Phys. Rev. Lett.* **121**, 042501 (2018).
16. M. Gatu Johnson, A. B. Zylstra, A. Bacher, C. R. Brune, D. T. Casey, C. Forrest, H. W. Herrmann, M. Hohenberger, D. B. Sayre, R. M. Bionta, J.-L. Bourgade, J. A. Caggiano, C. Cerjan, R. S. Craxton, D. Dearborn, M. Farrell, J. A. Frenje, E. M. Garcia, V. Yu. Glebov, G. Hale, E. P. Hartouni, R. Hatarik, M. Hohensee, D. M. Holunga, M. Hoppe, R. J. Janezic, S. F. Khan, J. D. Kilkenny, Y. H. Kim, J. P. Knauer, T. R. Kohut, B. Lahmann, O. Landoas, C. K. Li, F. J. Marshall, L. Masse, A. McEvoy, P. McKenty, D. P. McNabb, A. Nikroo, T. G. Parham, M. Paris, R. D. Petrasso, J. Pino, P. B. Radha, B. Remington, H. G. Rinderknecht, H. Robey, M. J. Rosenberg, B. Rosse, M. Rubery, T. C. Sangster, J. Sanchez, M. Schmitt, M. Schoff, F. H. Séguin, W. Seka, H. Sio, C. Stoeckl, and R. E. Tipton, *Phys. Plasmas* **24**, 041407 (2017).
17. L. E. Chen, A. F. A. Bott, P. Tzeferacos, A. Rigby, A. Bell, R. Bingham, J. Katz, M. Koenig, C. K. Li, R. Petrasso, H.-S. Park, J. S. Ross, D. Ryu, D. Ryutov, T. G. B. White, B. Reville, J. Matthews, J. Meinecke, F. Miniati, E. G. Zweibel, S. Sarkar, A. A. Schekochihin, D. Q. Lamb, D. H. Froula, and G. Gregori, "Measurement of Cosmic Ray Super-Diffusion in a Laboratory Turbulent Plasma," to be submitted to *Physical Review Letters*.
18. V. Gopalaswamy, R. Betti, J. P. Knauer, A. Bose, N. Luciani, I. V. Igumenshchev, K. S. Anderson, K. A. Bauer, M. J. Bonino, E. M. Campbell, D. Cao, A. R. Christopherson, G. W. Collins, T. J. B. Collins, J. R. Davies, J. A. Delettrez, D. H. Edgell, R. Epstein, C. J. Forrest, D. H. Froula, V. Yu. Glebov, V. N. Goncharov, D. R. Harding, S. X. Hu, D. W. Jacobs-Perkins, R. T. Janezic, J. H. Kelly, O. M. Mannion, F. J. Marshall, D. T. Michel, S. Miller, S. F. B. Morse, D. Patel, P. B. Radha, S. P. Regan, S. Sampat, T. C. Sangster, A. B. Sefkow, W. Seka, R. C. Shah, W. T. Shmayda, A. Shvydky, C. Stoeckl, W. Theobald, K. M. Woo, J. D. Zuegel, M. Gatu Johnson, R. D. Petrasso, C. K. Li, and J. A. Frenje, "Tripling the Yield in Direct-Drive Laser Fusion via Statistical Modeling," to be published in *Nature*.
19. L. Gao, E. Liang, Y. Lu, R. Follett, H. Sio, P. Tzeferacos, D. Froula, A. Birkel, C. K. Li, D. Lamb, R. Petrasso, W. Fu, M. Wei, and H. Ji, "Mega-Gauss Plasma Jet Creation Using a Ring of 20 Laser Beams," submitted to *Physical Review Letters*.
20. P. E. Masson-Laborde *et al.*, "Interpretation of Proton Radiography Experiments in a Hohlraum with 3-D Simulations," submitted to *Physical Review Letters*.
21. Y. Lu, P. Tzeferacos, E. Liang, R. Follett, L. Gao, A. Birkel, D. Froula, W. Fu, H. Ji, D. Lamb, C. K. Li, H. Sio, R. Petrasso, and M. Wei, "Simulation of Magnetized Jet Creation Using a Hollow Ring of 20 Laser Beams."
22. A. Bose, R. Betti, D. Mangino, K. M. Woo, D. Patel, A. R. Christopherson, V. Gopalaswamy, O. M. Mannion, S. P. Regan, V. N. Goncharov, D. H. Edgell, C. J. Forrest, J. A. Frenje, M. Gatu Johnson, V. Yu. Glebov, I. Igumenshchev, J. P. Knauer, F. J. Marshall, P. B. Radha, R. Shah, C. Stoeckl, W. Theobald, T. C. Sangster, D. Shvarts, and E. M. Campbell, *Phys. Plasma* **26**, 062701 (2018).

23. P. Tzeferacos, A. Rigby, A. F. A. Bott, A. R. Bell, R. Bingham, A. Casner, F. Cattaneo, E. M. Churazov, J. Emig, F. Fiuza, C. B. Forest, J. Foster, C. Graziani, J. Katz, M. Koenig, C. K. Li, J. Meinecke, R. Petrasso, H. S. Park, B. A. Remington, J. S. Ross, D. Ryu, D. Ryutov, T. G. White, B. Reville, F. Miniati, A. A. Schekochihin, D. Q. Lamb, D. H. Froula, and G. Gregori, *Nat. Commun.* **9**, 591 (2018).
24. A. B. Zylstra, J. A. Frenje, M. Gatu Johnson, G. M. Hale, C. R. Brune, A. Bacher, D. T. Casey, C. K. Li, D. McNabb, M. Paris, R. D. Petrasso, T. C. Sangster, D. B. Sayre, and F. H. Séguin, *Phys. Rev. Lett.* **119**, 222701 (2017).
25. A. McKelvey, G. E. Kemp, P. A. Sterne, A. Fernandez-Panella, R. Shepherd, M. Marinak, A. Link, G. W. Collins, H. Sio, J. King, R. R. Freeman, R. Hua, C. McGuffey, J. Kim, F. N. Beg, and Y. Ping, *Sci. Rep.* **7**, 7015 (2017).
26. R. Hua, H. Sio, S. C. Wilks, F. N. Beg, C. McGuffey, M. Bailly-Grandvaux, G. W. Collins, and Y. Ping, *Appl. Phys. Lett.* **111**, 034102 (2017).
27. V. N. Goncharov, S. P. Regan, E. M. Campbell, T. C. Sangster, P. B. Radha, J. F. Myatt, D. H. Froula, R. Betti, T. R. Boehly, J. A. Delettrez, D. H. Edgell, R. Epstein, C. J. Forrest, V. Yu. Glebov, D. R. Harding, S. X. Hu, I. V. Igumenshchev, F. J. Marshall, R. L. McCrory, D. T. Michel, W. Seka, A. Shvydky, C. Stoeckl, W. Theobald, and M. Gatu-Johnson, *Plasma Phys. Control. Fusion* **59**, 014008 (2017).
28. H. G. Rinderknecht, P. A. Amendt, M. J. Rosenberg, C. L. Li, J. A. Frenje, M. Gatu Johnson, H. Sio, F. H. Séguin, R. D. Petrasso, A. B. Zylstra, G. Kagan, N. M. Hoffman, D. Svyatsky, S. C. Wilks, V. Yu. Glebov, C. Stoeckl, and T. C. Sangster, *Nucl. Fusion* **57**, 066014 (2017).
29. C. J. Forrest, P. B. Radha, J. P. Knauer, V. Yu. Glebov, V. N. Goncharov, S. P. Regan, M. J. Rosenberg, T. C. Sangster, W. T. Shmayda, C. Stoeckl, and M. Gatu Johnson, *Phys. Rev. Lett.* **118**, 095002 (2017).
30. C. Stoeckl, R. Epstein, R. Betti, W. Bittle, J. A. Delettrez, C. J. Forrest, V. Yu. Glebov, V. N. Goncharov, D. R. Harding, I. V. Igumenshchev, D. W. Jacobs-Perkins, R. T. Janezic, J. H. Kelly, T. Z. Kosc, R. L. McCrory, D. T. Michel, C. Mileham, P. W. McKenty, F. J. Marshall, S. F. B. Morse, S. P. Regan, P. B. Radha, B. S. Rice, T. C. Sangster, M. J. Shoup III, W. T. Shmayda, C. Sorce, W. Theobald, J. Ulreich, M. D. Wittman, D. D. Meyerhofer, J. A. Frenje, M. Gatu Johnson, and R. D. Petrasso, *Phys. Plasmas* **24**, 056304 (2017).
31. M. J. Buehler *et al.*, *Phys. Rev. Lett.* **99**, 165502 (2007).
32. R. Pérez and P. Gumbsch, *Phys. Rev. Lett.* **84**, 5347 (2000).
33. J. G. Swadener, M. I. Baskes, and M. Nastasi, *Phys. Rev. Lett.* **89**, 085503 (2002).
34. P. M. Celliers, D. J. Erskine, C. M. Sorce, D. G. Braun, O. L. Landen, and G. W. Collins, *Rev. Sci. Instrum.* **81**, 035101 (2010).
35. R. S. McWilliams, J. H. Eggert, D. G. Hicks, D. K. Bradley, P. M. Celliers, D. K. Spaulding, T. R. Boehly, G. W. Collins, and R. Jeanloz, *Phys. Rev. B* **81**, 014111 (2010).
36. J. Sheng *et al.*, "Enhancing Positron Production Using Front Surface Target Structures," submitted to *Physical Review Letters*.
37. H. Chen *et al.*, *Phys. Rev. Lett.* **102**, 105001 (2009).
38. H. Chen, S. C. Wilks, D. D. Meyerhofer, J. Bonlie, C. D. Chen, S. N. Chen, C. Courtois, L. Elberson, G. Gregori, W. Kruer, O. Landoas, J. Mithen, J. Myatt, C. D. Murphy, P. Nilson, D. Price, M. Schneider, R. Shepherd, C. Stoeckl, M. Tabak, R. Tommasini, and P. Beiersdorfer, *Phys. Rev. Lett.* **105**, 015003 (2010).
39. H. Chen *et al.*, *Phys. Plasmas* **21**, 040703 (2014).
40. O. V. Gotchev, J. P. Knauer, P. Y. Chang, N. W. Jang, M. J. Shoup III, D. D. Meyerhofer, and R. Betti, *Rev. Sci. Instrum.* **80**, 043504 (2009).
41. H. Chen *et al.*, *Phys. Rev. Lett.* **114**, 215001 (2015).
42. H. Chen *et al.*, *Phys. Plasmas* **22**, 056705 (2015).
43. H. Chen, D. D. Meyerhofer, S. C. Wilks, R. Cauble, F. Dollar, K. Falk, G. Gregori, A. Hazi, E. I. Moses, C. D. Murphy, J. Myatt, J. Park, J. Seely, R. Shepherd, A. Spitkovsky, C. Stoeckl, C. I. Szabo, R. Tommasini, C. Zwick, and P. Beiersdorfer, *High Energy Density Phys.* **7**, 225 (2011).
44. M. J. MacDonald *et al.*, *J. Appl. Phys.* **120**, 125901 (2016).
45. P. K. Patel *et al.*, *Phys. Rev. Lett.* **91**, 125004 (2003).
46. M.-S. Miao and R. Hoffmann, *Account. Chem. Res.* **47**, 1311 (2014).
47. Y. Ma *et al.*, *Nature* **458**, 182 (2009).
48. E. Gregoryanz *et al.*, *Science* **320**, 1054 (2008).
49. M. Marqués *et al.*, *Phys. Rev. B* **83**, 184106 (2011).
50. J. R. Rygg, J. H. Eggert, A. E. Lazicki, F. Coppari, J. A. Hawreliak, D. G. Hicks, R. F. Smith, C. M. Sorce, T. M. Uphaus, B. Yaakobi, and G. W. Collins, *Rev. Sci. Instrum.* **83**, 113904 (2012).
51. P. M. Celliers, D. K. Bradley, G. W. Collins, D. G. Hicks, T. R. Boehly, and W. J. Armstrong, *Rev. Sci. Instrum.* **75**, 4916 (2004).
52. J. R. Rygg, J. H. Eggert, A. E. Lazicki, F. Coppari, J. A. Hawreliak, D. G. Hicks, R. F. Smith, C. M. Sorce, T. M. Uphaus, B. Yaakobi, and G. W. Collins, *Rev. Sci. Instrum.* **83**, 113904 (2012).
53. G. Gregori *et al.*, *Phys. Plasmas* **11**, 2754 (2004).
54. S. H. Glenzer and R. Redmer, *Rev. Mod. Phys.* **81**, 1625 (2009).
55. Z. Konôpková *et al.*, *Nature* **534**, 99 (2016).
56. K. Ohta *et al.*, *Nature* **534**, 95 (2016).
57. R. F. Smith, S. M. Pollaine, S. J. Moon, K. T. Lorenz, P. M. Celliers, J. H. Eggert, H.-S. Park, and G. W. Collins, *Phys. Plasmas* **14**, 057105 (2007).
58. A. B. Zylstra, J. A. Frenje, P. E. Grabowski, C. K. Li, G. W. Collins, P. Fitzsimmons, S. Glenzer, F. Graziani, S. B. Hansen, S. X. Hu, M. Gatu Johnson, P. Keiter, H. Reynolds, J. R. Rygg, F. H. Séguin, and R. D. Petrasso, *Phys. Rev. Lett.* **114**, 215002 (2015).
59. J. A. Frenje, P. E. Grabowski, C. K. Li, F. H. Séguin, A. B. Zylstra, M. Gatu Johnson, R. D. Petrasso, V. Yu. Glebov, and T. C. Sangster, *Phys. Rev. Lett.* **115**, 205001 (2015).

60. LLE 1999 Annual Report, October 1998–September 1999, p. 222, Laboratory for Laser Energetics, University of Rochester, Rochester, NY, LLE Document No. DOE/SF/19460-332 (January 2000).
61. D. E. Fratanduono, D. H. Munro, P. M. Celliers, and G. W. Collins, *J. Appl. Phys.* **116**, 033517 (2014).
62. D. K. Bradley, S. T. Prisbrey, R. H. Page, D. G. Braun, M. J. Edwards, R. Hibbard, K. A. Moreno, M. P. Mauldin, and A. Nikroo, *Phys. Plasmas* **16**, 042703 (2009).
63. D. K. Bradley, J. H. Eggert, R. F. Smith, S. T. Prisbrey, D. G. Hicks, D. G. Braun, J. Biener, A. V. Hamza, R. E. Rudd, and G. W. Collins, *Phys. Rev. Lett.* **102**, 075503 (2009).
64. S. W. Haan *et al.*, *Phys. Plasmas* **18**, 051001 (2011).
65. L. X. Benedict *et al.*, *Phys. Rev. B* **89**, 224109 (2014).
66. J. K. Crane *et al.*, *J. Phys.: Conf. Ser.* **244**, 032003 (2010).
67. L. Gao, P. M. Nilson, W. Theobald, C. Stoeckl, C. Dorrer, T. C. Sangster, D. D. Meyerhofer, L. Willingale, and K. M. Krushelnick, *Bull. Am. Phys. Soc.* **55**, BAPS.2010.DPP.XO6.1 (2010).
68. J. Peebles, M. S. Wei, A. V. Arefiev, C. McGuffey, R. B. Stephens, W. Theobald, D. Haberberger, L. C. Jarrott, A. Link, H. Chen, H. S. McLean, A. Sorokovikova, S. Krasheninnikov, and F. N. Beg, *New J. Phys.* **19**, 023008 (2017).
69. A. Yogo *et al.*, *Sci. Rep.* **7**, 42451 (2017).
70. H. Chen *et al.*, *Phys. Plasmas*, **24**, 033112 (2017).
71. A. J. Kemp and L. Divol, *Phys. Rev. Lett.* **109**, 195005 (2012).
72. N. Iwata *et al.*, *Phys. Plasma* **24**, 073111 (2017).
73. J. Kim, A. J. Kemp, S. C. Wilks, D. H. Kalantar, S. Kerr, D. Mariscal, F. N. Beg, C. McGuffey, and T. Ma, *Phys. Plasma* **25**, 083109 (2018).
74. G. J. Williams *et al.*, “Relativistic Electron Production Using the NIF-ARC Laser,” to be submitted to *Physical Review Letters*.
75. A. Pukhov, Z. M. Sheng, and J. Meyer-ter-Vehn, *Phys. Plasmas* **6**, 2847 (1999).
76. H. K. Mao *et al.*, *J. Appl. Phys.* **49**, 3276 (1978).
77. A. D. Chijioko, W. J. Nellis, and I. F. Silvera, *J. Appl. Phys.* **98**, 073526 (2005).
78. Y. Wang, R. Ahuja, and B. Johansson, *J. Appl. Phys.* **92**, 6616 (2002).
79. A. Dewaele, P. Loubeyre, and M. Mezouar, *Phys. Rev. B* **70**, 094112 (2004).
80. R. G. Kraus *et al.*, *Phys. Rev. B* **93**, 134105 (2016).
81. C. W. Greeff *et al.*, *J. Phys. Chem. Solids* **67**, 2033 (2006); D. Pile, M. Svandrlík, and F. Parmigiani, *Nat. Photonics* **8**, 82 (2014).
82. R. F. Smith, D. E. Fratanduono, D. G. Braun, T. S. Duffy, J. K. Wicks, P. M. Celliers, S. J. Ali, A. Fernandez-Pañella, R. G. Kraus, D. C. Swift, G. W. Collins, and J. H. Eggert, *Nat. Astron.* **2**, 452 (2018).
83. D. H. Dolan *et al.*, *Nat. Phys.* **3**, 339 (2007).
84. J. S. Oakdale *et al.*, *Adv. Funct. Mater.* **27**, 1702425 (2017).
85. E. Gumbrell *et al.*, *Rev. Sci. Instrum.* **89**, 10G118 (2018).
86. G. E. Kemp *et al.*, *Phys. Plasmas* **23**, 101204 (2016).
87. P. Ramaprabhu *et al.*, *Phys. Fluids* **24**, 074107 (2012).
88. L. Elgin *et al.*, *Bull. Am. Phys. Soc.* **62**, BAPS.2017.DPP.UO8.7 (2017); L. Elgin, presented at the NIF and JLF User Group Meeting 2018, Livermore, CA, 4–7 February 2018; L. Elgin, presented at the OMEGA Laser Facility Users Group 2018 Workshop, Rochester, NY, 25–27 April 2018; L. Elgin, presented at the 9th Fundamental Science with Pulsed Power: Research Opportunities and User Meeting, Albuquerque, NM, 29 July–1 August 2018, Albuquerque, NM.
89. D. H. Munro, *Phys. Rev. A* **38**, 1433 (1988).
90. V. Geppert-Kleinrath *et al.*, *Rev. Sci. Instrum.* **89**, 10I142 (2018).
91. P. L. Volegov *et al.*, *J. Appl. Phys.* **122**, 175901 (2017).
92. K. Molvig *et al.*, *Phys. Rev. Lett.* **116**, 255003 (2016).
93. K. Molvig, M. J. Schmitt, R. Betti, E. M. Campbell, and P. McKenty, *Phys. Plasmas* **25**, 082708 (2018).